Numerical studies of tropical convection

Gerard Kilroy

Munich 2013

Numerical studies of tropical convection

Gerard Kilroy

Dissertation
at the Faculty of Physics
Ludwig–Maximilians–University
Munich

by
Gerard Kilroy
from Mayo, Ireland

Munich, October 2013

Contents

Abstract

Idealized numerical model experiments are presented to investigate the convective generation of vertical vorticity in a tropical depression. The calculations are motivated by observations made during the recent PREDICT field experiment to study tropical cyclogenesis, and by a desire to understand the aggregation of vorticity debris produced by deep convection in models of tropical cyclogenesis to form a monopole vortex.

One aim is to isolate and quantify the effects of low to mid level dry air on convective cells that form within a depression and, in particular, on the generation of vertical vorticity in these cells. Another aim is to isolate the effects of a unidirectional boundary layer wind profile on storm structure, especially on vertical vorticity production and updraught splitting, and the combined effects of horizontal and vertical shear on vertical vorticity production, with and without background rotation. A third aim is to isolate the effects of a vortex boundary-layer wind profile on tropical deep convection, focussing especially on the morphology of vertical vorticity that develops.

The growing convective updraughts, that are initiated by a near surface thermal perturbation, amplify locally the ambient rotation at low levels by more than an order of magnitude and this vorticity persists long after the updraught has decayed, supporting the results of an earlier study. The results of calculations with dry air aloft do not support a common perception that the dry air produces stronger downdraughts.

In calculations where the vertical wind shear changes sign at some level near the top of the boundary layer, as occurs in warm-cored disturbances such as tropical depressions or tropical cyclones, it was found that the tilting of horizontal vorticity by a convective updraught leads not only to dipole patterns of vertical vorticity, but also to a reversal in sign of the updraught rotation with height. This feature is quite unlike the structure in a typical middle-latitude 'supercell' storm. These results provide an essential first step to understanding the interaction between deep convective elements in a tropical depression or tropical cyclone. An increase in the magnitude of boundary-layer shear was found to have the dual effect of weakening the development of the initial thermal, which is detrimental to vertical vorticity production by stretching and tilting, while at the same time increasing the magnitude of horizontal vorticity that can be tilted.

The results provide a basis for appraising a recent conjecture concerning the role of storm splitting in explaining the contraction of the eyewall in tropical cyclones.

In dieser Arbeit wird die konvektive Erzeugung vertikaler Vorticity in einem tropischen Sturm untersucht. Dazu werden idealisierte numerische Modellexperimente durchgeführt.

Zum einen sind die Simulationen durch Beobachtungen motiviert die während der Feldkampagne PREDICT gemacht wurden. Zum anderen dienen sie dem Ziel einen wesentlichen Prozess bei der Entstehung von tropischen Zyklonen in numerischen Modellen zu verstehen. Bei diesem Prozess führt die Verschmelzung von Überresten von Vorticity, welche durch tiefe Konvektion erzeugt wird, zur Bildung eines Wirbels eines Vorzeichens.

Ein wichtiges Teilziel dieser Arbeit besteht darin die Effekte von trockener Luft in tiefen bis mittleren Schichten auf konvektive Zellen die sich innerhalb eines Tiefdruckwirbels formen zu isolieren und zu untersuchen. Im Speziellen wird die Entstehung von vertikaler Vorticity in diesen Zellen untersucht. Desweiteren wird der Einfluss eines unidirektionalen Windprofils in der Grenzschicht auf die Sturmstruktur beleuchtet. Spezieller Fokus liegt dabei auf der Erzeugung vertikaler Vorticity und der Aufteilung von Aufwinden. Außerdem werden die kombinierten Effekte von horizontaler und vertikaler Scherung auf die Erzeugung vertikaler Vorticity beleuchtet. Dabei werden Fälle mit und ohne Hintergrundrotation untersucht. Außerdem werden in dieser Arbeit die Auswirkungen eines wirbelförmigen Windprofils in der Grenzschicht auf tropische tiefe Konvektion untersucht. Dabei liegt der Fokus speziell auf der Morphologie der sich bildenden vertikalen Vorticity.

Die wachsenden konvektiven Zellen verstärken lokal die Rotation der Umgebung in niedriger Höhe um mehr als eine Größenordnung. Dieser Vorticitybeitrag besteht fort lange nachdem der anfängliche Aufwind abgeflaut ist. Diese Ergebnisse untermauern diejenigen früherer Studien.

Die Ergebnisse der Simulationen mit trockenen Luftschichten widersprechen der verbreiteten These, dass trockene Luft stärkere Fallwinde verursacht.

In Störungen mit einem warmen Kern wie zum Beispiel tropischen Stürmen ändert sich das Vorzeichen der vertikalen Scherung im oberen Teil der Grenzschicht. Simulationen mit so einem Windprofil zeigen, dass das Kippen von horizontaler Vorticity durch einen konvektiven Aufwind nicht nur zu Dipolmustern von vertikaler Vorticity führt, sondern auch zu einem Vorzeichenwechsel der Aufwindrotation mit der Höhe. Dies stellt einen Gegensatz zum Wirkprinzip in einem typischen „Superzellen-Sturm" in den mittleren Breiten dar. Die Ergebnisse stellen einen wichtigen ersten Schritt im Verständnis der Interaktion zwischen Zellen tiefer Konvektion in einem tropischen Sturm dar. Eine Zunahme der Scherung in der Grenzschicht wirkt sich zweierlei aus. Zum einen wird die Entwicklung des initialen Aufwinds gehemmt was die Bildung vertikaler Vorticity durch Strecken und Kippen schwächt. Zum anderen wird jedoch gleichzeitig die horizontale Vorticity verstärkt die durch Kippen in vertikale Vorticity umgewandelt werden kann.

Die Ergebnisse dieser Arbeit bieten eine Grundlage um die Rolle der Aufteilung von Stürmen einzuschätzen, welche laut einer kürzlich vorgestellten Hypothese die Kontraktion der Eyewall in tropischen Zyklonen erklärt.

Chapter 1

Introduction

1.1 Overview

Cumulonimbus clouds, commonly known as thunderstorms, are convective clouds that produce rainfall and lightning. These clouds are sometimes hazardous when they form over land, and are associated with large hail, damaging gust fronts, heavy rainfall and even tornadoes. They can cause problems for commercial airplanes as the most intense thunderstorms can have very powerful updraughts, over 20 m s^{-1}. The US National Weather Service defines a severe thunderstorm as having at least one of the following: large hail with a diameter of at least 2.5 cm, storm-force winds of 93 km h^{-1}, and producing one or more tornadoes. This study is concerned with thunderstorms occurring over the ocean, in a tropical environment. In the tropics, cumulonimbus clouds have an essential role in vertically transferring heat and mass into the troposphere, as part of the tropical overturning circulation (Riehl and Markus 1958).

There is mounting evidence that the genesis and intensification of a tropical cyclone[1] is an asymmetric process involving the formation and interaction of rotating convective clouds. Hendricks *et al.* (2004) demonstrate the role that rotating deep convection plays in the formation of tropical cyclones. They defined a two stage process for the formation of a vortex that eventually became Hurricane Diana (1984). The first stage involved a preconditioning of the lower troposphere by the generation of multiple deep rotating clouds, while the second stage involves the merger and axisymmetrization of existing clouds or their rotating remnants. The studies by Hendricks et al. 2004, Montgomery et al. 2006, Nguyen et al. 2008 and Shin and Smith 2008 offer a new paradigm for tropical-cyclone intensification. They indicate that the intensification process is intrinsically three-

---

[1]The current Hurricane Research Division's website (`http://www.aoml.noaa.gov/hrd/tcfaq/A1.html`) uses "tropical cyclone" as the generic term for a non-frontal synoptic-scale low-pressure system over tropical or sub-tropical waters with organized convection (i.e. thunderstorm activity) and a definite cyclonic surface wind circulation." Notably, this definition does not invoke any wind threshold. The same glossary defines a tropical depression as a tropical cyclone with maximum sustained surface winds of less than 17 m s^{-1} (34 kt, 39 mph) and, in the Atlantic and Eastern Pacific Basins, a "tropical storm" as a tropical cyclone with surface winds between 17 m s^{-1} and 33 m s^{-1}.

dimensional and that rotating deep convective clouds, which Hendricks et al. christened "vortical hot towers" (VHTs), are the principle coherent structures in this process.

The role that convective clouds play in contracting the eyewall of a tropical cyclone (and leading to tropical cyclone intensification) is hypothesised in Hogsett and Stewart (2013). As a series of studies (references as above) indicate that thunderstorms play a pivotal role in both tropical cyclogenesis and intensification, it becomes pertinent to clearly understand the dynamics involved in cumulonimbus clouds that develop in environments characteristic of those where tropical cyclogenesis occurs, and in the inner core region of a cyclone once it has formed. One of the major goals of this study is to use a state of the art numerical model to investigate how thunderstorms in a tropical environment are influenced by wind shear (winds that vary in the horizontal and vertical directions). Another major topic is how convective clouds develop in progressively drier environments. In a later chapter the environmental moisture content is reduced in the mid-troposphere over a series of experiments and the ensuing convection is analysed in detail.

Of particular interest is the development of vertical vorticity (local rotation about the vertical axis) within thunderstorms. A number of recent studies have shown that convection growing in environments with some background rotation (whether associated with the Coriolis force or located in the vicinity of a tropical cyclone) have a distinct vortical (rotating) structure. An interesting feature of these rotating clouds is that once the cloud decays, the enhanced rotation can remain for several hours more. New convective clouds can develop in the vicinity and further amplify the already enhanced background rotation. It is vital to understand the dynamics involved in these rotating convective clouds in order to determine how they are involved in tropical cyclogenesis and cyclone intensification.

1.2   Basic concepts

Thunderstorms generally occur in regions where the environment is either conditionally unstable or completely unstable, and where the low-level air is humid. Cumulonimbus clouds are convective clouds which form as warm buoyant air rises. If a parcel of air is warmer than its surroundings then it is positively buoyant, and begins to rise. The warmer the parcel, and therefore the less dense it is when compared to the surrounding environment, the stronger the buoyant force acting on it. The buoyancy force is an upward (or downward) force an air parcel feels due to the difference in density between the air parcel and its surrounding environment.

The buoyancy force is given by

$$B = g\frac{T_{vp} - T_{ve}}{T_{ve}}, \tag{1.1}$$

where g is the acceleration due to gravity, T_{vp} and T_{ve} are the virtual temperatures of the parcel and the environment, respectively. The buoyancy depends, of course, on the reference value chosen for the environment (Smith *et al.* 2005). Another way to quantify

the buoyancy of an air parcel is by using the perturbation density temperature difference (Emanuel 1994), which is a measure of the buoyancy including the effects of water and ice loading. The density temperature difference is given by

$$dT_\rho = T(\frac{1 + \frac{q_v}{\epsilon}}{1 + q_v + q_r + q_i}) - T_{ve}, \tag{1.2}$$

where T is the temperature, q_v is the water vapour mixing ratio, q_r is the rain water mixing ratio, q_i is the ice particle mixing ratio and ϵ is the ratio of the molecular weight of water vapour to dry air and has a value of 0.622.

As an air parcel rises it cools and the water vapour it holds begins to condense into droplets once it reaches its lifting condensation level (LCL). If the parcel has enough buoyancy, and if the atmosphere is suitably unstable, the parcel will rise to its level of free convection (LFC), where it can remain positively buoyant in comparison to the surrounding environment through a significant depth of the troposphere. Typically a rising air parcel has negative buoyancy at the LCL, but it can still be lifted to its LFC by some forced lifting phenomena such as frontal or orographic lifting. Typically, in the tropics over a warm ocean, convection may be initiated by turbulent eddies in the boundary layer. Over night the boundary layer cools radiatively, while the sea surface temperatures remain relatively constant. Turbulent eddies arise and some have more energy than others, and the more energetic ones can penetrate the LFC and develop into convective cells. Once a parcel reaches the LFC, the parcel rises until it reaches a level where it becomes negatively buoyant in comparison to its surroundings, called the level of neutral buoyancy (LNB).

A measure of the maximum energy available to an ascending parcel is given by the Convective Available Potential Energy (CAPE):

$$CAPE = \int_i^{LNB} B\,dz, \tag{1.3}$$

where i is the height level of the initial parcel, LNB is the level of neutral buoyancy and B is the buoyancy of the air parcel. CAPE is a parcel quantity that typically has a strong negative vertical gradient in the lower troposphere. For this reason, the values cited herein are based on an average for air parcels lifted from the surface and at 100 m intervals above the surface to a height of 500 m. Since the calculation of CAPE is a non-linear function of temperature and moisture, this method is preferred to one based on averaged values of temperature and mixing ratio through a surface-based layer of air with some arbitrarily-prescribed depth.

An air parcel needs to reach its LFC before it can harness the CAPE. There is usually some negatively buoyant energy, which is exerted on the parcel, that it must first overcome as it rises to this level. A measure of the energy that will prevent an air parcel from rising is the Convective Inhibition (CIN):

$$CIN = \int_i^{LFC} -B\,dz, \tag{1.4}$$

where i is the height of the initial parcel, which is located somewhere between the surface and the level of free convection, and $-B$ is the negative buoyancy that the parcel has to overcome. Like CAPE, CIN is a quantity that refers also to an air parcel. Rather than computing an average up to 500 m as for CAPE, it seems physically more reasonable to examine the minimum value of CIN up to 500 m.

1.3 Thunderstorm types

Thunderstorms can range from single cells that extend a couple of kilometers in width to convective line systems that span hundreds of kilometers in length. Some thunderstorms can become intense long lasting supercells. A brief description of the different types of thunderstorms is now given.

1.3.1 Ordinary single cell

Ordinary single cells usually occur in environments without, or with very little, vertical wind shear and where the environment contains plenty of low-level moisture. Bryers and Braham (1949) and Browning (1977) describe the "cell" as the fundamental building block of a cumulonimbus cloud. They define the cell as a region of coherent relatively strong updraught which may contain intense precipitation. The life cycle of a cumulonimbus cloud can be described in three stages: the cumulus stage, the mature stage and the dissipating stage.

The cumulus stage begins with some sort of *triggering* event. There are many possible triggers that lead to the initial air parcel warming: some form of unequal surface heating, orographic lifting by terrain, or lifting of air along convergence lines associated by fronts. The cumulus stage, or the growing stage, is characterised by one towering cumulus cloud which has not developed significant rainfall yet. The updraught grows as buoyant air rises and condenses as it reaches its LCL. As the water droplets form, heat is released into the surrounding air by the latent heat of condensation. The air parcel reaches its LFC, either through positive buoyancy or, more likely, some lifting mechanism, where it can then consume CAPE in the environment to grow further. As the updraught reaches the freezing level (the zero degree isotherm, which is at a height of about 5 km in the tropics) some of the water droplets freeze, releasing latent heat of fusion. As the updraught rises the water droplets grow and become heavier, and begin to weigh down the buoyantly rising air. Eventually the weight of the hydrometeors will become so large that the rising air will no longer be able to keep them suspended and a downdraught will form. The appearance of a convective downdraught marks the beginning of the mature stage, which is the most intense stage of the thunderstorm. The downdraught is strengthened by a combination of the weight of the hydrometeors and by cooling as ice particles melt. The downdraught is then strengthened further as rain droplets fall into unsaturated air below cloud base and evaporate, cooling the subsiding air in the process. A spreading gust front occurs as the

downdraught reaches the surface and spreads outwards. The gust front lifts warm moist air into the updraught, prolonging the life of the cell. Once the gust front spreads out too far ahead of the updraught core the energy source of the cell is cut off and the updraught begins to decay. The updraught weakens and subsiding air dominates throughout the cell in the dissipating stage. In a suitably unstable environment the gust front can also produce new convective cells if it lifts enough environmental air to its LFC.

Figure 1.1: A photograph of a field of growing cumuli with single cells developing almost upright in the absence of moderate-strong vertical shear. Photograph taken by Roger. K. Smith.

Houze *et al.* (2009) documented an intense single convective cell, which occurred in the tropical depression that became Hurricane Ophelia (2005), with an updraught that was 10 km wide, 17 km deep and had updraughts of 10-20 m s^{-1} throughout its mid-upper levels. In the tropics convective cells can reach a height of around 15 km during their mature stage, while the cloud top takes on an anvil shape as the updraught reaches a stable layer in the troposphere and spreads outwards. The mature stage can generally last between 15-30 min, while the entire lifetime of the cell takes on the order of one hour. Figure 1.1 shows a photograph of a field of growing cumuli with single cells developing almost upright in the absence of moderate-strong vertical shear.

1.3.2 Multicell

A thunderstorm system that contains more than one ordinary single cell is known as a multicell thunderstorm. Multicell storms usually occur in environments with low-moderate vertical wind shear from the surface to a height of roughly 4 km, and with large values of CAPE (Weisman and Klemp 1982). The vertical wind shear causes the cells to tilt with height and the convective downdraught fall out ahead of the updraught. As the downdraught does not fall into the updraught as in the unsheared case, the life cycle of the sheared cell is prolonged. New cells continuously develop from the converging gust fronts of existing cells.

Figure 1.2 shows a schematic of a multicell system in an unstable environment with weak-moderate vertical shear, where multiple cells are developing at the same time. In the oldest cell (cell 1), only an anvil remains. Moving to the right of the schematic, the larger the number of the cell, the earlier the cell is in its life cycle. The newest cell, Cell 5, is located farthest downshear. This cell evolution pattern is a defining characteristic of organized multicell systems.
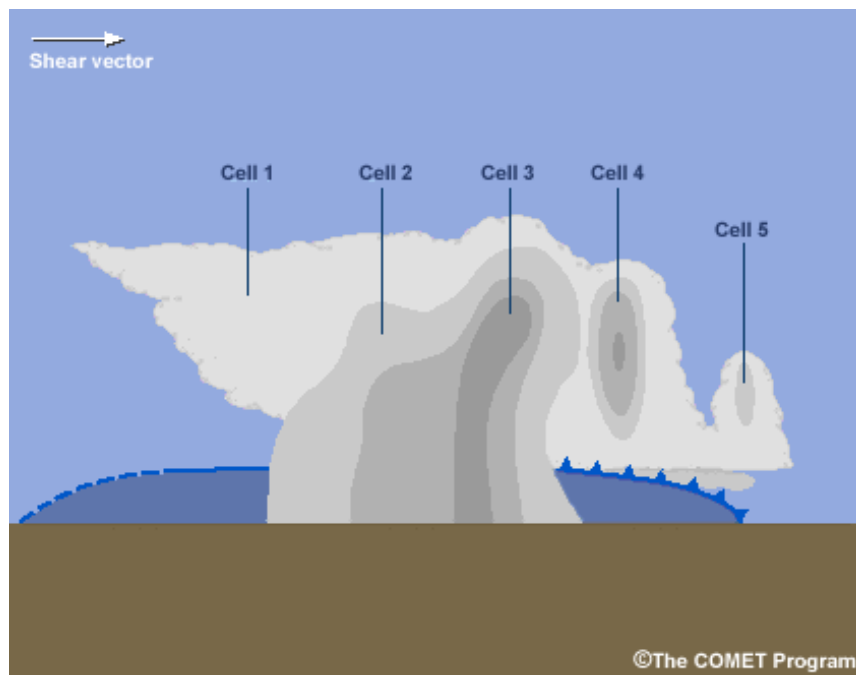

Figure 1.2: A schematic of a mature multiple cell system showing a range of cell growth stages. Figure adapted from the COMET program (www.meted.ucar.edu).

1.3.3 Squall line

Multicell thunderstorms may form in a line or narrow band, known as a squall line. Often squall lines develops along a cold front and can extend for hundreds of kilometers, lasting

several hours. Newton (1950) described the squall line as a system of convective updraughts and downdraughts aligned perpendicular to the vertical shear. The frontal boundary of the squall line lifts environmental air and continuously produces new cells as it propagates onwards. Squall lines often represent the initial phase of a much longer lived mesoscale convective system

1.3.4   Supercell

Supercells are the most intense type of thunderstorms and are associated with severe winds and large hail. They form in environments with large CAPE and with moderate or strong vertical wind shear (Weisman and Klemp 1982), and often spawn tornadoes. Supercells are often the result of storm splitting, where a storm can split into two if the environmental vertical shear is strong enough (Schlesinger 1978). Storm splitting that occurs in an environment with a curved hodograph favours the development of one of the split updraughts more than the other, often leading to the development of a supercell. The supercell consists of a single rotating updraught, and the rotation is primarily cyclonic (anticyclonic) if the wind hodograph veers (backs) with height. After storm splitting and a supercell has developed, the large magnitude of vertical shear causes the updraught to slant and the rain induced downdraught falls out ahead of the updraught. The spreading gust front then lifts warm moist environmental air into the updraught, and the system can self-perpetuate for up to 12 hours.

1.4   Thunderstorm dynamics

In order to analyse the results of the numerical experiments performed herein, some key quantities are studied in detail. Among these quantities are the vertical velocity and vorticity. Vertical wind shear plays an important role in how the thunderstorm develops. The environmental vertical shear is given by

$$\mathbf{S} = \frac{d\mathbf{v}_h}{dz} = \left(\frac{du}{dz}, \frac{dv}{dz} \right) \tag{1.5}$$

where $\mathbf{v}_h(z) = [u(z), v(z)]$, and where (u, v) are the Cartesian velocity components in the (x, y) direction.

The updraught and downdraught strength are quantified by the vertical velocity, w. The vertical acceleration of a particle is given by:

$$\frac{Dw}{Dt} = -\frac{1}{\rho} \frac{dp'}{dz} - B, \tag{1.6}$$

where p' and ρ are the pressure perturbation and density of the particle and B is the

buoyancy force. The material derivative defined as

$$\frac{D}{Dt} = \frac{\partial}{\partial t} + u_j \frac{\partial}{\partial x_j} \tag{1.7}$$

where u_j is the velocity vector, with $j = 1, 2, 3$, pointing in the direction x_j.

The two main forces influencing the acceleration of an air parcel are the vertical pressure gradient force and the buoyancy force.

The vorticity, or a measure of the local rotation, is the curl of the velocity vector $\mathbf{v}$:

$$\omega = (\xi, \eta, \zeta) = \nabla \times \mathbf{v},$$

$$= \left(\frac{\partial w}{\partial y} - \frac{\partial v}{\partial z}\right)\mathbf{i} + \left(\frac{\partial u}{\partial z} - \frac{\partial w}{\partial x}\right)\mathbf{j} + \left(\frac{\partial v}{\partial x} - \frac{\partial u}{\partial y}\right)\mathbf{k} \tag{1.8}$$

where $\mathbf{v}$ is the velocity vector with components (u, v, w), and (ξ, η, ζ) are the vorticity components in the (x, y, z) directions. Of particular interest in this study is the component of vorticity in the vertical direction, ζ. The time evolution of the absolute vertical vorticity is given by:

$$\frac{\partial \zeta_a}{\partial t} = \overbrace{-\mathbf{v}_h \cdot \nabla \zeta_a}^{\text{advective}} - w\frac{\partial \zeta}{\partial z} \overbrace{- \zeta_a\left(\frac{\partial u}{\partial x} + \frac{\partial v}{\partial y}\right)}^{\text{stretching}} + \overbrace{\left(\frac{\partial w}{\partial y}\frac{\partial u}{\partial z} - \frac{\partial w}{\partial x}\frac{\partial v}{\partial z}\right)}^{\text{tilting}}$$
$$+ \underbrace{\frac{1}{\rho^2}\left(\frac{\partial \rho}{\partial x}\frac{\partial p}{\partial y} - \frac{\partial \rho}{\partial y}\frac{\partial p}{\partial x}\right)}_{\text{solenoidal}} \tag{1.9}$$

where the first two terms on the right are the horizontal and vertical advection terms, the third term is the stretching, or divergence term, the fourth term is tilting term and the fifth term is the solenoidal term. ζ_a is the absolute vorticity, which is the sum of the vorticity due to the planetary rotation and the relative vorticity. Figure 1.3 shows a schematic of how vertical vorticity is produced in the atmosphere. In panel (a) there is convergence, or stretching, of existing vertical vorticity. Panel (b) shows how an updraught can tilt background horizontal vorticity into the vertical. This occurs in an environment with vertical shear of the horizontal winds. In panel (b) there is a uni-directional (no winds in the north-south direction) wind shear in which horizontal vorticity exists. The updraught tilts the horizontal vortex tubes into the vertical as the buoyant updraught rises and produces a vertical vorticity dipole. In an environment without background rotation or horizontal wind shear (and thus no contribution from the stretching term), the cyclonic and anticyclonic members of the dipole are identical in magnitude. Once some vertical vorticity is produced by tilting it can be further stretched as described by the stretching term in Equation 1.9. Panel (c) shows how vertical vorticity is produced from baroclinicity,
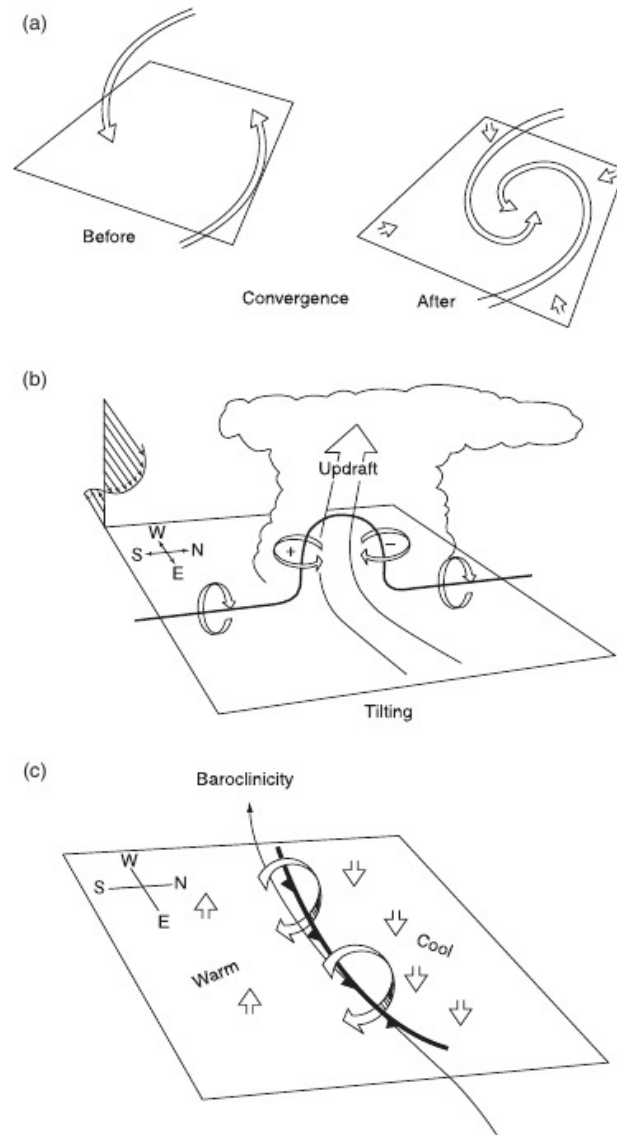
Figure 1.3: A schematic, adapted from Cotton *et al.* (2011), depicting the processes responsible for vertical vorticity generation. Convergence, or stretching, (a) can lead to an amplification of existing vertical vorticity. Tilting (b) of horizontal vorticity by updraughts can produce vertical vorticity. The production of vorticity from baroclinicity (c), where strong horizontal temperature gradients exist.

where a strong temperature gradient exists. Such vorticity is generated as the cool gust front spreads outward in thunderstorms.

Figure 1.4 shows in more detail how vorticity is produced by tilting in a uni-directional vertically sheared environment. Panel (a) is similar to that in Figure 1.3 (b), while panel (b) shows how the convective downdraught can also tilt horizontal vorticity tubes downward. The downdraught then spreads out at the surface to form a spreading gust front. Further
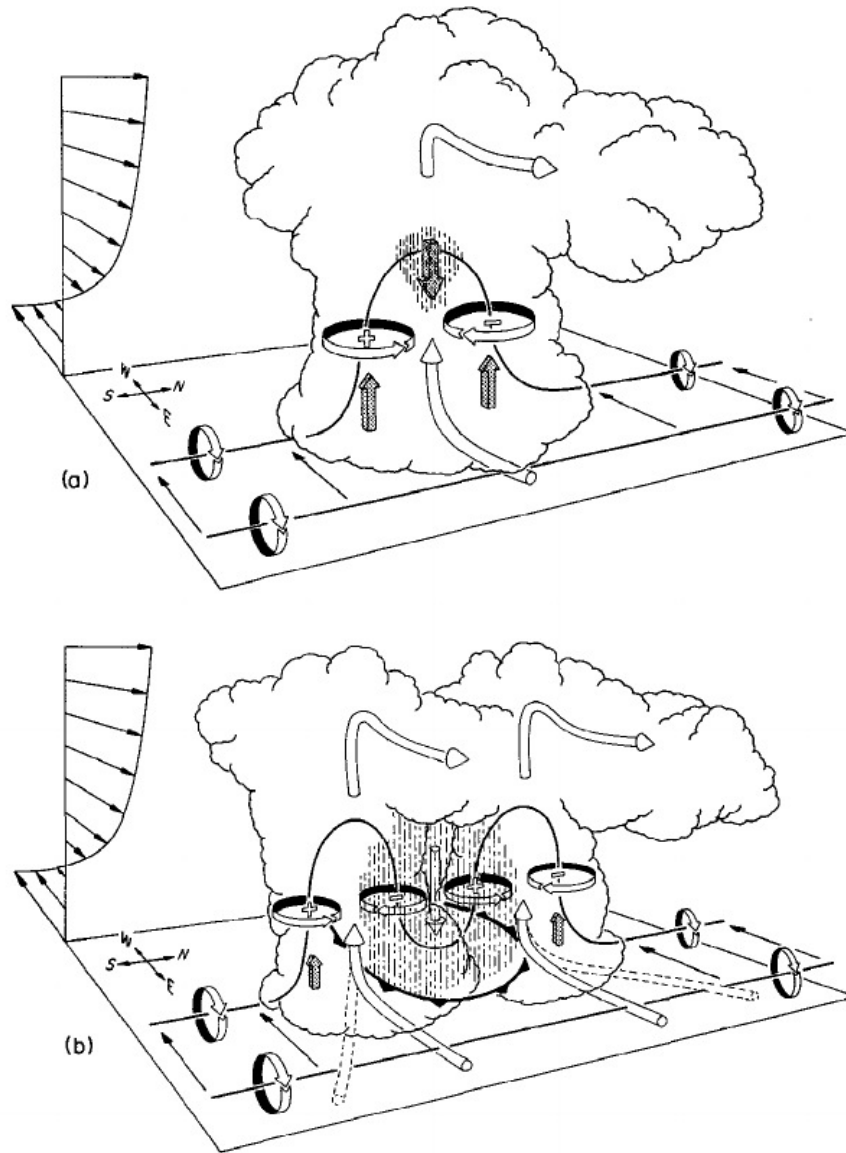
Figure 1.4: A schematic, adapted from Klemp (1987), which illustrates how vortex tubes are tilted in an environment with uni-directional vertical wind shear. The horizontal vorticity tubes (solid black lines) are tilted into the vertical by (a) the growing convective cell to form a vertical vorticity dipole. The rain induced downdraught (b) then tilts the horizontal vorticity downward and aids updraught splitting into two different cells. The white arrows show the direction of the inflow and outflow associated with the cell, while the shaded arrows represent the pressure gradient forces. The dash-dotted lines indicate regions of precipitation. Klemps schematic appears to ignore the effects of vertical shear in *slanting* the cell, which would cause the rain to fall out ahead of the updraught.

vertical vorticity can be produced from baroclinicity here, while lifting of environmental air by the dense cold pool feeds the updraught. If the magnitude of the low-level vertical shear is strong enough the storm may eventually split into two separate updraught cells, which propagate transverse to the shear vector (i.e. to the left and right of the mean flow). These split cells are named left and right-movers and each cell rotates with pure cyclonic or anticyclonic vorticity, depending on the structure of the environmental shear. Split storms can often lead to the development of supercells.

Split storms that develop in an environment of purely uni-directional vertical shear, and no background rotation, produces a mirror-image pair of rotating cells which are equal in strength. The cells are mirror-image because there is no background rotation to be stretched. If some positive background rotation is included, the cyclonic member of the split storm becomes stronger while the anticyclonic member slowly decays, while the opposite happens when background anticyclonic vorticity is included. A clockwise turning hodograph, which is associated with thunderstorm weather patterns in the northern hemisphere, also favours the development of the cyclonic cell, where an anticlockwise turning hodograph favours the anticyclonic cell (Klemp and Wilhelmson 1978).

1.5   PREDICT

The Pre-Depression Investigation of Cloud-systems in the Tropics (PREDICT) experiment was carried out in the period August 15-30 September 2010 to gather data on tropical depressions with the ultimate aim of better understanding the processes that lead to tropical cyclogenesis[2]. A specific aim was to test the so-called "marsupial paradigm" for cyclogenesis proposed in a recent theoretical paper by Dunkerton *et al.* (2009). This paradigm rests on the idea that the synoptic-scale wave in which a large proportion of Atlantic, Caribbean and Eastern Pacific hurricanes form contains a protected region, or pouch, consisting of a closed cyclonic circulation in the low to middle troposphere in a frame of reference moving with the wave. The pouch region has weak deformation and provides a set of closed material contours inside of which air is repeatedly moistened by convection, being protected from the lateral intrusion of dry air and deformation by horizontal or vertical shear.

The experiment was based in St. Croix in the U.S. Virgin Islands and its central facility was the National Center for Atmospheric Research GV research aircraft, a twin-engined jet that has a typical flight duration of 9 hours and can fly at altitudes of up to about 14 km. The aircraft was used to release Global Positioning System (GPS) dropsondes to measure the vertical structure of wind and thermodynamic quantities in tropical disturbances. A total of 26 missions were flown sampling eight tropical disturbances. Further details and some early results of the experiment are presented by Montgomery *et al.* (2012).

The main topic of Chapter 4 was motivated by observations of one particular disturbance that was declared Tropical Storm Gaston on 1 September 2010 by the National Hurricane Center, but which was downgraded on 2 September to a tropical depression after data from the first PREDICT mission into the disturbance became available. The

---

[2]A recent review of tropical cyclogenesis is given by Montgomery and Smith (2011)

disturbance maintained an identity that could be tracked across the Caribbean although the convective activity weakened considerably after 7 September. Five GV flights were made into the disturbance on each day from 2 to 7 September, except on 4 September.

1.6 Vortical convective clouds

Numerical model simulations show that when convection occurs in an environment of non-zero vertical vorticity, updraughts amplify the vorticity by the process of vortex-tube stretching (Hendricks *et al.* 2004, Saunders and Montgomery 2004, Montgomery *et al.* 2006, Nguyen *et al.* 2008, Rozoff 2007, Wissmeier and Smith 2011). Using a cloud model, Wissmeier and Smith (2011) showed that even moderately deep clouds can produce a large amplification (by one to two orders of magnitude) of the vertical component of absolute vorticity on time scales of an hour, and even for a background rotation rate typical of the undisturbed tropical atmosphere. The vorticity so produced has a maximum in the lower troposphere and persists long after the initial updraught has decayed. The authors showed also that the induced tangential wind speeds by a single updraught are typically no more than a few meters per second with a horizontal scale on the order of a kilometer, and would be barely detectable by normal measurement methods in the presence of an ambient wind field. Their results suggest that all tropical convection away from the equator is vortical to some degree and can significantly amplify the vertical vorticity locally. It is not hard to imagine, then, that the stretching of vertical vortex tubes by a developing cumulus cloud is a fundamental process and that it may be an important process in tropical cyclogenesis. In fact, vortical convective clouds have been identified as fundamental building blocks during both the tropical cyclone genesis and intensification process (Hendricks *et al.* 2004, Montgomery *et al.* 2006, Nguyen *et al.* 2008, Braun *et al.* 2010, Fang and Zhang 2010).

The foregoing studies indicate that like-signed vortical remnants generated by convective clouds tend to aggregate in a quasi two-dimensional manner with a corresponding upscale energy cascade and some of these remnants are intensified further by subsequent convective episodes. If the disturbance-scale circulation strengthens, the vorticity remnants tend to become axisymmetrized by the associated angular shear flow. In addition, system-scale inflow forced by the aggregate latent heating from the convective elements leads to an inward advection of convectively-enhanced vorticity. Stokes' theorem applied to a fixed area *surrounding the convection* implies that there will be an accompanying increase in strength of the disturbance-scale circulation on account of the import[3] of ambient absolute vorticity into it. When applied to a fixed area *within the convective region*, the import of convectively-enhanced vorticity into the area will lead also to an increase in the circulation. As the circulation progressively increases in strength, there is some increase in the surface moisture fluxes. This research forms the basis of a unified view of tropical cyclogenesis and intensification (Montgomery and Smith 2011). In this view, the separate

---

[3]The stretching and thereby amplification of ambient (or system-scale) vorticity by convection by itself does not lead to an increase in the circulation around a fixed loop embedded in the flow because stretching leads to a contraction in the areal extent of the amplified vorticity (see Haynes and McIntyre 1987).
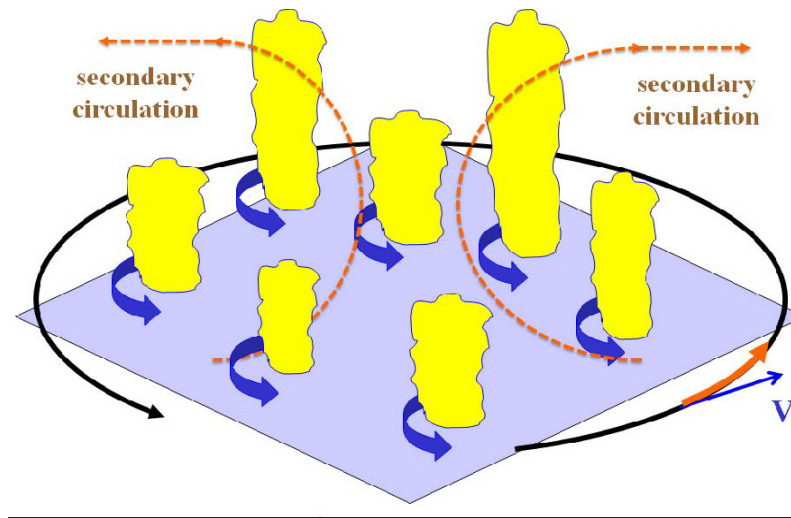
Figure 1.5: Schematic showing the amplification of ambient vertical vorticity by convective cells. If the disturbance-scale circulation strengthens, the vorticity remnants tend to become axisymmetrized by the associated angular shear flow.

stages proposed in previous significant studies and reviews (e.g. Frank, 1987; Emanuel 1989; McBride 1995; Karyampudi and Pierce 2002; Tory and Frank, 2010) are unnecessary. Figure 1.5 shows a schematic of the aforementioned mechanism of vorticity remnant merger. If the disturbance-scale circulation strengthens, the vorticity remnants tend to become axisymmetrized by the associated angular shear flow.

The foregoing discoveries have motivated efforts to document vortical updraughts in observations of tropical cyclones. A summary of these efforts is given by Wissmeier and Smith (2011, see section 1.2). Further, recognition of the possibly important role of cloud rotation on the dynamics of tropical cyclogenesis and tropical cyclone intensification has led to a few studies of the effects of *ambient vertical vorticity* on the dynamics of deep convection in isolation (Rozoff 2007, Wissmeier and Smith 2011).

1.7 The effects of dry air aloft

During the weather briefings for the PREDICT experiment, there was much speculation (Roger Smith, personal communication) that Tropical Storm Gaston failed to redevelop because of its weak pouch that enabled dry air to penetrate its core. The presumption was that the dry air in the lower to middle troposphere would strengthen downdraughts from deep convection and flood the boundary layer with low entropy air from above. However, later analyses of the dropwindsonde data showed that the mission average low-level pseudo-equivalent potential temperature increased during the five days on which the storm was monitored (Smith and Montgomery, 2012). While some of this increase may have been due to the increase in sea surface temperature as the disturbance tracked westwards, there is certainly no evidence of a reduction on a day-to-day time scale that might have thwarted

Gaston's redevelopment. The question then is: are there other aspects of the convection that might be influenced by the presence of dry air that might ultimately be detrimental to cyclogenesis?

Over the years, the common perception that dry air generally enhances the strength of convective downdraughts has been challenged in one way or another by a number of authors (Brown and Zhang 1997, Tompkins 2001, Redelsperger *et al.* 2002, Sobel *et al.* 2004, Kuchera and Parker 2005, Rozoff 2007, Holloway and Neelin 2009, James and Markowski 2009, Minoru and Sugiyama 2010). For example, James and Markowski (2009) performed numerical experiments to determine the effects of dry air aloft on quasi-linear convective systems. Using idealised soundings of differing values of CAPE and moisture content, they found that dry air aloft exerts detrimental effects on overall convective intensity, weakening both updraughts and downdraughts. They found also that in an environment with large CAPE, the influence of dry air is minimised. They attributed the reason for weakened convection to a decline in hydrometeor mixing ratios, as both updraught buoyancy is diluted by dry air entrainment and downdraught strength is weakened by smaller rates of ice melting. However, they did find that for cloud environments with high CAPE, dry air strengthened mesoscale downdraughts in regions of stratiform precipitation. Kuchera and Parker (2005) found also that dry mid-level air is not uniquely associated with strong downdraughts leading to damaging gust fronts.

The above findings motivate the question: if *convective* downdraughts are not strengthened by the presence of dry air, what aspects of the ensuing convection might be detrimental to tropical cyclogenesis? Is it simply the fact that mesoscale downdraughts are strengthened, or is it that by reducing the updraught strength, the dry air reduces the ability of the convection to amplify vorticity? It is the latter question that is a focus of Chapter 4.

This study extends that of Wissmeier and Smith (2011) with a specific aim of quantifying the effects of dry air aloft on deep convection in a tropical depression environment, and, in particular, on the ability of the convection to amplify ambient rotation. It is conceivable that a reduction of the ability of the convection to amplify ambient rotation might have a more detrimental effect on tropical cyclogenesis than the effects of downdraughts by reducing the propensity of deep convective cells to aggregate. As a necessary first step, the focus is on the effects of dry air on a single cloud updraught using thermodynamic soundings based on the data for ex-Gaston. Examined also in Chapter 4 is the dependence of the ensuing convection on the temperature excess of the initial bubble. The experiments performed in Chapter 4 are highly idealized, and ignore several processes that are likely to be important in reality, such as the effects of background wind shear, which is included in the experiments performed in Chapters 5 and 6.

1.8 Storm growth in shear

There have been numerous previous numerical studies of the effects of an ambient *vertical* wind shear on convection, mostly in the context of severe convective storms in the middle latitudes (Schlesinger 1978, Weisman and Klemp 1982, Weisman and Klemp 1984, Rotunno and Klemp 1985, Gilmore *et al.* 2004, see section 8.8.3 of Cotton *et al.* (2011) for a recent review and a more complete list of references). It is pertinent to review briefly the main results of these early studies to provide a context for more recent ones of convection growing in an environment with vertical vorticity associated with horizontal shear, background rotation, or a combination of both.

1.8.1 Storm growth in vertical shear

A considerable focus in studies of severe convective storms has been on the phenomenon of storm splitting. Typically, in the presence of horizontal vorticity associated with vertical shear, the first cell of convection generates a dipole of vertical vorticity within it. As it becomes loaded with water condensate, a downdraught forms and develops into a cold-air outflow. Triggered by lifting at the leading edge of this outflow, subsequent cells of convection form within the positive and negative regions of the vorticity dipole and amplify the vorticity by stretching to form a pair of counter-rotating updraughts (Wilhelmson and Klemp 1978, Wilhelmson and Klemp 1981, Weisman and Klemp 1982, Rotunno and Klemp 1982, 1985). If the broadscale wind veers with height, the cyclonically-rotating cell tends to be stronger than the anticyclonic one, while the anticyclonic cell is favoured when the broadscale wind backs with height (Schlesinger 1978, Rotunno and Klemp 1982). This mechanism has been shown to be important in the generation of so-called "supercell thunderstorms", first described by Browning (1964). The occurrence of storm splitting and supercell storms is favoured by large low-level vertical shear and large instability as characterized by the CAPE (Schlesinger 1978, Wilhelmson and Klemp 1978). Typical values of vertical wind shear in cases where splitting occurs in numerical models is on the order of 10-20 m s^{-1} across the lowest 2-4 km, with typical values of CAPE being on the order of 2000 J kg^{-1} (Wilhelmson and Klemp 1978, Rozoff 2007).

Wilhelmson and Klemp (1978) suggested that low-level shear is more important than upper-level shear to the development of supercell storms, both in numerical models and in reality. Pursuing this suggestion, Weisman and Klemp (1982) investigated a uni-directional wind profile with positive vertical shear from the surface to a height of 4 km. They found that an increase in the magnitude of the shear leads to a decrease in the strength of the updraught and to a decrease in the vertical vorticity produced by stretching, but to an increase in that produced by tilting. They showed also that, in cases of split storms, the vorticity extrema are larger in magnitude after splitting has occurred than in the vortex couplet produced by the initial cell. Up to a point, the magnitude of vorticity increases with increasing shear, but subsequent increases in shear inhibit early storm growth and hence the strength of the vorticity dipole.

1.8.2   Storm growth with ambient vertical vorticity

Rozoff (2007) carried out a series of idealized numerical model simulations on an f-plane to explore the effects of uniform horizontal shear, uniform vertical shear, and a combination of both horizontal and vertical shear, on the evolution of deep convection. He found that storm splitting occurs in all cases (pure vertical shear, pure horizontal shear, or a combination thereof), provided that the shear is sufficiently large. With pure vertical shear, splitting occurs by the classical mechanism described above. With pure horizontal shear, splitting occurs because the initial thermal bubble is progressively elongated by the shear as it rises. Subsequently, a pair of deep convective cells develop near the tips of this elongated thermal. The vorticity enhancement in these cells is due to the stretching of ambient vertical vorticity and therefore both cells have the same sense of rotation. In the case of horizontal and vertical shear, the outcome depends on the relative magnitude of the effects for pure vertical shear and pure horizontal shear. Rozoff showed, *inter alia*, that horizontal shear is generally detrimental to the development of convection and quantified the effect of different amounts of shear on the strength and structure of the convection.

It is shown in Chapter 5 that the mechanism articulated by Rozoff involving pure horizontal shear is dependent on the initial thermal bubble being of sufficient horizontal extent and on the characteristics of the environmental sounding.

Wissmeier and Smith (2011) described also a series of idealized numerical model experiments designed to isolate and quantify the influence of ambient vertical vorticity on the dynamics of deep convection, such as that in a tropical depression. The vertical vorticity was represented either by a uniform *horizontal* shear, a uniform solid-body rotation, or a combination of both. As in the studies discussed above, they found, *inter alia*, that the growing convective cells amplify locally the ambient vorticity at low levels by more than an order of magnitude and that this vorticity, which is produced by the stretching of existing ambient vorticity, persists long after the initial updraught has decayed. They found also that significant amplification of vorticity occurs even for a background rotation rate typical of the undisturbed tropical atmosphere and even for clouds of only moderate vertical extent. The simulations ignored several processes that are likely to be important in reality, such as ambient vertical shear and surface friction, but they represent benchmark calculations for interpreting the additional complexity arising from the inclusion of these effects.

1.8.3   Convective environments in tropical cyclones

In the classical middle-latitude thunderstorm environment, the ambient wind increases in strength with height and the horizontal vorticity has a single sign from the surface upwards. However, in tropical depressions and tropical cyclones, the tangential wind speed decreases with height above a shallow boundary layer so that the sign of the radial vorticity

component changes sign at some low level, typically on the order of 1 km. In contrast, the radial wind component may increase or decrease with height at low levels, depending on the radius (see e.g. Smith and Montgomery 2013). In addition, levels of ambient absolute vertical vorticity may be much larger than in middle-latitude thunderstorm environments. Thus deep convection that develops in tropical cyclones may have a significantly different morphology from that which develops in middle latitudes, a fact that motivates one aspect of the present work. As far as is known, there have been no numerical studies of convection performed with a wind profile as described above.

A key question is how does a boundary layer unidirectional wind structure, where the sign of the horizontal vorticity component changes sign at some low level, affect the generation of vertical vorticity and its vertical structure?

1.8.4 Hodograph turning with height

While there have been several numerical studies of convective cells developing in environments where the wind hodograph turns with height (e.g. Klemp and Wilhelmson 1978, Schlesinger 1978, Weisman and Klemp, 1984), none of these have examined a typical vortex boundary-layer-type wind profile. Klemp and Wilhelmson (1978) showed that if the wind hodograph turns clockwise with height, the right moving storm is favoured, whereas if the wind hodograph turns anticlockwise the development of the left moving cell is preferred. Rotunno (1981) and Rotunno and Klemp (1982) provided an explanation for this behaviour based on linear theory, which predicts that the interaction of the mean shear with the updraught produces favourable vertical pressure gradients along its right flank. Their analyses suggest that although nonlinear effects strongly promote splitting of the updraught, the linear forcing remains the dominant factor in preferentially enhancing updraught growth on the right flank.

Another key question is how does a typical vortex boundary-layer-type wind profile structure affect the generation of vertical vorticity and its vertical structure?

1.9 The Hogsett and Stewart conjecture

In a recent paper, Hogsett and Stewart (2013) proposed an interesting conceptual model involving storm splitting to explain the inward contraction of eyewall convection in tropical cyclones. The model is based on the idea that deep convection growing in the rapidly-rotating environment of a tropical cyclone might have a character similar to "supercell convection", which, in the middle latitudes is a by-product of storm splitting. Exploiting the analogy with splitting storms in the middle latitudes, they likened the radially-inward movement of the cyclonic cell of a split pair to the cyclonic "right-mover" of a split pair in the middle latitudes. They noted that, because the vertical shear is negative in the tropical

cyclone, the cyclonic cell of a pair occurs to the left of the azimuthal mean (tangential) wind (i.e. radially inwards) and referred to this cell as a "left mover". They argued that the anticyclonic cell to the right of the mean tangential wind would be weakened by the production of cyclonic vertical vorticity by stretching in the updraught of this cell.

The conceptual model involving storm splitting to explain the inward contraction of eyewall convection in tropical cyclones is worthy of further investigation, especially in view of the possible modifying role of ambient horizontal vorticity associated with the positive vertical shear in the boundary layer.

1.10 Motivation

A series of studies published in the past ten years have identified vortical convective clouds as fundamental building blocks in the genesis and intensification of tropical cyclones (Hendricks *et al.* 2004, Montgomery *et al.* 2006, Nguyen *et al.* 2008, Braun *et al.* 2010, Fang and Zhang 2010). While Wissmeier and Smith (2011) isolated the processes leading to the generation of vertical vorticity in a very simple configuration, the question remains as to how vertical vorticity develops in more complex tropical depression environments. The present study is motivated by the desire to understand the merger of convectively-induced vorticity anomalies during vortex evolution, a topic that is currently not well understood (Nguyen *et al.* 2008, Deng *et al.* 2012). In fact, the relevance on the importance of vortical deep convection in cyclogenesis was first pointed out in a case study by Hendricks *et al.* (2004), and then in a numerical model study by Montgomery *et al.* (2006). During genesis the vertical vorticity generated by the convection progressively merged to form a vortiticy monopole over the evolution of the vortex, although the processes involved in the merger are not yet well understood. In the presence of vertical shear there are vertical vorticity dipoles, whereas in Nguyen *et al.* (2008) it was suggested that the merger was a barotropic process.

The need is to better understand the merger process, and to do that it seems sensible to begin with understanding how rotation develops in individual clouds. This thesis is set up as to carry out a series of simple thought experiments based on a hierarchy of calculations with increasing complexity. The aim is to isolate the basic processes of vorticity generation in deep convective clouds in an increasingly complex environment. Avoiding complexity is desired, at least initially, when trying to fully understand the dynamics of atmospheric phenomena. A quote from Ian James summarises this argument. "This is not to say that using such [simple] models is folly. Indeed the aim of any scientific modelling is to separate crucial from incidental mechanisms. Comprehensive complexity is no virtue in modelling, but an admission of failure" (James, 1994).

1.11   Thesis structure

Chapter 2 briefly describes the numerical model and the typical experimental setup used in this study. The method used to initiate convection is described also.

The typical evolution of a convective cell in a quiescent environment is examined in detail in Chapter 3. The experiment in this chapter is used as a control to compare to two other experiments with soundings that become progressively drier at mid-levels.

The findings that dry air aloft does not increase the strength of the convective downdraught motivate the question: if *convective* downdraughts are not strengthened by the presence of dry air, what aspects of the ensuing convection might be detrimental to tropical cyclogenesis? Is it that by reducing the updraught strength, the dry air reduces the ability of the convection to amplify vorticity? It is this question that is a focus of Chapter 4.

One aim of Chapter 5 is to extend that of Wissmeier and Smith (2011) by investigating and quantifying the combined effects of both horizontal and vertical wind shear on deep convection that develops in a thermodynamic environment typical of a tropical depression. Particular attention is focussed on the generation of vertical vorticity by convection and the role of boundary layer shear. A second aim is to examine the role of a deep layer of negative vertical shear overlying a shallow layer of positive vertical shear on storm morphology. This pattern of shear arises in the tangential wind direction in tropical cyclones, although the complete boundary-layer flow in a tropical cyclone is not unidirectional. A third aim of this chapter is to re-examine the mechanisms involved in storm splitting discussed by Rozoff (2007), again giving particular attention to vertical vorticity generation. Since there is observational evidence for the existence of supercell convection in tropical storms, it may be presumed that storm splitting is a relevant process in these systems also.

An additional complication in the context of tropical cyclones is that there is a significant radial wind component in the boundary layer and this component may increase or decrease with height at low levels, depending on the radius (see e.g. Smith and Montgomery 2013). Thus, experiments with unidirectional vertical wind profiles examined may be over-simplistic in application to such vortices. For this reason, a further series of numerical experiments are carried out in Chapter 6 to examine the additional effects of a typical radial wind profile in a tropical-cyclone on the evolution of deep convection, focussing on vertical vorticity production. In Chapter 6 the conceptual model of Hogsett and Stewart is also investigated.

A summary and discussion of the results and the conclusions, along with a discussion of future work, are given in Chapter 7.

Chapter 2

The numerical model

2.1 Bryan Cloud Model (CM1)

The numerical model used for this study is the state-of-the-art three-dimensional cloud model of Bryan and Fritsch (2002) and Bryan (2002). CM1 is a three-dimensional, non-hydrostatic, non-linear, time-dependent numerical model designed for idealized studies of atmospheric phenomena. CM1 is designed primarily for idealized research, particularly for deep precipitating convection (i.e., thunderstorms). The model retains several terms in the governing thermodynamic and pressure equations that are often neglected in atmospheric models. CM1 does not precisely conserve total energy or mass to machine accuracy because of technical numerical reasons. However, it retains several terms in the internal energy equation that many other numerical models neglect, such as terms associated with the heat content of hydrometeors, and dissipative heating. Because the pressure equation in CM1 retains all terms, its mass errors are several orders of magnitude smaller than those from other cloud models that integrate pressure equations (e.g., Pennsylvania State University/National Center for Atmospheric Research mesoscale model (MM5), Advanced Regional Prediction System (ARPS), Regional Atmospheric Modeling System (RAMS)). See Bryan and Fritsch (2002, MWR, pg 2917) and Bryan and Rotunno (2009, MWR, pg 1770) for more information.

CM1 was designed specifically to do very-large domain simulations using high resolution; specifically, it has comparatively little memory overhead, which allows the code to be applied to very large problems (i.e., domains of order 10^9 grid points). Also, CM1 is rare (if not unique) in its ability to use different equation sets, for different applications; for example, the model can be run using the compressible equations (with three different solvers, depending on application and desired accuracy), but it can be used also with the anelastic equations, and even the incompressible equations. This capability allows CM1 to be used very efficiently for a broad range of problems that span many scales (see CM1 website for more information [1]).

The model incorporates a parametrisation scheme for warm rain processes as well as

---

[1]http://www.mmm.ucar.edu/people/bryan/cm1

one for processes involving ice microphysics. The latter is Gilmore's Li-scheme, in which cloud water, rain water, cloud ice, snow and hail/graupel are predicted (Gilmore *et al.* 2004). The model has no parametrisation of the planetary boundary layer. For simplicity, radiation effects are neglected and there are no surface fluxes of momentum, heat, and moisture. A 6th order horizontal advection scheme, which is not diffusive, is chosen. An additional artificial filter is applied to all variables to ensure stability using a coefficient suggested by Bryan (personal correspondence).

In this study CM1 version 1.15 is used.

2.1.1 The governing equations

The equations for the model were derived from a set of equations that govern the conservation of mass, total energy, and total momentum.

Thermodynamic equation

The dry air potential temperature is given by:

$$\theta \equiv \frac{T}{\pi} \tag{2.1}$$

where θ is the potential temperature, T is the temperature and π is the non-dimensional pressure, which is defined below.

The prognostic equation is:

$$\frac{D \ln \theta}{Dt} = -\left(\frac{R_m}{c_{vml}} - \frac{R_d c_{pml}}{c_p c_{vml}} \right) \frac{\partial u_j}{\partial x_j}$$
$$+ \frac{c_v}{c_p c_{vml} T} \left(L_v \dot{q}_{cond} + L_s \dot{q}_{dep} + L_f \dot{q}_{frz} \right) - \frac{R_v}{c_{vml}} \left(1 - \frac{R_d c_{pml}}{c_p R_m} \right) \left(\dot{q}_{cond} + \dot{q}_{dep} \right), \tag{2.2}$$

where c_p and c_v are the specific heat of dry air at constant pressure and volume, respectively. Then c_{pml} and c_{vml} account for the specific heat of moist air and liquid water at constant pressure and volume, respectively. R_d, R_m and R_v are the gas constants of dry air, moist air and water vapour, respectively. L_f, L_s and L_v are the latent heat coefficients for freezing, sublimation and vaporisation, respectively. The rates of change of the mixing ratio with time for condensation, deposition and freezing are given by $\dot{q}_{cond}$, $\dot{q}_{dep}$ and $\dot{q}_{frz}$, respectively.

Pressure Equation

A prognostic equation for the Exner Function (or the non-dimensional pressure) is derived also. The Exner function is given by:

$$\pi \equiv \left(\frac{p}{p_0} \right)^{\frac{R_d}{c_p}} \tag{2.3}$$

where $p_0 = 1000$ hPa is the reference pressure.

The prognostic equation is:

$$\frac{D \ln \pi}{Dt} = -\frac{R_d}{c_p} \frac{c_{pml}}{c_{vml}} \frac{\partial u_j}{\partial x_j}$$

$$+\frac{R_d}{c_p} \left[\left(\frac{L_v}{c_{vml}T} - \frac{R_v c_{pml}}{R_m c_{vml}} \right) \dot{q}_{cond} + \left(\frac{L_s}{c_{vml}T} - \frac{R_v c_{pml}}{R_m c_{vml}} \right) \dot{q}_{dep} + \frac{L_f}{c_{vml}T} \dot{q}_{frz} \right], \quad (2.4)$$

Momentum Equation

The momentum equation is expressed as

$$\frac{Du_i}{Dt} = -\frac{1}{\rho_a (1 + q_t)} \frac{\partial p}{\partial x_i} - \delta_{i3} g, \quad (2.5)$$

where ρ_a is the dry air density, q_t is the sum of all the mixing ratios, and δ_{i3} is the Kronecker delta function. The momentum equation is then rewritten in terms of π using Equation 2.3. First the natural logarithm and derivative of Equation 2.3 are used to obtain the derivative of p with respect to x_i:

$$\frac{\partial p}{\partial x_i} = \frac{p c_p}{R_d \pi} \frac{\partial \pi}{\partial x_i} \quad (2.6)$$

Then, by using the equation of state,

$$p = \rho_a R_d T_v = \rho_a R_d T \left(1 + \frac{q_v}{\epsilon} \right), \quad (2.7)$$

and Equation 2.1, Equation 2.6 becomes

$$\frac{\partial p}{\partial x_i} = \rho_a c_p \theta \left(1 + \frac{q_v}{\epsilon} \right) \frac{\partial \pi}{\partial x_i}, \quad (2.8)$$

which is substituted into Equation 2.5, giving

$$\frac{Du_i}{Dt} = -c_p \theta_\rho \frac{\partial p}{\partial x_i} - \delta_{i3} g, \quad (2.9)$$

where θ_ρ is the density potential temperature given by

$$\theta_\rho = \theta \left(\frac{1 + \frac{q_v}{\epsilon}}{1 + q_t} \right). \quad (2.10)$$

Then the variables p, π, θ, and q_v are expressed as the sum of a mean and perturbation component, while the base state is assumed to be in hydrostatic balance

$$\frac{\partial p_0}{\partial z} = -\rho_0 g \left(1 + q_{v0}\right) \tag{2.11}$$

where the subscript 0 refers to the base state of the variable. The hydrostatic equation can be written in terms of the non-dimensional pressure, yielding

$$\frac{\partial \pi_0}{\partial z} = \frac{-g}{c_p \theta_{\rho 0}} \tag{2.12}$$

and assuming that the base state momentum, and that the liquid water and ice mixing ratios are zero, the momentum equation is given by

$$\frac{D u_i}{D t} = -c_p \theta_\rho \frac{\partial \pi^{'}}{\partial x_i} - \delta_{i3} g \left(\frac{\theta_\rho}{\theta_{\rho 0}} - 1\right). \tag{2.13}$$

The buoyancy term (term on the right of Equation 2.13) is different from that used in most other models in that it is exact, whereas other models derive this by invoking Taylor series approximations.

In summary, the main advantages of these equations over those used in different models are (1) the inclusion of specific heats of liquid and frozen water particles; (2) the inclusion of diabatic terms in the pressure equation; and (3) an unapproximated buoyancy term in the momentum equation.

2.1.2   Numerics

CM1 is written in the framework of the *Arakawa C* grid (Arakawa and Lamb 1977) so that the momentum points are staggered one-half a grid spacing from the locations of the scalars (e.g., θ, π and mixing ratios). In this study the grid spacing in the horizontal directions is constant, while a stretched grid is used in the vertical to give higher resolution at low-levels.

To maintain mass conservation there is no flow through the upper and lower boundaries (i.e., w is set to zero at these surfaces). As the upper boundary is a rigid lid, the location of the boundary is placed far into the stratosphere to minimize the effects of gravity waves. There is also a sponge-layer implemented at upper levels to inhibit the reflection of any waves from the top. At lateral boundaries, an open radiative boundary condition is applied in this study.

2.1.3   Microphysics

There is the option to use several different microphysics schemes in CM1: The warm-rain only Kessler scheme, the NASA-Goddard version of the Lin/Farley/Orwell (LFO) scheme, the Thompson scheme, the Gilmore/Straka/Rasmussen version of the LFO scheme, the Morrison double-moment scheme and the warm-rain only Rotunno-Emanuel (1987) simple water-only scheme. In this study two separate schemes are used: the warm-rain Kessler scheme and the warm-rain and ice Gilmore/Straka/Rasmussen scheme. The Kessler scheme is based on equations presented in Klemp and Wilhelmson (1978) while the Gilmore/Straka/Rasmussen scheme is based on a version of the LFO scheme (Lin *et al.* 1983, Gilmore *et al.* 2004). The ice scheme contains mixing ratios of cloud ice, snow and hail/graupel in addition the warm rain mixing ratios of water vapour, cloud condensate and rain water.

2.1.4   Initial thermal perturbation

Convection is initiated by a symmetric thermal perturbation with a horizontal radius of 5 km and a vertical extent of 1 km. The temperature excess has a maximum at the surface at the centre of the perturbation and decreases monotonically to zero at the perturbation's edge. The perturbation centre coincides with the centre of the domain. While this method for the initiation of convection is necessarily artificial, it is unclear how to significantly improve upon it and for this reason it has been widely used in numerical studies of deep convection (see e.g. Weisman and Klemp 1982, Gilmore *et al.* 2004, Rozoff 2007, Wissmeier 2009[2] and Wissmeier and Smith 2011).

The thermal perturbation is given by

$$\theta' = b \cos\left(\frac{1}{2}\pi\beta\right)^2, \tag{2.14}$$

where

$$\beta = \sqrt{\left(\frac{x - x_c}{r_h}\right)^2 + \left(\frac{y - y_c}{r_h}\right)^2 + \left(\frac{z - z_c}{r_v}\right)^2}, \tag{2.15}$$

and where b is the maximum temperature perturbation; x_c, y_c and z_c represent the location of the centre of the maximum temperature perturbation; and r_h and r_v are the horizontal and vertical radius of the bubble.

The initial thermal perturbation does not include a moisture perturbation, so that the relative humidity does not initially increase within the bubble.

---

[2]Section 3.4.2 therein examines the sensitivity of the storm's initial updraught strength on the warm bubble parameters (width, depth, temperature excess).

In reality, thermal perturbations over the ocean will be linked to surface heat fluxes, but there are other ways in which convection may be triggered such as lifting at gust front boundaries generated by prior convection. For this reason, other methods for storm initiation have been used. One method is to begin with a low-level cold pool that induces sufficient lifting at its boundary to bring environmental air to its LFC (e.g. Trier *et al.* 1996; Wissmeier *et al.* 2010; Fierro *et al.* 2012). Another method is simply to impose a vertical velocity at low levels to achieve the same result (e.g. Ferrier and Houze 1989).

Chapter 3

Evolution of control experiment

A control experiment is carried out in a quiescent environment with a symmetric thermal perturbation on an f-plane with the Coriolis parameter $f = \zeta_o$, where $\zeta_o = 1.5 \times 10^{-4}$ s^{-1}. The results of this experiment are compared to the results of other experiments presented in Chapter 4, which aim to isolate and quantify the effects of low to mid level dry air on convective cells that form within a depression environment.

3.1 Model configuration

The experiment uses the same model configurations as that of Experiment 9 from Wissmeier and Smith (2011), except the horizontal domain size and grid spacing are halved to give improved horizontal resolution of the cloud updraughts. The horizontal domain size is 25 km × 25 km with a uniform horizontal grid spacing of 250 m. The vertical domain extends to a height of 25 km with the vertical grid interval stretching smoothly from 120 m at the surface to 1000 m at the top. There are 47 grid levels in the vertical, 8 of which are below 850 mb. The large time step is 3.7 seconds and the integration time is 2 h. There are 8 small time steps per large time step to resolve fast-moving sound waves. The default "open" boundary conditions are used at the lateral boundaries. A sponge-layer is implemented in the uppermost 2 km to inhibit the reflection of gravity waves from the upper boundary. The experiment includes both warm rain processes and an ice microphysics scheme.

3.1.1 Initiation of convection

Convection is initiated in a quiescent environment by a symmetric thermal perturbation with a horizontal radius of 5 km and a vertical extent of 1 km. The temperature excess has a maximum at the surface at the centre of the perturbation and decreases monotonically to zero at the perturbation's edge. The perturbation centre coincides with the centre of the domain. In general, the details of the ensuing convection such as the maximum updraught strength and the updraught depth will depend on the spatial structure and amplitude of

the thermal perturbation. While this method for the initiation of convection is necessarily artificial, it is unclear how to significantly improve upon it and for this reason it has been widely used in numerical studies of deep convection (see e.g. Weisman and Klemp 1982, Gilmore *et al.* 2004, Rozoff 2007, Wissmeier 2009[1]) and Wissmeier and Smith 2011.

In reality, thermal perturbations over the ocean will be linked to surface heat fluxes, but there are other ways in which convection may be triggered such as lifting at gust front boundaries generated by prior convection. For this reason, other methods for storm initiation have been used. One method is to begin with a low-level cold pool that induces sufficient lifting at its boundary to bring environmental air to its LFC (e.g. Trier *et al.* 1996; Wissmeier *et al.* 2010; Fierro *et al.* 2012). Another method is simply to impose a vertical velocity at low levels to achieve the same result (e.g. Ferrier and Houze 1989). **Both methods are unsuitable for implementation in the simple thought experiments formulated here, where the desire is to initiate an updraught that is axisymmetric.**

3.1.2   Representation of vertical vorticity

The choice of Coriolis parameter $f = \zeta_o = 1.5 \times 10^{-4}$ s^{-1} is typical of the vertical vorticity at low levels in Ex-Tropical Storm Gaston (Mark Boothe, personal communication). The use of an f-plane with an enhanced value of f beyond a typical tropical value is a simple expedient to model the background rotation of the vortex in the present problem. For further simplicity, both horizontal and vertical wind shear have been omitted in representing the pouch environment (recall Section 1.5). One of the main goals of this study is to examine and quantify the amplification of the background rotation by deep convection in such an environment, starting with an initial uniform background rotation and an environmental sounding.

3.2   Thermodynamic sounding

The control experiment uses an idealised sounding with piecewise-linear profiles of virtual potential temperature, θ_v, and mixing ratio, r. The sounding approximates that obtained from the dropsonde launched at 18:20 UTC on 5 September into ex-Tropical Storm Gaston, but has somewhat lower CAPE (2770 J kg^{-1} compared with 3500 J kg^{-1}). The dropsonde was launched near the centre of the low-level circulation in a region of high total precipitable

---

[1]Section 3.4.2 therein examines the sensitivity of the storm's initial updraught strength on the warm bubble parameters (width, depth, temperature excess).

water (TPW), high CAPE[2] and zero CIN[3]. In fact, the 18:20 UTC sounding had the largest TPW, 65.2 kg m^{-2}, on that day.

(a)

(b)
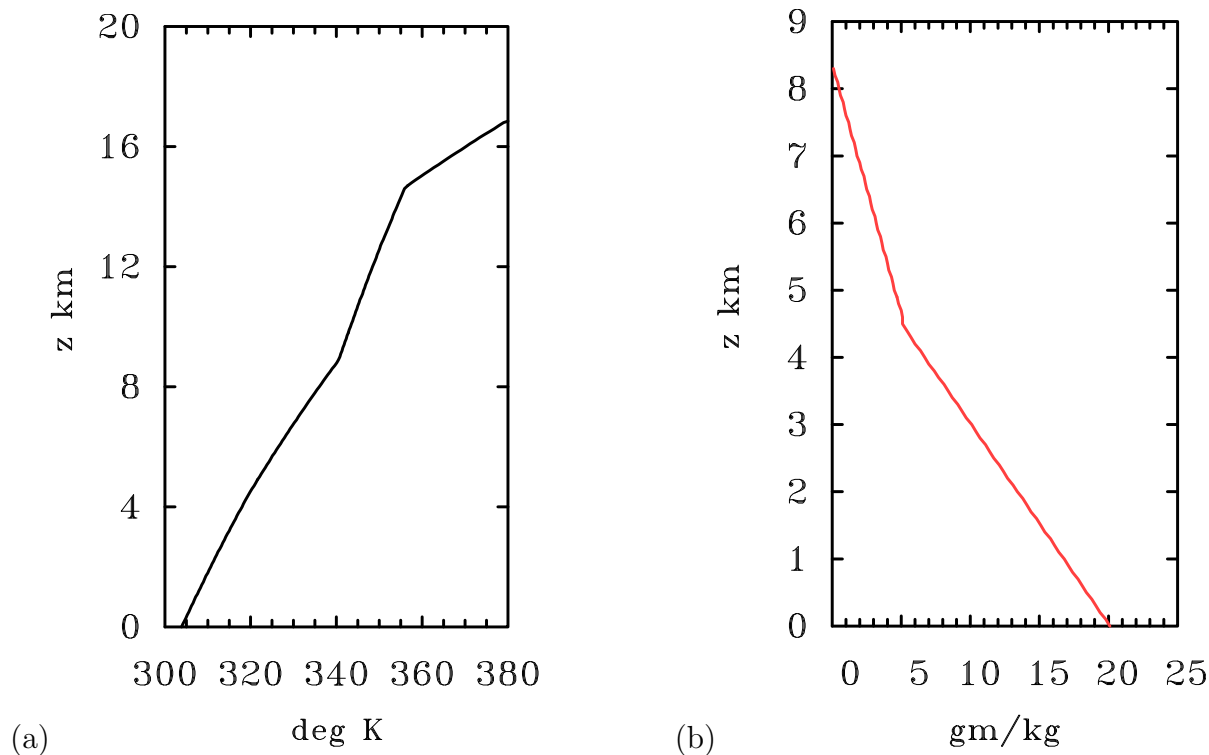
Figure 3.1: The idealised sounding used for the control experiment. Shown is the virtual potential temperature on the left and mixing ratio on the right.

Figure 3.1 shows the vertical profile of virtual potential temperature and mixing ratio. To summarise the control sounding, the CAPE is 2770 J kg^{-1}, the CIN is 40 J kg^{-1} and the TPW is 62.3 kg m^{-2}.

---

[2]The reader is reminded that CAPE is a parcel quantity that typically has a strong negative vertical gradient in the lower troposphere. For this reason, the values cited herein are based on an average for air parcels lifted from the surface and at 100 m intervals above the surface to a height of 500 m. Since the calculation of CAPE is a nonlinear function of temperature and moisture, this method is preferred to one based on averaged values of temperature and mixing ratio through a surface-based layer of air with some arbitrarily-prescribed depth.

[3]Like CAPE, CIN is a quantity that refers also to an air parcel. Rather than computing an average up to 500 m as for CAPE, it seems physically more reasonable to examine the minimum value of of CIN up to this level.

3.3   Control experiment evolution

The evolution of the convective cell in the control experiment is described here in three separate phases: the early phase in which the cloud develops from the initial thermal perturbation, the mature phase where the cloud experiences the strongest vertical motion, and the decay phase where the updraught has ended and only broadscale subsiding vertical motion remains. All three phases are complete within 60 minutes in this case. An analysis of some maximum and minimum values for the life time of the cloud is carried out.

3.3.1   Early development

The updraught that forms the first convective cell is initiated by the buoyancy of the initial thermal bubble. The updraught develops slowly at first, but increases rapidly in vertical extent and strength as additional buoyancy is generated by the latent heat release of condensation. Figure 3.2 shows vertical cross sections of selected fields through the domain centre in the control experiment at 10 min, when the initial thermal is beginning to rise and form an updraught, and at 20 minutes when the updraught is already rapidly growing. Panels (a) and (e) show isopleths of the vertical mass flux $M = \rho_o(x,z)w(x,z)$ with the 0.2 g kg^{-1} contour of cloud water plus ice superimposed at 10 and 20 min, respectively. At this early stage, the mass flux is positive as the cloud begins to form, but there is a narrow region of subsidence on the flanks of the cloud at 20 min associated with the downward branch of the overturning circulation associated with the rising thermal. At 20 min a cloud has formed as the rising air reaches its LCL and the water vapor in the rising air begins to condense. As water droplets form in the rising air the updraught is strengthened by the latent heat of condensation.

Figures 3.2b and f show the corresponding cross section of density temperature difference, dT_ρ, between the cloud and its environment. The quantity dT_ρ is a measure of the buoyancy including the effects of water loading (Emanuel 1994, Chapter 2). The positive values of dT_ρ at 10 min represent the initial thermal, which has a maximum located at the surface. At this time a small strip of negative buoyancy has developed above the rising thermal due to the lifting of environmental air above the thermal as it rises. This lifted environmental air is cooler than its surroundings and experiences a negative buoyancy force acting on it. By 20 min additional positive buoyancy, which is located between heights of 1 and 3 km, is generated by the latent heat release of condensation as the cloud forms.

Figures 3.2c and g show cross sections of pseudo-equivalent potential temperature, θ_e, at 10 and 20 min. These plots illustrate how the cloud is effectively a plume of relatively high near-surface values of θ_e that mixes with lower values of θ_e from low and middle tropospheric levels as it ascends. The isotherms bend upwards as the updraught forms and near surface values of θ_e are transported vertically to higher levels.

The cross sections of the vertical component of relative vorticity, ζ, at 10 and 20 min indicate that, even as early as 20 min, there is a significant amplification of the ambient vorticity, and the vorticity generated is a maximum at the surface (Figure 3.2h). This amplification of vorticity is a result of the stretching of ambient absolute vorticity by the
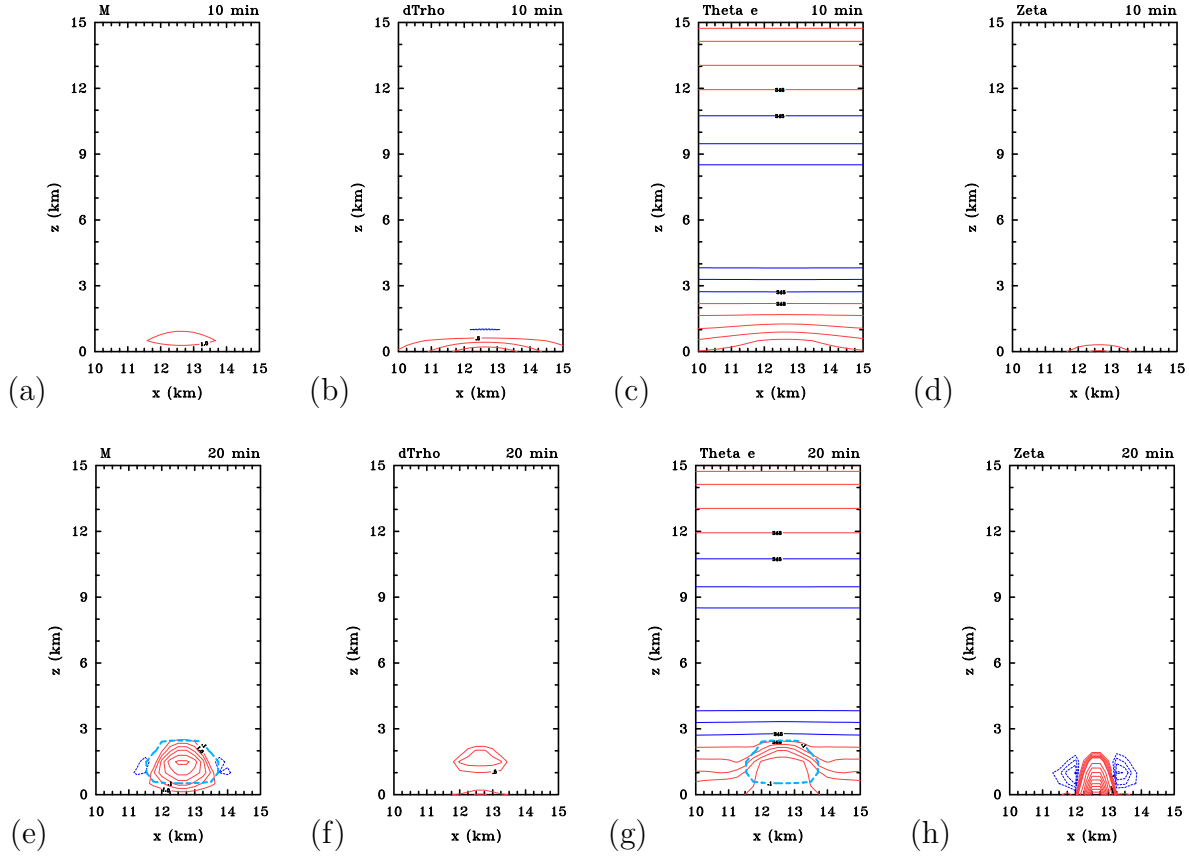
Figure 3.2: Vertical cross sections through the domain centre of (a,e) vertical mass flux, M, (b,f) density temperature difference, dT_ρ, between the cloud and its environment, and (c,g) pseudo-equivalent potential temperature, θ_e, and (d,h) the vertical component of relative vorticity ζ in Experiment 1 at 10 min (upper row) and 20 min (lower row). Shown also are the cloud boundaries, characterized by the 0.1 g kg^{-1} contour of cloud water + ice (thick dashed light blue curve), and the rain shaft, characterized by the 0.5 g kg^{-1} contour of rain water (thick black curve). In panels (d) and (e), the region of ice is delineated by the 0.1 g kg^{-1} contour of ice (thick dashed green curve). The calculations using a square horizontal grid lead to a weak azimuthal wavenumber-4 asymmetry that is most prominent in the vorticity field. This asymmetry accounts for the departures from axisymmetric features in panels (d) and (h). Contour interval: for M 1 kg s^{-1} m^{-2}; for dt_ρ 0.5 K; for θ_e 3 K; for ζ, thin contours 5×10^{-4} s^{-1}. Contours of θ_e change colour from blue at 345 K to red at and above 348 K.

vertical gradient of the mass flux, which is positive at this time up to a height of almost 2 km (Figure 3.2(e)).

3.3.2 Mature phase

While the assumption of an axisymmetric thermal rising in an environment without vertical shear is certainly an idealization, it is not totally unrealistic as suggested by the cloud shown in the photograph of a moderately deep, precipitating cumulus congestus cloud shown in Figure 3.3.

Figure 3.3: Photograph of a precipitating cumulus congestus cloud with little or no vertical shear in the lower and middle troposphere taken from the Pacific Island of Guam in August 2008. Photograph taken by Roger Smith.

Figures 3.4a and e show isopleths of the vertical mass flux, contours of cloud water plus ice, and the rain shaft, characterized by the 0.5 g kg^{-1} contour of rain water (thick black curve) superimposed at 30 and 40 min, respectively. At 30 min the updraught extends to a height of almost 9 km, and at this stage the mass flux is generally positive throughout the cloud, except for the region on the flanks of the updraught where the subsiding branch of the overturning circulation results in some downward motion. A fraction of the condensate that is carried aloft in the updraught grows large enough to fall against the updraught as ice, snow or rain, and subsequently generates a downdraught. By 30 min a large area of rainwater has developed which engulfs most of the cloud. As the rain drops fall into the unsaturated air below cloud base they partially evaporate, cooling the surrounding air and strengthening the downdraught. At 40 min the contour of rain water engulfs the region of negative mass flux, and rainfall reaches the surface.

Figures 3.4b and f show cross sections of density temperature difference at 30 and 40 min, respectively. At 30 min the cloud is largely positively buoyant throughout, whereas at 40 min there is only a small area of positive buoyancy associated with the formation of

ice particles. Cloud water produced by condensation is carried aloft in the updraught, and if it ascends high enough it freezes, thereby generating additional buoyancy through the latent heat of fusion. At 30 min there is a region of negative buoyancy below 2 km, which is in part a result of water loading and in part because of the lifting of stably stratified air below the updraught following the ascent of the warm bubble initiating convection (note that this negative buoyancy extends laterally well beyond the region of water loading). The two areas of positive buoyancy on either side of the cloud are associated with transient subsidence as the updraught penetrates the stably-stratified environmental air and the area of negative buoyancy near the cloud top is associated with the forced ascent of stably-stratified environmental air ahead of the cloud. This time is just prior to that when ice begins to form. By 40 min a large region of ice (dashed green countour) has formed.
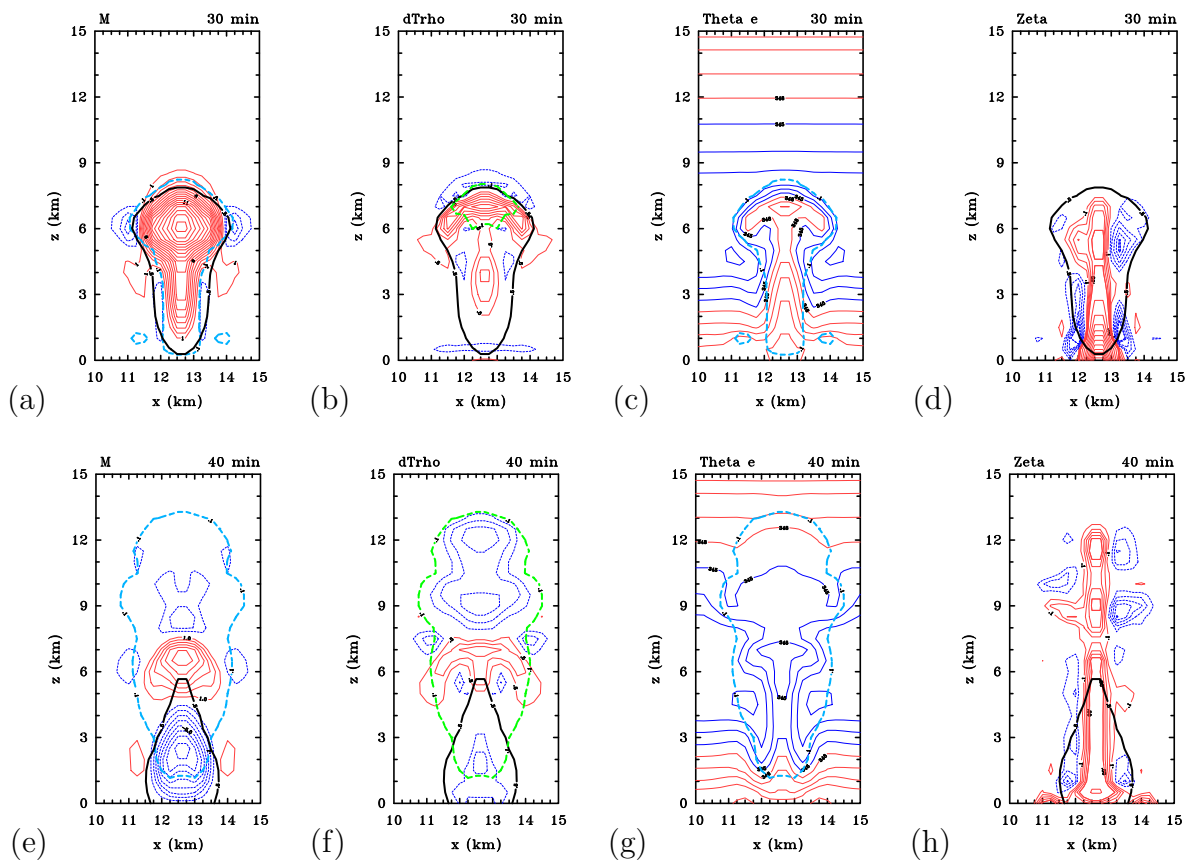
Figure 3.4: Vertical cross sections, as in Figure 3.2, for the control experiment at 30 and 40 min.

In Figure 3.4c the updraught has lifted air with high values of θ_e from low-levels to the mid-troposphere at 30 min. By 40 min (Figure 3.4g) the downdraught has begun to advect air with low θ_e towards the surface.

The cross section of the vertical component of relative vorticity, ζ, at 30 min (Figure 3.4d) indicates a significant amplification of the ambient vorticity extends almost to the

top of the cloud, while the vorticity maximum remains located at low-levels. These findings corroborate those of Wissmeier and Smith (2011). By 40 min the depth of vorticity has increased to just over 12 km, while the surface values have decreased in strength. As the downdraught reaches the surface and diverges laterally outwards, the vorticity near the surface is diluted and advected outwards, leading to a decrease in the amplification at low levels. The evolution of ζ will be examined in more detail in Chapter 4.

3.3.3 Decay phase
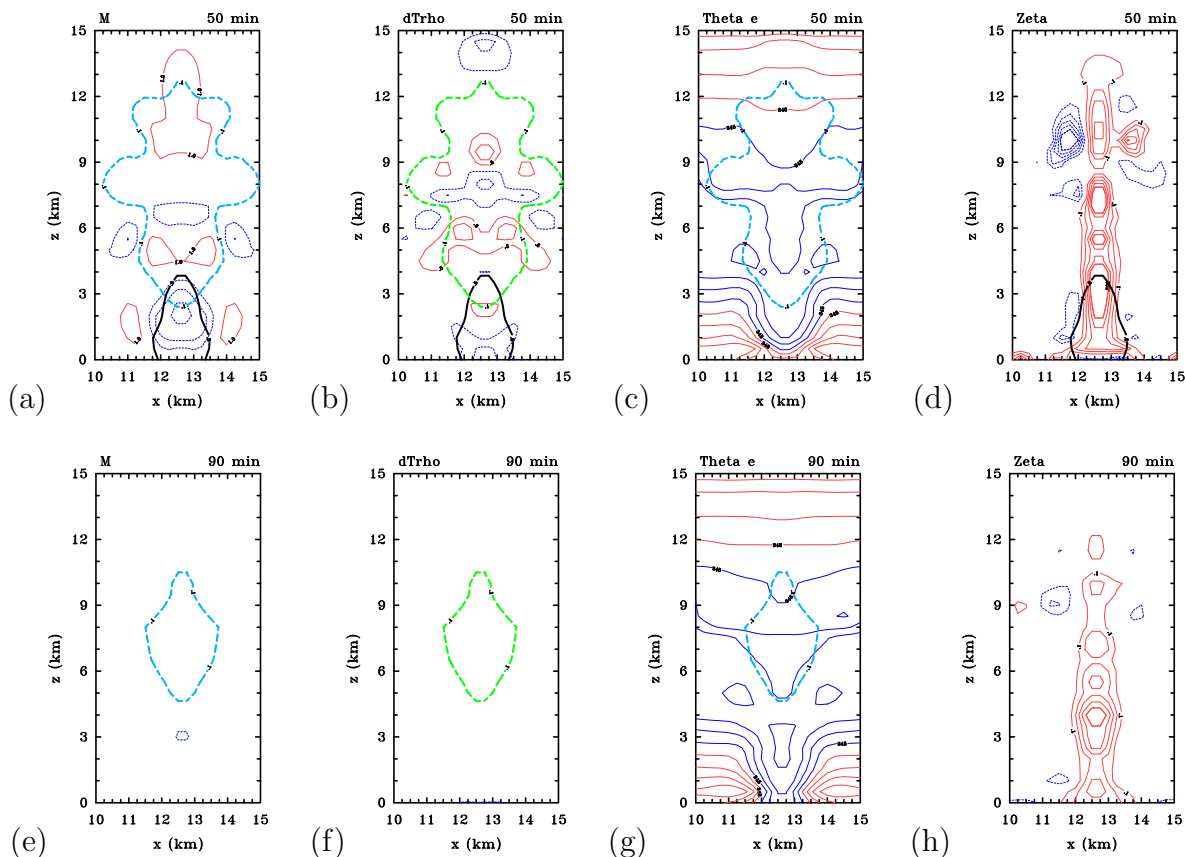
Figure 3.5: Vertical cross sections, as in Figure 3.2, for the control experiment at 50 and 90 mins.

Figure 3.5 show similar vertical cross sections to Figures 3.2 and 3.4 but at 60 and 90 min. At these times, the updraught has all but decayed (panels (a) and (e)), but a plume of enhanced relative vorticity remains within and below the cloud (panels (d) and (h)). The amplified vorticity is a legacy of that generated by stretching during the earlier stages of updraught development, and survives long after the convective cell decays. There is little remaining positive buoyancy in the cloud at 50 min, which is mostly composed of an anvil of ice and a decaying rain shaft that has negative buoyancy (panel (b)). All that

remains at 90 min is the anvil of ice (panel (f)). The θ_e cross section at this time (panel (g)) shows that the plume generated by the updraught has been replaced by one generated by the downdraught, which has brought air with low values of θ_e to the surface.

Of interest is how these structures are modified by the presence of dry air aloft, a topic that is examined in the next chapter. Secondary cells of convection may be triggered along the cold pool's spreading gust front if the air ahead of it is sufficiently unstable. This does not occur in the control experiment, but does in several experiments investigated in Chapter 4 where the environmental sounding is more unstable. In these experiments, the subsequent flow evolution becomes more complicated than that shown in Figures 3.2, 3.4 and 3.5, losing its axisymmetric structure.

3.3.4 Maximum values

Figure 3.6 shows the evolution of the maximum values for the updraught velocity, positive density temperature difference, ice and liquid water content, the amplification of vertical vorticity and the absolute values of the minimum downdraught and negative surface density temperature difference for the control experiment. The updraught has a maximum strength of close to 30 m s^{-1} at roughly 28 min (panel (a)) and then rapidly decays over the next 10 min. Maximum values of over 10 m s^{-1} occur for a period of about 20 min.
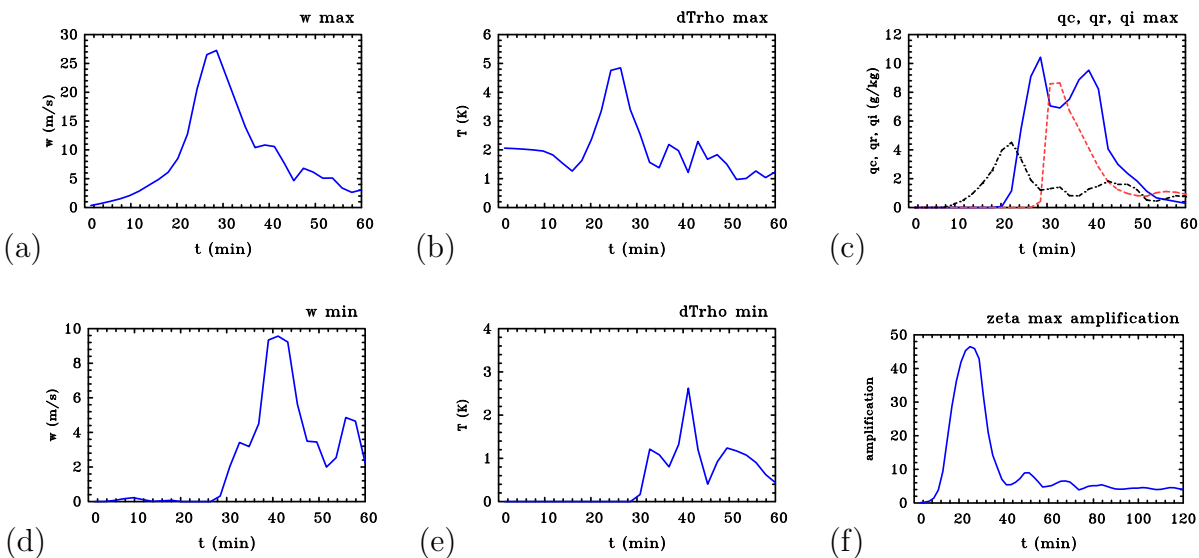
Figure 3.6: Time evolution plots of the maximum values of (a) updraught velocity, (b) positive density temperature difference, (c) ice content (red dashed contour), liquid water (blue solid line) content and cloud condensate (black dash-dot contour) for 60 min; the absolute values of the minimum (d) downdraught velocity, (e) negative density temperature difference at the surface for 60 min; and (f) the amplification of vertical vorticity for 120 min.

The maximum buoyancy, as given by the positive density temperature difference, has a value of almost 5 K[4] occurring at 24 min . The timing of this maximum coincides with the intensifying positive vertical velocity values (panel (a)). The source of this buoyancy is the latent heat released from the condensation of water vapor into cloud and rain droplets. The maximum cloud condensate and rain water content grows rapidly between 20 and 30 min (panel (c)), reaching almost 5 g kg^{-1} and 12 g kg^{-1} at about 20 and 28 min for cloud condensate and rain water content, respectively. The maximum ice content occurs slightly later, just after 30 min, reaching a value of almost 9 g kg^{-1}. The maximum buoyancy associated with the maximum ice content does not match that associated with the water droplet formation, with a maximum buoyancy of just over 2 K occurring after 30 min. In this experiment the buoyancy generated by latent heat of ice formation is countered by the water loading from rain droplets which acts to reduce buoyancy. In experiments where vertical wind shear exists the buoyancy generated by ice formation plays a larger role since the rainfall does not fall directly into the updraught.

The maximum downdraught and the maximum negative buoyancy (panels (d) and (e), respectively) occur at roughly the same time, 40 min. Subsequently, just after 40 min the maximum rain content decays suddenly (panel (c)). The downdraught is driven by water loading and strengthened by the partial evaporation of raindrops as they fall towards the surface.

The vorticity amplification maximum (panel (f)) occurs at roughly 26 min and is close to 50 times the background rate for a duration of about 10 min. The sudden vorticity increase occurs at the same time when the updraught velocity is a maximum (panel (a)). The vertical gradient of the vertical mass flux is responsible for the production of vertical vorticity by the stretching of existing vorticity. The vorticity decays subsequently, although an amplified region of vorticity remains after the updraught decays, lasting until the simulation ends at 120 min. The long lasting vortical amplification becomes very important in simulations where secondary cells develop as further updraughts amplify the enhanced vorticity even further.

3.4   Summary

In summary, the updraught that forms the first convective cell is initiated by the buoyancy of the initial bubble. The updraught develops slowly at first, but increases rapidly in vertical extent and strength as additional buoyancy is generated by the latent heat release of condensation. Eventually a fraction of the condensate that is carried aloft in the updraught grows large enough to fall against the updraught as ice, snow or rain, and subsequently

---

[4]While a temperature excess of 5 K in the tropics may seem unrealistic, it is noted that Houze *et al.* (2009) observed a peak temperature perturbation of around 6 K at a height of 10 km in convection occurring in the tropical depression that became Hurricane Ophelia. Also, it is worth pointing out that Davies-Jones (1974) found virtual temperature excesses of 8 to 10.5 K in balloon soundings recorded within the cores of severe midlatitude thunderstorms in Oklahoma. In these intense updraughts vertical velocities in the range of 16-37 m s^{-1} were recorded. Even larger maximum vertical velocities and temperature excesses were observed in intense thunderstorms in Bluestein *et al.* (1988) and in Heymsfield and Hjelmfelt (1981).

generates a downdraught. As the rain drops fall into the unsaturated air below cloud base they partially evaporate, cooling the surrounding air and strengthening the downdraught. The entire process takes about 20 min, and when the convection decays the air at the surface has low values of θ_e, brought down from the upper levels by the downdraught.

Cross sections of the vertical component of relative vorticity indicate a significant amplification of the ambient vorticity extends almost to the top of the cloud, while the vorticity maximum remains located at low-levels. The amplified vorticity is a legacy of that generated by stretching during the earlier stages of updraught development, and survives long after the convective cell decays.

Chapter 4

Effects of dry air aloft and sensitivity to initial bubble strength

4.1 Introduction

During the weather briefings for the PREDICT experiment, there was much speculation (Roger Smith, personal communication) that Tropical Storm Gaston failed to redevelop because of its weak pouch that enabled dry air to penetrate its core. The presumption was that the dry air in the lower to middle troposphere would strengthen downdraughts from deep convection and flood the boundary layer with low entropy air from above. As discussed in section 1.7, the common perception that dry air generally enhances the strength of convective downdraughts has been challenged recently (James and Markowski 2009).

This chapter aims to answer the questions: if *convective* downdraughts are not strengthened by the presence of dry air, what aspects of the ensuing convection might be detrimental to tropical cyclogenesis? Is it simply the fact that mesoscale downdraughts are strengthened, or is it that by reducing the updraught strength, the dry air reduces the ability of the convection to amplify vorticity?

It is conceivable that a reduction of the ability of the convection to amplify ambient rotation might have a more detrimental effect on tropical cyclogenesis than the effects of downdraughts by reducing the propensity of deep convective cells to aggregate. As a necessary first step, the focus is on the effects of dry air on a single cloud updraught using thermodynamic soundings based on the data for ex-Gaston.

Examined also in this chapter is the dependence of the ensuing convection on the temperature excess of the initial bubble.

4.2   Numerical experiments

The distinguishing features of the ten numerical experiments discussed in this chapter are the environmental sounding used and the maximum temperature excess of the thermal perturbation that initiates the updraught. The soundings examined are a small subset of those obtained from dropsondes launched during the missions into Ex-Gaston on 2, 3 and 5 September, 2010, but span a reasonable range of sounding types in the pouch region. As soundings were limited to the ceiling of the aircraft (about 14 km), they were extended vertically using analysis data in their proximity from the European Centre for Medium Range Weather Forecasts 0.25 degree analyses. A list of all soundings used is presented in Table 4.1. The table lists also the relevant parameters of these experiments including the thermodynamic characteristics of the soundings, their date and time, and the initial temperature perturbation used to initiate convection.

4.2.1   Experiments with idealised soundings

The first three experiments are designed to explore the role of moisture on the dynamics and thermodynamics of the ensuing updraught and downdraught. The thermodynamic sounding used in Experiment 1 is discussed in detail in Chapter 3.

   Experiment 1 serves as a control to compare with Experiments 2 and 3, which have decreasing amounts of mid-level moisture. Experiment 2 has the same moisture profile as that of Experiment 1 from the surface to 2.5 km and above 4.5 km. In the layer between these heights, the mixing ratio is reduced by extending the linear profile of mixing ratio at upper levels down to 2.5 km as shown in Figure 4.1b. The relative humidity for the 'dry' region between 2.5 km and 4.5 km is an average of 66%, compared to 83% for Experiment 1. Experiment 3 is similar to Experiment 2, but the upper-level mixing ratio profile is reduced down to 1.5 km as shown in Figure 4.1b. The relative humidity for the 'dry' region is then 63% compared to 83% for the control. The reduced moisture lowers the TPW values to 59.3 kg m^{-2} for Experiment 2 and 54.8 kg m^{-2} for Experiment 3. The temperature profile of both altered soundings is adjusted slightly to preserve the virtual temperature of the control sounding, ensuring that each sounding has identical CAPE. Experiments based on these soundings are used to investigate sensitivity of the cloud updraught and downdraught to dry air aloft.

4.2.2   Experiments with observed soundings

Experiment 4 is carried out with the observed sounding on which Experiment 1 was based while Experiment 5 is carried out with the sounding at 14:48 UTC, which is one of the driest on that day with a TPW of 43.5 kg m^{-2} (see Smith and Montgomery, 2011, Figure 2.). Again, the flow environment is taken to be quiescent. It is seen that the idealised profiles are broadly realistic: the θ_v-profiles of all soundings are very similar (Figure 4.1a) and the mixing ratios in Experiments 1-3 lie within those of the driest and moistest soundings made on 5 September (Figure 4.1b). The two observed soundings are illustrated by the
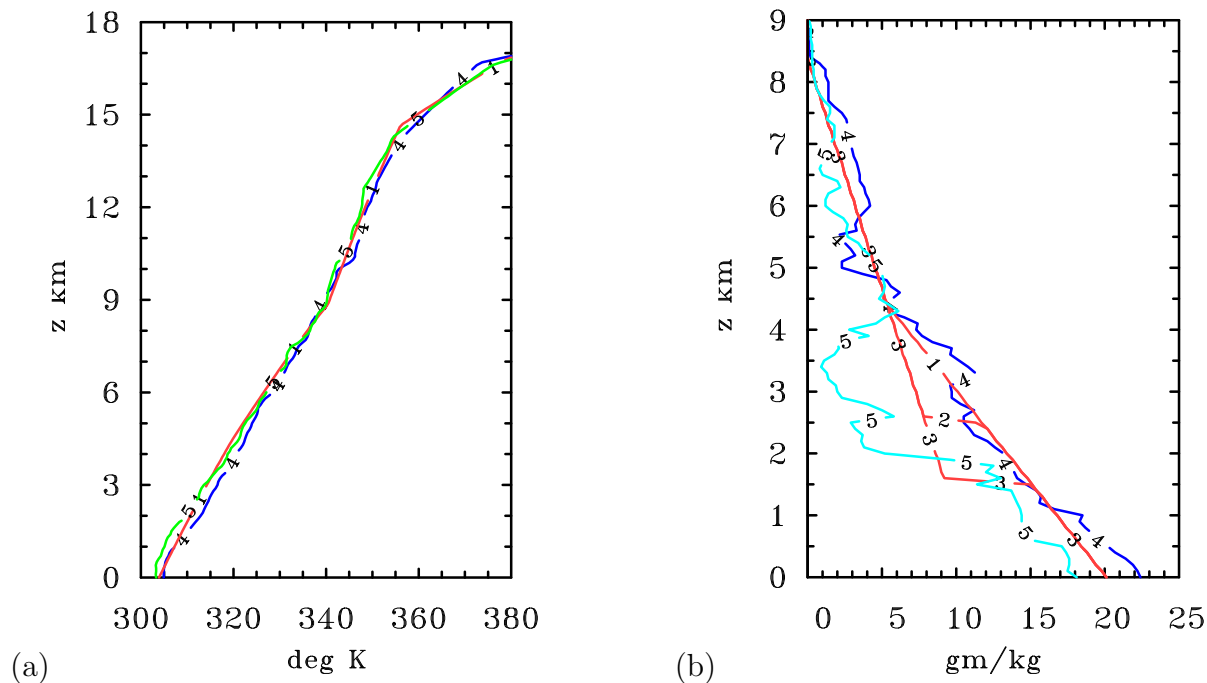
Figure 4.1: Three idealised soundings used for Experiments 1-3 and two actual soundings from ex-Tropical Storm Gaston on 5 September obtained during the PREDICT Experiment. Shown are virtual potential temperature on the left and mixing ratio on the right. Sounding labeled '1' is the control (Experiment 1), while those labeled '2' and '3' are modified versions thereof giving a progressively drier atmosphere at mid-levels (but with the same virtual potential temperature to preserve the CAPE and CIN). The sounding labeled '4' refers to the profile with the highest moisture content in ex-Gaston on 5 September (TPW = 65.2 kg m^{-2}) while that labeled '5' is one of the driest profiles observed on that day (TPW = 43.5 kg m^{-2}).

curves labeled '4' and '5' in Figure 4.1. The sounding in Experiment 5 has a CAPE value of 1145 J kg^{-1}, only a third of that in Experiment 4, and has a CIN of 21 J kg^{-1}. Five additional experiments were carried out using other observed profiles, three to examine the dependence of the ensuing convection on the temperature excess of the initial bubble for a sounding of moderate CAPE (1650 J kg^{-1}), zero CIN, and where the parcel buoyancy is expected to be relatively large at low altitudes (Experiments 6-8); and two with a moderate CAPE (1900 J kg^{-1}) and small CIN (5 J kg^{-1}) to examine the structure of convection where the parcel buoyancy is expected to become appreciable only above 2 km (Experiments 9-10). Further details of these experiments are given in the relevant subsections.

Exp #	Sounding Date	Sounding Time UTC	TPW kg m^{-2}	CAPE J kg^{-1}	CIN J kg^{-1}	ΔT K
1	5/9/10*	18:20	62.3	2770	40	2
2	5/9/10*	18:20	59.3	2770	40	2
3	5/9/10*	18:20	54.8	2770	40	2
4	5/9/10	18:20	65.2	3500	0	2
5	5/9/10	14:48	43.5	1145	21	2
6	2/9/10	17:03	67.1	1650	0	2
7	2/9/10	17:03	67.1	1650	0	1
8	2/9/10	17:03	67.1	1650	0	0.25
9	3/9/10	17:57	58.7	1900	5	2
10	3/9/10	17:57	58.7	1900	5	3.5

Table 4.1: Launch time and details of the ten experiments studied herein. CAPE averaged from the surface to 500 m in J Kg^{-1}, minimum CIN between the surface and 500 m in J Kg^{-1}, and total precipitable water (TPW) in kg m^{-2}. ΔT refers to the strength of the initial thermal perturbation. * Refers to an idealized profile created using dropsonde data from the given date and time as a basis.

4.3 Results

4.3.1 Convective cell evolution

Much of the interest herein is focussed on the life cycle of the first convective updraught triggered by the initial thermal bubble, i.e. the first hour of the simulation. The evolution of the updraught is summarized by time-height cross sections of various quantities at the centre of the domain, where the initial updraught forms. Figure 4.2 shows the cross sections of vertical velocity, w, and density temperature difference, dT_ρ, between the updraught and the environment for Experiments 1-3, respectively. The quantity dT_ρ is a measure of the buoyancy including the effects of water loading (Emanuel 1994, Chapter 2). Figure 4.3 shows cross sections of total liquid water (cloud water plus rainwater) and of total ice content (hail, graupel, snow and ice) for these experiments. Table 4.2 gives details of the updraught and downdraught strength for all experiments. These details include the maximum density temperature difference between the updraught and the environment ($dT_{\rho max}$), the maximum liquid water content (q_{Lmax}), the maximum ice content ($q_{Ice\,max}$), the maximum density temperature difference ($dT_{\rho\,min}$) between the downdraught and the environment, and maximum difference in pseudo-equivalent potential temperature ($d\theta_{e\,min}$) between the downdraught and the environment at the surface.

    In all ten experiments, the flow evolution is similar to that described many times previously (see Chapter 3 and Wissmeier and Smith 2011, section 4.1). In brief, the updraught that forms the first convective cell is initiated by the buoyancy of the initial bubble. The updraught develops slowly at first, but increases rapidly in vertical extent and
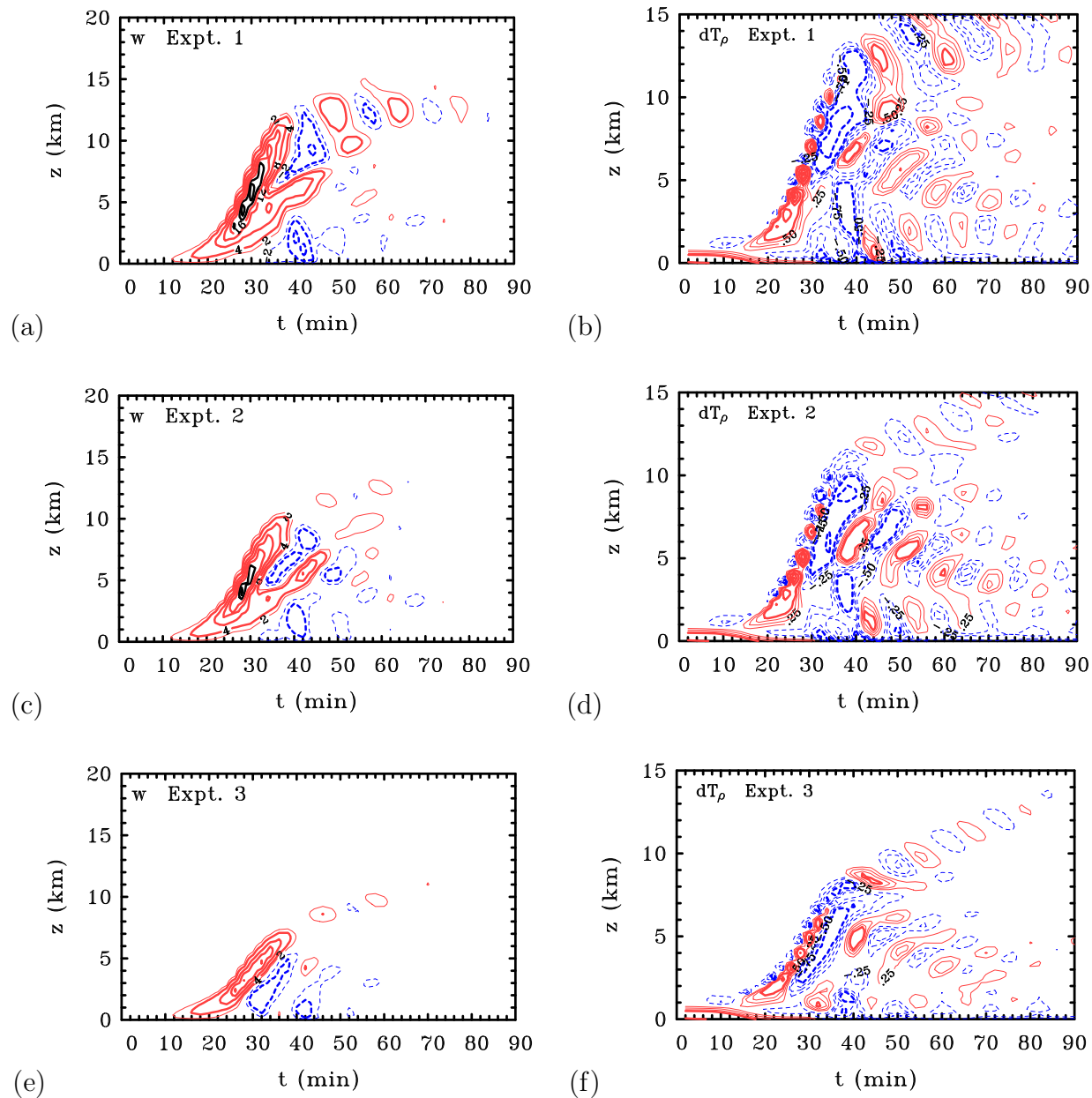
Figure 4.2: Height-time series of maximum vertical velocity, w, (left column) and density temperature difference between the updraught and its environment, dT_ρ, (right column) taken at the centre of the updraught in Experiments 1-3. Contour interval for w, thin contours 2 m s^{-1}, thick contours 4 m s^{-1}. Thick black contours show values above 20 m s^{-1} and are in intervals of 5 m s^{-1}. Solid/red contours show positive values, dashed/blue contours negative values. Contour interval for dT_ρ: thin contours 0.25 K, 0.5 K, 0.75 K, thick contours 1 K.

strength as additional buoyancy is generated by the latent heat release of condensation. Cloud water produced by condensation is carried aloft in the updraught, and if it ascends
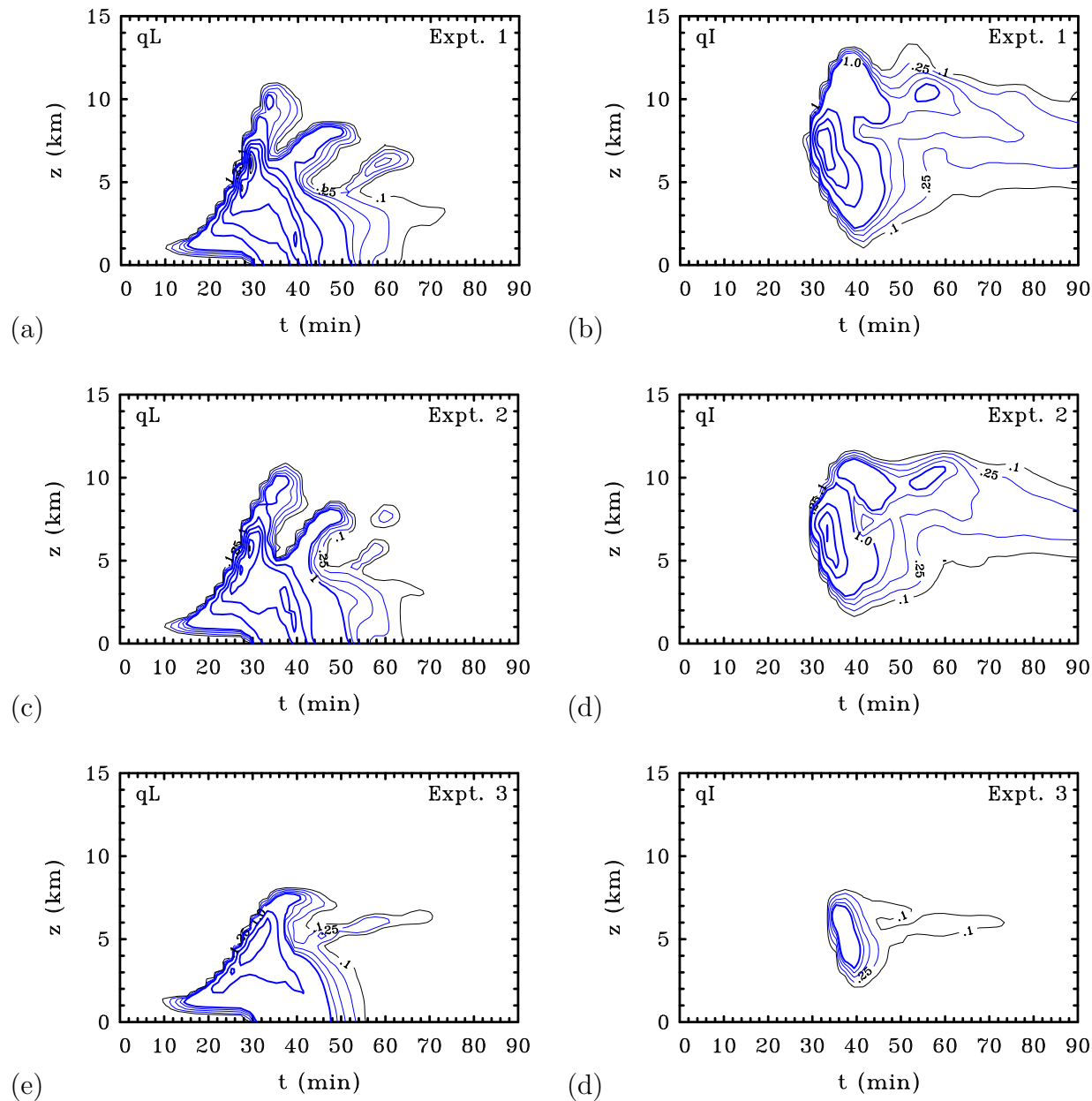
Figure 4.3: Height-time series of maximum total liquid water (cloud water + rain water) taken at the center of the updraught (left panels) and maximum total ice water (snow, ice, hail and graupel) (right panels) in Experiments 1-3. Contour interval: thin contours 0.1, 0.25, 0.5 and 0.75 g kg^{-1}; thick contours 2 g kg^{-1} starting at 1 g kg^{-1}.

high enough it freezes, thereby generating additional buoyancy through the latent heat of fusion. A fraction of the condensate grows large enough to fall against the updraught as ice, snow or rain, and subsequently generates a downdraught. A more detailed description of the evolution of Experiment 1 is given in Chapter 3.

Expt.	w_{max} m s^{-1}	$z(w_{max})$ km	w_{min} m s^{-1}	$z(w_{min})$ km	$q_{L\,max}$ g kg^{-1}	$q_{Ice\,max}$ g kg^{-1}	$dT_{\rho\,max}$ K	$z(dT_{\rho\,max})$ km	$dT_{\rho\,min}$ K	$d\theta_{e\,min}$ K
1	27.1	6.5	-9.6	1.3	11.4	8.6	4.4	4.0	-2.6	-21.0
2	25.0	4.7	-7.6	2.5	10.1	7.1	4.1	3.8	-1.9	-15.4
3	16.5	2.8	-6.9	2.2	6.4	2.2	2.4	3.2	-0.8	-20.2
4	34.0	10.5	-10.9	6.1	16.7	16.6	8.2	8.4	-3.8	-10.0
5	11.4	3.1	-6.3	1.6	6.1	0.3	2.0	1.0	-2.3	-0.5
6	34.0	12.0	-6.0	3.5	15.1	10.1	4.6	11.8	-3.7	-13.2
7	28.0	11.7	-6.0	3.1	14.4	8.1	3.4	4.4	-4.5	-11.4
8	21.0	13.1	-5.3	2.5	12.0	5.5	3.1	4.2	-3.9	-12.4
9	27.7	7.6	-9.9	3.1	9.7	9.1	5.2	5.8	-3.7	-3.3
10	27.7	6.5	-11.4	2.2	13.8	12.2	6.0	6.6	-3.4	-17.5

Table 4.2: Maximum vertical velocity (w_{max}) at the centre of the domain, the height of this maximum ($z(w_{max})$), minimum vertical velocity below 10 km (w_{min}) at the centre of the domain, the height of this minimum ($z(w_{min})$), the maximum liquid water content ($q_{L\,max}$) and the maximum ice content ($q_{Ice\,max}$) in Experiments 1-10. Listed also are the density perturbation temperature ($dT_{\rho\,max}$), the height of this maximum, the minimum surface density perturbation temperature ($dT_{\rho\,min}$), which indicates the strength of the low level cold pool, and the minimum surface pseudo-equivalent potential temperature depression ($d\theta_{e\,min}$).

At this point it is worth drawing attention to the qualitative likeness between the time height cross-sections shown in Figures 4.2 and those of Ferrier and Houze (1989; their Figures 7, 8 and 10) obtained using a one-dimensional cloud model. Since this study does not have to make many of the assumptions that they did, the results in this chapter may be interpreted as support for the realism of their simple model.

4.3.2 The effects of dry air aloft

A comparison of the values of w_{max} for Experiments 1, 2 and 3 in Table 4.2 shows that updraught is significantly weakened in Experiment 3 when moisture is removed from the lowest levels (i.e. below 2.5 km), but less so when these levels remain moist (Experiment 2). The updraughts in Experiments 2 and 3 have maximum values of 25 m s^{-1} and 16.5 m s^{-1} at heights of 4.7 and 2.8 km, respectively. Thus the presence of the environmental layer of dry air reduces the updraught strength as well as the altitude attained by the updraught, the reduction being most dramatic in Experiment 3. The foregoing reductions are a manifestation of the diminished updraught buoyancy (compare panels (b), (d) and (f) in Figure 4.2). Note that the maximum buoyancy in Experiment 1 is nearly double that of Experiment 3 ($dT_{\rho\,max} = 2.4$ K compared with 4.4 K). As expected, there is a monotonic relationship between the maximum vertical velocity and the maximum buoyancy.

The reduced buoyancy may be attributed to the entrainment of the drier air, which decreases the amount of water that condenses and therefore the amount of latent heat

release. The effect is evident in a comparison of the liquid water and ice mixing ratios between the three experiments (see Figure 4.3 and Table 4.2). The maximum liquid water content is 10.1 g kg^{-1} in Experiment 2 and only 6.4 g kg^{-1} in Experiment 3, compared with 11.4 g kg^{-1} in Experiment 1. The lower liquid water content means also that there are fewer water particles to freeze, and therefore less generation of additional buoyancy above the freezing level by the latent heat of freezing. Note that in Experiment 1, a relatively large ice mixing ratio leads to a large vertical velocity maximum at a height of 6.5 km. In contrast, there are comparatively few ice hydrometeors in Experiment 3 as the cloud only ascends slightly above the freezing level, which is about 5 km high.

The foregoing results are supported by those of Experiments 4 and 5. These use observed soundings of temperature and humidity with similar profiles of θ_v to the idealized profile in Experiments 1-3, but have differing amounts of low-level moisture (Figure 4.1). Additional information about these soundings is contained in Figure 4.4, which compares the vertical structure of θ_v, θ_e [1], and saturation pseudo-equivalent potential temperature (θ_{es}) for each of them. The former sounding lies in the region of highest TPW near the centre of circulation and the latter in the drier air to the south of this region (the location of the soundings in relation to the TPW and surface pressure distributions are shown in Figure 2 of Smith and Montgomery 2012).

The vertical lines in Figure 4.4 show the θ_e values for air parcels at the surface and at a height of 100 m above the surface. Since θ_e is conserved[2] for undilute ascent with or without condensation, these lines represent the θ_e of moist air parcels lifted from these levels. Moreover, the distance between the vertical line and the θ_{es}-curve at a given height is roughly proportional to the buoyancy of the lifted air parcel at this height, with the buoyancy being positive when the parcel line is to the right of the θ_{es}-curve. Thus, assuming undilute ascent, the first intersection of the vertical line with the θ_{es}-curve is the approximate LFC and the final intersection is approximately equal to the LNB for the particular air parcel (see Ooyama 1969, Emanuel 1994, Holton 2004). Furthermore, the area between these lines and the θ_{es}-curve in the range between the LFC and LNB is roughly proportional to the CAPE and that between the surface and the LFC is roughly proportional to the CIN.

Time-height cross sections of vertical velocity for Experiments 4 and 5 are shown in Figure 4.5. The maximum updraught and downdraught velocities in Experiment 4 are 34 m s^{-1} and 10.9 m s^{-1}, respectively (see Figure 4.5(a) and Table 4.2). These values are both larger than the corresponding values in Experiment 1, which are 27.1 m s^{-1} and 9.6 m s^{-1}, respectively. The maximum buoyancy, characterized by $dT_{\rho max}$, is larger also (8.2 K compared with 4.4 K). These differences may be attributed to the fact that the mixing ratio is 1-2 g kg^{-1} larger in Experiment 4 below a height of 1 km (Figure 4.1). In contrast, the maximum updraught velocity in Experiment 5 (11.4 m s^{-1}) is less than that in Experiment 3 (16.5 m s^{-1}), the maximum buoyancy is slightly weaker also (2 K compared with 2.4 K). Further, the updraught only just extends above the freezing level so

---

[1]The pseudo-equivalent potential temperature was calculated using Bolton's formula (Bolton 1980).

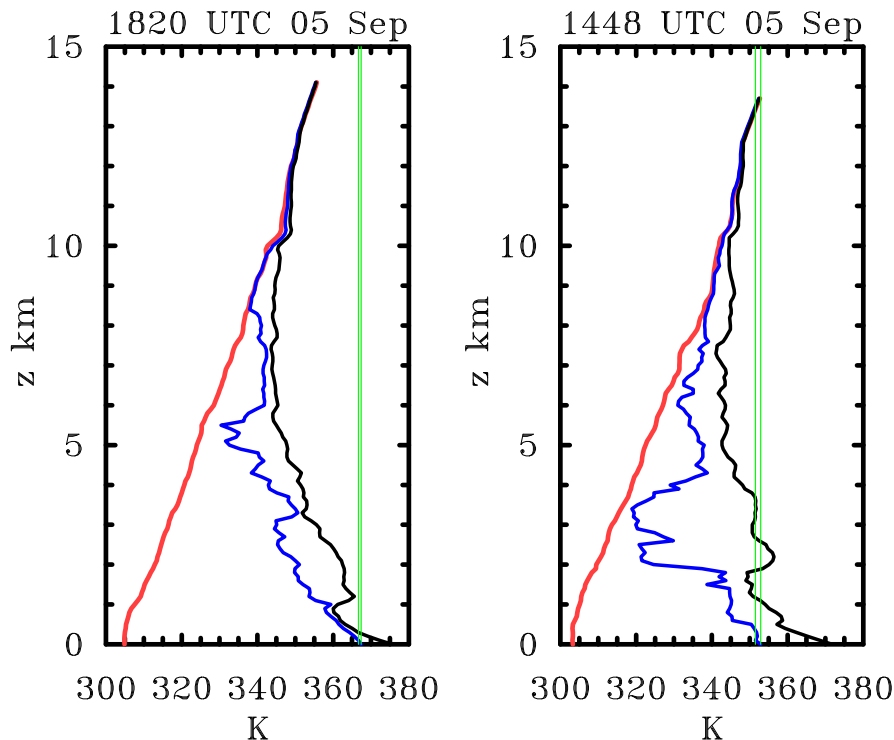[2]It is perhaps worth noting that the numerical model used here only conserves θ_e approximately.

Figure 4.4: Vertical profiles of θ_v, θ_e, and θ_{es} for two soundings made in ex-Gaston on 05 September: (left) 18:20 UTC, and (right) 14:48 UTC. The left (red) curves show θ_v, the middle (blue) curves show θ_e, and the right (black curves) saturated θ_{es}. The location of these soundings relative to the TPW and surface pressure distribution are shown in Figure 1 of Smith and Montgomery (2012). The vertical lines in the figure show the θ_e values for air parcels at the surface and at a height of 100 m above the surface.

that there is little ice produced and little latent heat of fusion released. The downdraught velocity is only marginally less than that in Experiment 3 (6.3 m s^{-1} compared with 6.9 m s^{-1}). These differences are presumably because the sounding in Experiment 5 is drier than that in Experiment 3 in the air layer between about 2 and 4 km and near the surface (see Figure 4.1(b)).

At this point it is worth noting that the maximum vertical velocities in Experiments 1, 2 and 4, which range between 25 m s^{-1} to 34 m s^{-1}, are somewhat high compared with those commonly reported in deep tropical convection, where values in the range 10 m s^{-1} to 25 m s^{-1} are more typical (LeMone and Zipser 1980, Houze *et al.* 2009). The maximum vertical velocities in Experiments 1-4 are comparable to those observed in more intense mid-latitude thunderstorms. Davies-Jones (1974) observed intense updraughts vertical velocities in the range of 16-37 m s^{-1} in balloon soundings recorded within the cores of severe thunderstorms in Oklahoma, while even larger maximum vertical velocities (up to 50 m s^{-1}) were observed in intense thunderstorms in Bluestein *et al.* (1988) and in Heymsfield and Hjelmfelt (1981). The high values found in the experiments performed here, which were
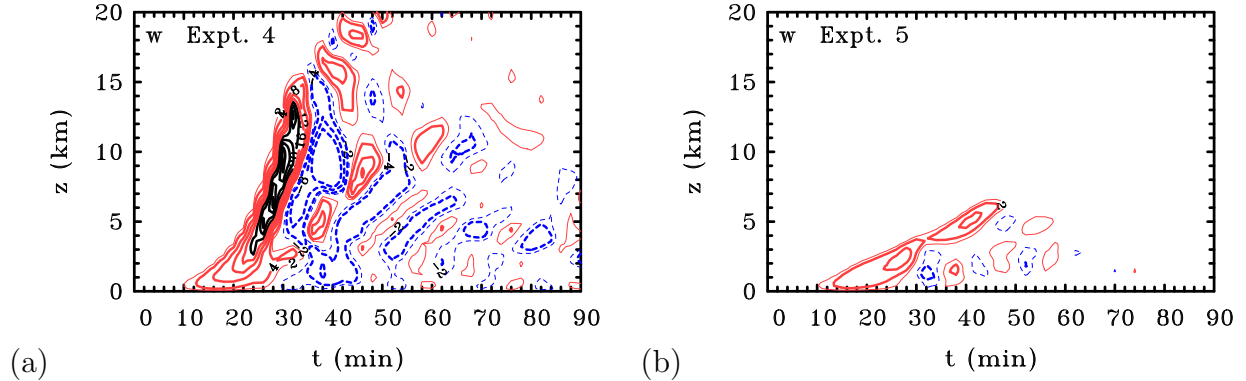
(a)   (b)

Figure 4.5: Height-time series of maximum vertical velocity, w, at the centre of the up-draught in (a) Experiments 4, and (b) Experiment 5. Contour interval for w, thin contours 2 m s^{-1}, thick contours 4 m s^{-1}. Thick black contours show values above 20 m s^{-1} and are in intervals of 5 m s^{-1}. Solid/red contours show positive values, dashed/blue contours negative values. Thick black contours show values above 20 m s^{-1} and are in intervals of 5 m s^{-1}.

only on the axis, are presumably due to the strength of the thermal bubble (2 K), which may be unrealistically large for thermal perturbations over the tropical oceans. When Experiments 1-3 were repeated with a 1.5 K bubble, the maximum vertical velocities were reduced to 22.5 m s^{-1}, 18.7 m s^{-1}, and 8.6 m s^{-1}, but all the conclusions regarding the effects of dry air discussed below were unchanged. However, with a 1 K bubble, convection was not initiated in any of them. A 2 K bubble was chosen so that deep convection would be initiated in all experiments. Finally, it is worth noting also that the maximum observed vertical velocities determined by aircraft penetrations may be expected to have a bias because, for safety reasons, pilots will not normally fly into the most intense updraughts.

Traditional reasoning would suggest that ensuing convection within a relatively dry mid-level environment would lead to comparatively strong downdraughts (e.g., Emanuel 1994). However, this idea is not borne out by the results of the present calculations. Indeed, in Experiments 1-3, the strongest downdraught (9.6 m s^{-1}) occurs in Experiment 1, while the downdraughts become progressively weaker as the environment becomes drier (see Table 4.2). The negative buoyancy of the downdraught characterized by $dT_{\rho\,min}$ diminishes also with increasing dryness, being -2.6 K in Experiment 1, -1.9 K in Experiment 2, and only -0.8 K in Experiment 3.

In the drier environment of Experiments 2 and 3, the negative vertical gradient of θ_e is much larger at low levels than in Experiment 1, especially just above 1 km, where the dry air is introduced (see Figure 4.1b). Thus, the weaker downdraughts in Experiment 3 are able to bring down low-θ_e air into the boundary layer with θ_e values comparable to those in Experiment 1 (note that $d\theta_{e\,min}$ is -21 K in Experiment 1 and -20.2 K in Experiment 3: see Table 4.2). For this reason, the minimum depression in θ_e does not decrease monotonically in Experiments 1-3 and, perhaps not surprisingly, there is not a monotonic relationship between $d\theta_{e\,min}$ and $dT_{\rho min}$ in Table 4.2.

A similar finding concerning downdraught strength to mid-level dryness was described in a recent numerical modelling study of mid-latitude convective systems (both quasi-linear systems and supercells) by James and Markowski (2009). They found that dry air aloft "reduces the intensity of the convection, as measured by updraught mass flux and total condensation and rainfall. In high-CAPE line-type simulations, the downdraught mass flux and cold pool strength were enhanced at the rear of the trailing stratiform region in a drier environment. However, the downdraught and cold pool strengths were unchanged in the convective region, and were also unchanged or reduced in simulations of supercells and of line-type systems at lower CAPE." They noted also that "when dry air was present, the decline in hydrometeor mass exerted a negative tendency on the diabatic cooling rates and acted to offset the favourable effects of dry air for cooling by evaporation. Thus, with the exception of the rearward portions of the high-CAPE line-type simulations, dry air was unable to strengthen the downdraughts and cold pool." Weaker downdraughts would be expected if the water loading, characterized by the sum of liquid water and ice mixing ratios, is decreased. The presence of fewer ice hydrometeors would lead to less cooling due to melting and sublimation and fewer raindrops would lead also to less cooling by partial evaporation below cloud base. These features are confirmed by the experiments carried out here. As seen in Table 4.2 and in the scatter plot of Figure 4.6, the experiments with lower liquid water content in a particular set (Expts. 1-5, Expts 9-10[3]) have weaker downdraughts. In fact, a drier environment leads to weaker updraughts and downdraughts irrespective of the presence of ice hydrometeors. This result was demonstrated by repeating Experiments 1-3 with the ice-microphysics scheme switched off (not shown).
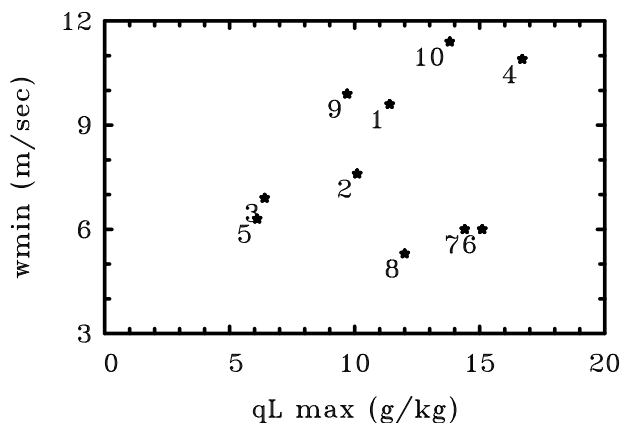
Figure 4.6: Scatter plot of maximum downdraught velocity against maximum liquid water content (marked by star symbols) in Experiments 1-10 (indicated by the numbers).

It was thought by PREDICT forecasters that the failure of ex-Tropical Storm Gaston to redevelop was because a dry Saharan air layer aloft suppressed the system by flooding the boundary layer with cool downdraught air. The dry air was evident in multiple satellite products. The Saharan air layer is considered hostile to Atlantic tropical convection

---

[3]Experiments 6-10 are discussed later in this section.

(Dunion and Veldon, 2004). The experiments described here with dry air aloft suggest an alternative hypothesis for the failure of ex-Tropical Storm Gaston to redevelop. By weakening the updraught strength, the dry air would make the updraught less effective in amplifying vertical vorticity. This effect is examined in the next section.

4.3.3   The amplification of ambient vertical vorticity

Since the pioneering study of Hendricks *et al.* (2004), there is growing evidence that all deep convection, and even convection of moderate vertical extent, produces a significant amplification of existing local vertical vorticity by vortex-tube stretching, even in the absence of ambient vertical shear (Wissmeier and Smith 2011 and references). There is evidence also that this convectively-generated vorticity is important in both the genesis of tropical cyclones (e.g. Hendricks *et al.* 2004, Montgomery *et al.* 2006) and their intensification (e.g. Nguyen *et al.* 2008, Shin and Smith 2008, Fang and Zhang 2010). Such vorticity is able to interact with like-signed patches of vorticity produced by neighbouring convective cells, to be strengthened further by subsequent convection, and to be progressively axisymmetrized by the angular shear of the parent vortex as discussed in Montgomery *et al.* (2006) and Nguyen *et al.* (2008). These findings naturally motivate the question foreshadowed in the introduction: if the most important effect of mid-level dry air on convective clouds is to reduce the updraught strength rather to increase the downdraught strength, is the detrimental effect of dry air on tropical cyclogenesis simply that it reduces the ability of the convection to locally amplify the ambient vertical vorticity? While an answer to this question calls for model simulations in which there are many clouds, it is still pertinent to quantify the effects of dry air on the ability of a single cloud to amplify vorticity.

Wissmeier and Smith (2011) showed that the first updraught produces a large amplification of the background vorticity at low levels and that this vorticity remains after the updraught has decayed. The same occurs in the calculations carried out here as seen in the vertical cross sections of ζ shown in the time-height cross sections of vertical vorticity for Experiments 1-8 shown in Figure 4.7, and in the values for the maximum vertical vorticity (ζ_{max}) as a fraction of the background vorticity (ζ_1) in Table 4.3. The maxima of ζ_{max}/ζ_1 in Table 4.3 and the time of their occurrence, $t_{\zeta_{max}}$, refer to the first convective updraught, which, as noted earlier, forms along the axis. The third and and fourth column of the table list the maximum values for ζ attained *in any location* and their times of occurrence. This is because in Experiments 4 and 6-8, new updraughts are triggered along the gust front produced by the initial cell and these amplify the existing vertical vorticity further.

The maximum amplification by the first updraught in Experiments 1-3 is about 85-88 times the background vorticity and occurs at the surface after about 24 minutes. Perhaps surprisingly, the magnitude of the amplification is insensitive to the maximum updraught strength or vertical extent of the cloud, although the deeper clouds produce an amplification of the vorticity through a deeper layer of the atmosphere (cf panels (a), (b) and (c) of Figure 4.7. An even larger amplification occurs in Experiments 4 and 5 (117 times in the former and 121 times in the latter) despite the large difference in the vertical extent of the updraughts in these two experiments (see Figure 4.2).
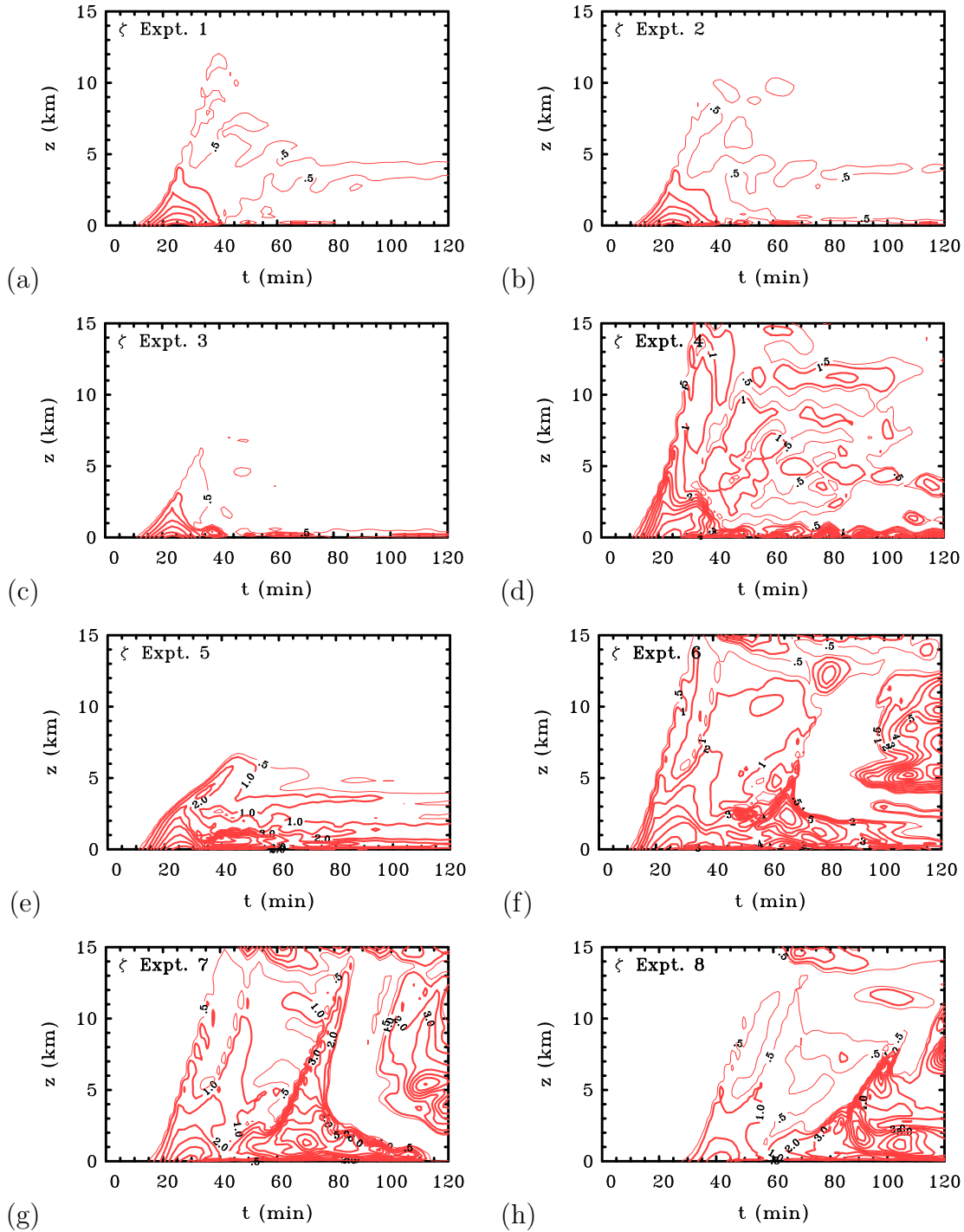
Figure 4.7: Height-time cross sections of maximum vertical component of relative vorticity taken in the centre of the updraught in Experiments 1-8. Contour interval $= 1 \times 10^{-3}$ s^{-1}. Solid/red contours show positive values, dashed/blue contours negative values. The thin solid curve shows the 0.5×10^{-3} s^{-1} contour.

Expt.	ζ_{max}/ζ_1	$t_{\zeta_{max}}$ min	$\zeta_{dom-max}/\zeta_1$	$t_{\zeta_{dom-max}}$ min
1	88	26	-	-
2	88	26	-	-
3	85	24	-	-
4	117	28	197	82
5	121	40	-	-
6	122	28	173	54
7	94	30	180	72
8	48	42	170	96
9	121	28	-	-
10	139	24	-	-

Table 4.3: The degree of amplification of the ambient vorticity by the first updraught cell (ζ_{max}/ζ_1) and the time ($t_{\zeta_{max}}$) at which it occurs, and the degree of amplification of the ambient vorticity over the entire domain ($\zeta_{dom-max}/\zeta_1$) to capture further amplification by secondary cells, should they occur. Also listed is the time of this secondary maximum $t_{\zeta_{dom-max}}$. A blank value indicates that secondary convection was not triggered.

The fact that ζ_{max}/ζ_1 is virtually the same in Experiments 1-3, which all have the same temperature and moisture profiles below a height of 1.5 km, suggests that factors other than the sounding play a role in determining the amplification of vorticity. One possible factor is the strength of the initial thermal perturbation, since this quantity determines the vertical profile of buoyancy and its time variation. In turn, the buoyancy profile determines the vertical gradient of the vertical mass flux that is responsible for the production of vertical vorticity by the stretching of existing vorticity. The similarities between ζ_{max}/ζ_1 in Experiments 4 and 5 would then be attributable to the fact that there are only slight differences between the temperature and moisture profiles at low levels in these experiments. Further investigation of the effects of the strength of the initial thermal bubble is the topic of the next section.

4.3.4 Sensitivity to initial bubble strength

The three Experiments 6-8 all use the sounding made in ex-Tropical Storm Gaston at 17:03 UTC on September 2nd (see left panel of Figure 4.8), but have initial thermal bubbles with temperature excesses of 2 K, 1 K and 0.25 K respectively. The sounding has a lower value of CAPE than that in Experiment 4 (1650 J kg^{-1} compared with 3500 J kg^{-1}), but a slightly larger TPW (67.1 kg m^{-2} compared with 65.2 kg m^{-2}). Moreover, like Experiment 4 it has zero CIN. Thus convection is easily initiated, even with an initial thermal perturbation of 0.25 K. These three experiments are designed to assess the role played by the strength of the initial bubble on the ensuing convection.

The evolution of the updraught in the three experiments is shown in Figure 4.9 and a comparison of maximum updraught strengths is detailed in Table 4.2. As expected, a

decrease in strength of the initial thermal perturbation leads to a monotonic decrease in the maximum updraught strength, the maximum liquid water and ice contents, and the maximum density perturbation temperature. However, the downdraught strength does not change appreciably (by less than 1 m s^{-1}). Even so, in the case with the initial thermal perturbation of only 0.25 K, convection reaches a depth of 15 km. The maximum amplification of vertical vorticity in the three experiments is 122, 94 and 48 times, respectively, i.e. it decreases monotonically with the temperature excess of the initial bubble in line with the arguments given in the previous section.
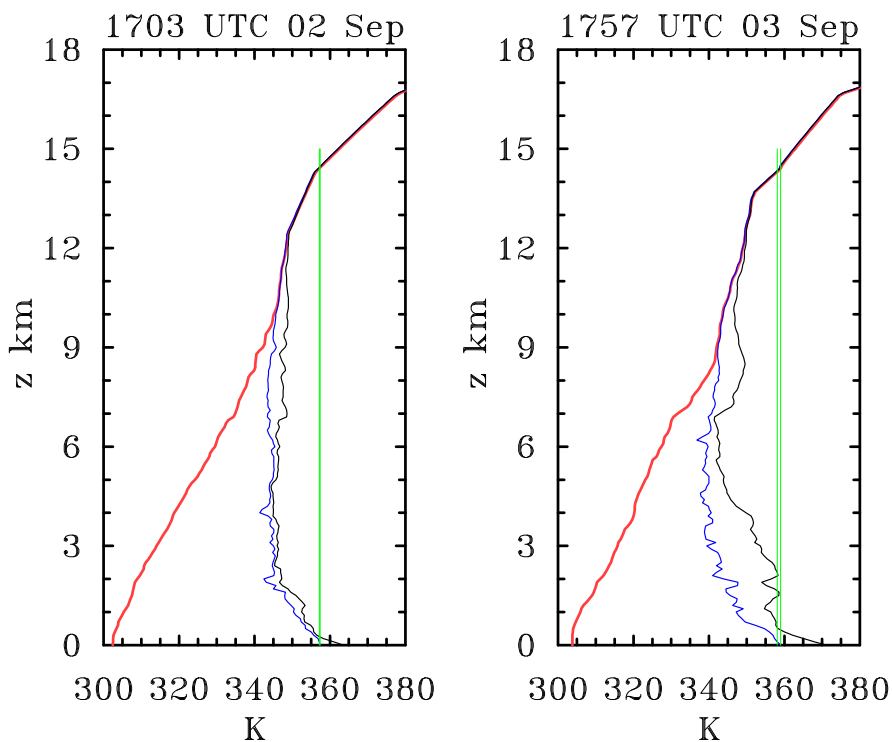

Figure 4.8: Legend as for Figure 4.4, but for the two soundings in ex-Gaston at: (left) 17:03 UTC on 02 September, and (right) 17:57 UTC on 03 September.

As noted above, new updraughts are triggered along the gust front produced by the initial cell in Experiments 4 and 6-8 (note that these experiments have soundings with zero CIN: see Table 4.1). These updraughts amplify the existing vertical vorticity further as indicated in the two right columns of Table 4.3. The amplification of relative vorticity in Experiment 4 increases from 117 times the background ambient value after the first cell to 197 times in subsequent cells. Similar increases are found in Experiments 6-8. In particular, the amplification by secondary cells in Experiment 8 is 170 times the background ambient value, which is over three times the amplification produced by the initial cell. The evolution of the maximum relative vorticity for Exp. 6-8 is shown in Figure 4.9d.

Experiments 9 and 10 use the sounding made in ex-Tropical Storm Gaston at 17:57 UTC on 3 September (see right panel of Figure 4.8), which is typical of those on the
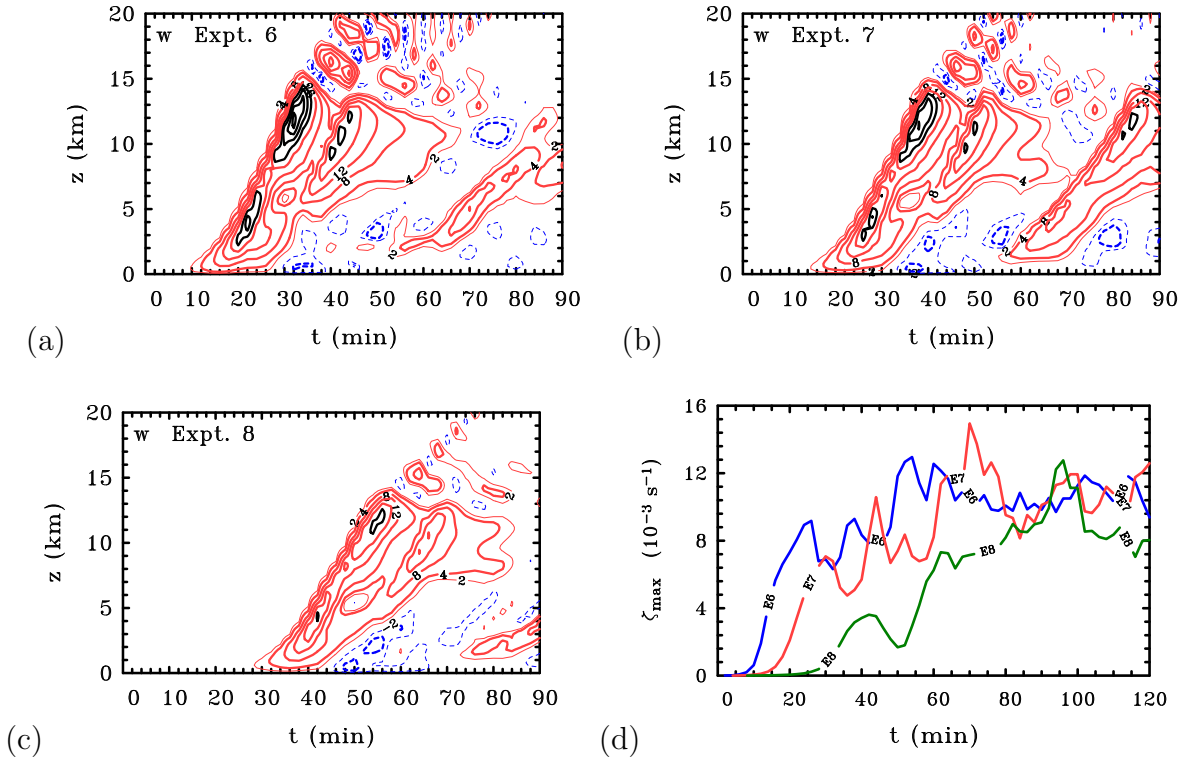
(a)   (b)   (c)   (d)

Figure 4.9: Height-time series of maximum vertical velocity, w, at the centre of the updraught in Experiments 6-8 (panels (a)-(c), respectively). Contour interval for w, thin contours 2 m s^{-1}, thick contours 4 m s^{-1}. Thick black contours show values above 20 m s^{-1} and are in intervals of 5 m s^{-1}. Solid/red contours show positive values, dashed/blue contours negative values. Thick black contours show values above 20 m s^{-1} and are in intervals of 5 m s^{-1}. Panel (d) shows the time evolution of the domain maximum of ζ in these experiments.

periphery of the pouch and has a lower CAPE than in Experiments 6-8 and non zero CIN (see Table 4.2). Experiment 9 is initialized with a 2 K thermal perturbation and in this case the initial updraught produces a 121$\times$ amplification of the vorticity. In contrast, in Experiment 10, which is initialized with a 3.5 K thermal perturbation, the first updraught cell produces a 139$\times$ amplification of the vorticity. As in the previous experiments, there is a monotonic increase in the maximum amplification of vorticity with increasing strength of the thermal perturbation.

4.3.5   Relevance to tropical cyclogenesis

The precise way in which the stretching and thereby amplification of ambient vertical vorticity in clouds impacts tropical cyclogenesis remains a topic of active research. However, a range of numerical simulations to date (e.g. by Hendricks *et al.* 2004, Montgomery *et al.* 2006, Nguyen *et al.* 2008, Shin and Smith 2008, Fang and Zhang 2010) indicate that the

amplification of vertical vorticity by clouds is followed by a merger, aggregation and subsequent axisymmetrization of the remnant vorticity anomalies, leading to an upscale cascade of cyclonic vorticity to form a nascent vortex. The aggregation process is assisted by the system-scale convergence driven by the collective buoyancy of the clouds, themselves. In the presence of ambient vertical shear, the clouds generate anticyclonic vorticity anomalies also by tilting horizontal vortex tubes into the vertical, but the cyclonic anomalies tend to be stronger as a result of the existing cyclonic ambient vorticity. Nevertheless, a segregation mechanism comes into play in which like-signed vorticity anomalies agglomerate, with the stronger cyclonic anomalies ultimately becoming the dominant features. As discussed in the foregoing papers (see e.g. Nguyen *et al.* 2008, section 3.1.5), the merger and segregation processes can be understood broadly in terms of barotropic dynamics, although the finer details of these processes in a baroclinic vortex are still under investigation.

In the context of the foregoing remarks, attention is drawn to a recent paper by Braun *et al.* (2012), which investigates the impact of dry mid-level air on tropical-cyclone intensification (not genesis) using idealized model simulations. The study investigates the potential negative influence of dry mid-level air on intensification, in particular "its role in enhancing cold downdraught activity and suppressing storm development". Specifically, they use the Weather Research and Forecasting model to construct two sets of idealized simulations of tropical-cyclone development in environments with different configurations of dry air. A principal finding is that "dry air slows the intensification only when it is located very close to the vortex core at early times", but that "all storms eventually reached the same steady-state intensity". The study appears to be built on the premise that mid-level dry air should enhance cold downdraught activity, but a finding was that " ... strong downdraught cooling in and of itself does not necessarily inhibit intensification. Instead, it may need to be coupled with the production of storm asymmetries that have the potential to dramatically change the radial distribution of diabatic heating and push the heating peak away from the high vorticity core." Interestingly, no mention is made about the possible effects of dry air on the generation of in-cloud vertical vorticity, which the studies referenced in the paragraph above have shown to be a prominent feature of the tropical-cyclone intensification process.

4.4   Conclusions

A series of numerical experiments were presented, which are designed to isolate the effects of dry air aloft on deep convection, including the efficacy of the convection in amplifying the vertical component of low-level ambient vorticity. Experiments were carried out also to determine the effects of the initial thermal trigger on the ensuing convection. The main focus was on convection that develops within a tropical depression environment using a few thermodynamic soundings acquired during the 2010 PREDICT experiment, or idealized soundings based on these. The initial structure of vertical vorticity was idealized by assuming solid body rotation, but with a value characteristic of disturbances observed during the experiment.

The calculations do not support a common perception that dry air aloft produces stronger convective downdraughts and more intense outflows. Rather, the entrainment of dry air aloft was found to weaken both convective updraughts and downdraughts. Consistent with recent findings of Wissmeier and Smith (2011), growing convective cells amplify locally the ambient rotation at low levels by more than an order of magnitude and this vorticity, which is produced by the stretching of existing ambient vorticity, persists long after the initial updraught has decayed.

The main aims of this chapter were to answer the questions: if *convective* downdraughts are not strengthened by the presence of dry air, what aspects of the ensuing convection might be detrimental to tropical cyclogenesis? By reducing the updraught strength does the dry air reduce the ability of the convection to amplify vorticity?

It was found that significant amplification of vorticity occurs even for clouds of only moderate vertical extent. The maximum amplification of vorticity is relatively insensitive to the maximum updraught strength, and/or the height at which it occurs. Extending the findings of Wissmeier and Smith (2011), it was shown that the degree of amplification is insensitive to the presence of dry air aloft. Thus these results provide an answer to the question posed earlier: does the reduction of the updraught strength by dry air entrainment have the most detrimental effect on tropical cyclogenesis by reducing the ability of the convection to amplify ambient rotation? The results of this chapter suggest that the answer to this question is no. Nevertheless, the reduction in the depth of the strengthened rotation may be an important effect of dry air on the dynamics of tropical cyclogenesis. For example, it might be speculated that a deeper circulation may be less prone to decay, a possibility that merits further investigation.

Another aim of this chapter was to examine the dependence of the ensuing convection on the temperature excess of the initial bubble.

Results for a limited number of different environmental soundings showed that the maximum amplification of vorticity increases monotonically with the strength of the thermal perturbation used to initiate the convection. However, the amount of increase depends also on the thermodynamic structure of sounding. Thus, in reality, the amplification of vorticity may depend strongly on the strength of the trigger that initiates the convection, which is generally not known. It depends also on the low-level thermodynamic structure of the sounding. The current understanding of the way in which the amplification of vertical vorticity by stretching in convective clouds influences tropical cyclogenesis is not yet complete. However, there is mounting evidence that the interaction between the vorticity remnants of clouds promotes an upscale cascade of cyclonic vorticity that is an important component in the formation of a nascent cyclone-scale vortex. This work is conceived as a useful building block for future studies of this issue.

Chapter 5

Effects of ambient vertical and horizontal vorticity

5.1 Introduction

One aim of the present chapter is to examine the role of a deep layer of negative vertical shear overlying a shallow layer of positive vertical shear on storm morphology. This pattern of shear arises in the tangential wind direction in tropical cyclones, although the complete boundary-layer flow in a tropical cyclone is not unidirectional.

A second aim is to extend that of Wissmeier and Smith (2011) by investigating and quantifying the combined effects of both horizontal and vertical wind shear on deep convection that develops in a thermodynamic environment typical of a tropical depression. Particular attention is focussed on the generation of vertical vorticity by convection and the role of boundary layer shear.

A third aim of this chapter is to re-examine the mechanisms involved in storm splitting discussed by Rozoff (2007), giving particular attention to vertical vorticity generation. Since there is observational evidence for the existence of supercell convection in tropical storms (e.g. Gentry *et al.* 1970, Black 1983), it may be presumed that splitting is a relevant process in these systems also.

This chapter is organized as follows. In section 5.2 a brief description of the configuration of the experiments is given. The results of experiments performed with purely vertical shear are presented in Section 5.3. In Sections 5.4 and 5.5 storm splitting is investigated in experiments with a background of pure vertical shear and pure horizontal shear, respectively. The effects of combined horizontal and vertical shear are examined in Sections 5.6 and 5.7, with Section 5.7 focussing on splitting events. The conclusions are given in Section 5.8.

5.2   Experimental setup

5.2.1   Model configuration

The experiments use the same model configurations as those of Chapter 4. The horizontal domain size is 50 km × 50 km with a uniform horizontal grid spacing of 250 m. The vertical domain extends to a height of 28 km with the vertical grid interval stretching smoothly from 120 m at the surface to 1000 m at the top. There are 50 grid levels in the vertical, 8 of which are below 850 mb. The large time step is 3.7 seconds and the integration time is 2 h. There are 8 small time steps per large time step to resolve fast-moving sound waves. The default "open" boundary conditions are used at the lateral boundaries. A sponge-layer is implemented in the uppermost 2 km to inhibit the reflection of gravity waves from the upper boundary. All experiments include warm rain physics, while one experiment implements an ice microphysics scheme also.

5.2.2   The numerical experiments

A total of ten numerical experiments are performed, details of which are summarized and compared in Table 5.1. The first three experiments examine the role of pure vertical shear, the fourth the role of pure horizontal shear, and the remainder the combined effects of horizontal and vertical shear. Further details about the experiments and their objectives are given in the relevant sections.

Exp	microphysics	horiz. shear	f	vertical shear	sounding
1	warm rain	none	0	noBL profile	standard
2	warm rain	none	0	BL profile	standard
3	warm rain	none	0	BL profile*	unstable
4	warm rain	$3\zeta_o$	0	none	unstable
5	warm rain	ζ_o	0	standard	standard
6	warm rain	ζ_o	$\frac{1}{2}\zeta_o$	standard	standard
7	warm rain	ζ_o	ζ_o	standard	standard
8	rain + ice	ζ_o	0	standard	standard
9	warm rain	none	0	standard*	unstable
10	warm rain	ζ_o	0	standard*	unstable

Table 5.1: Details of the ten experiments studied herein. ζ_0 has the value 3×10^{-4} s^{-1}. (*) refers to the wind profile in Experiments 3, 9 and 10, which are altered to include increased low-level vertical shear. The equations for the different types of vertical shear are given in section 5.2.3. Experiments 3, 4, 9 and 10 use a different environmental sounding which is more unstable than the standard sounding. The thermodynamic soundings are discussed in Section 5.2.4.

5.2.3 Background wind profiles

In all experiments, the background flow is in the meridional (y-) direction of a rectangular Cartesian coordinate system, (x, y, z), with z pointing vertically upwards. The background wind profiles for Experiments 1-3 have vertical shear only and are shown in Figure 5.1. The profiles are given by the formula:

$$V(z) = \begin{cases} V_s + (V_m - V_s) \sin\left(\frac{\pi z}{2h}\right) & \text{for } z \leq h \\ V_m \cos\left(\frac{\pi(z-h)}{2H}\right) & \text{for } z \geq h \,, \end{cases} \tag{5.1}$$

where V_m is 20 m s^{-1}, $H = 15$ km and other parameters differ between experiments. Above 15 km, the wind speed is set to zero. In Experiment 1, V_s is equal to $0.7V_m$ and $h = 0$, the latter giving the maximum wind speed at the surface. In this case only the cosine profile applies and the wind profile has negative vertical shear at all heights. In Experiment 2, $h = 1$ km and $V_s = 0.7V_m$. In this case, the cosine profile applies above a height of 1 km and the sine profile below to represent a boundary layer with positive vertical shear. Experiment 3 is similar to Experiment 2, but has $V_s = 0.5V_m$ and therefore a larger positive shear in the boundary layer.
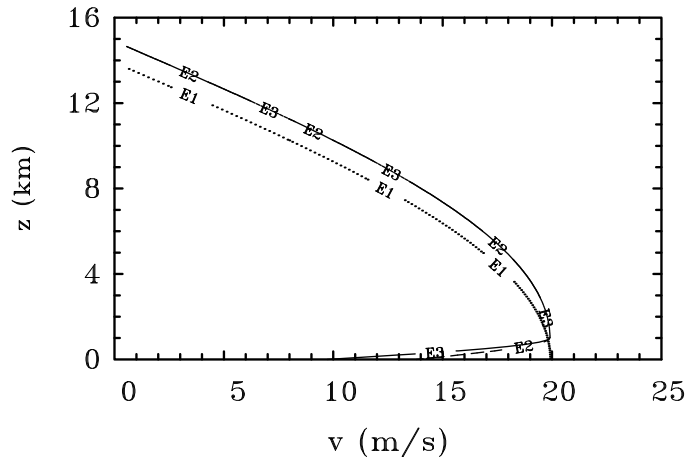
Figure 5.1: Schematic of the background wind field used for Experiments 1-3. The dotted curve denotes V for Experiment 1, dashed curve for Experiment 2 and the solid curve for Experiment 3.

The background wind profile for Experiment 4 is given by the formula:

$$V_o(x) = 3\zeta_o x, \tag{5.2}$$

where $\zeta_o = 3 \times 10^{-4}$ s^{-1}, a value typical of that in a tropical depression[1].

---

[1]See Wissmeier and Smith 2011, section 2.3.

The background wind profile for Experiments 5-10 is shown in Figure 5.2. This idealized profile is chosen to extend the results of Wissmeier and Smith (2011) and is given by the formula:

$$V(x, z) = V_o(x)[1 - b \exp(-az)], \tag{5.3}$$

where $b = 0.5$, $a = -\log(0.05/b)/2000$ m and $V_o(x) = \zeta_o x$. The wind speed increases monotonically with z from a value $0.5V_o(x)$ at the surface reaching 95% of V_o at a height of 2 km. For simplicity, above this height, the wind has essentially uniform horizontal shear only.

A uniform flow is added to the wind profile in all experiments to keep the convection near the centre of the computational domain. The value of this flow is determined by trial and error and is different for each experiment.
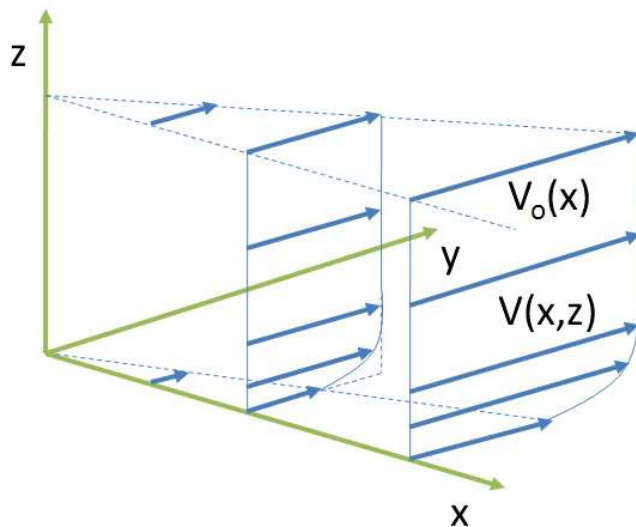

Figure 5.2: Schematic of the "standard" background flow used for Experiments 5-10. The domain is 50×50 km and the thermal bubble used to initiate convection is located at the centre of the domain.

5.2.4   Thermodynamic soundings

Experiments 1-2 and 5-8 use the idealized thermodynamic sounding shown in Figure 5.3a. This sounding is similar to that used in Chapter 3, with piecewise-linear profiles of virtual potential temperature, θ_v, and mixing ratio, r, but it is slightly drier at low levels. Accordingly, the CAPE is less than that of the sounding used in Chapter 3 (2080 J kg^{-1} compared with 2770 J kg^{-1}). The construction of both soundings is based on an observed sounding made near the centre of the low-level circulation ex-Tropical Storm Gaston on 5 September 2010 during the PREDICT experiment (see Smith and Montgomery 2012,

Figure 6 therein). This region of ex-Gaston was one of high TPW, high CAPE and low CIN.

The sounding used here has a minimum CIN of 40 J kg^{-1} and a TPW value of 59.1 kg m^{-2}. In the lower half of the troposphere, the idealized sounding is more moist than the mean tropical sounding of Dunion and Marron (2008), but is much drier in the upper troposphere. In contrast, the temperature structure is close to that of the mean tropical sounding.
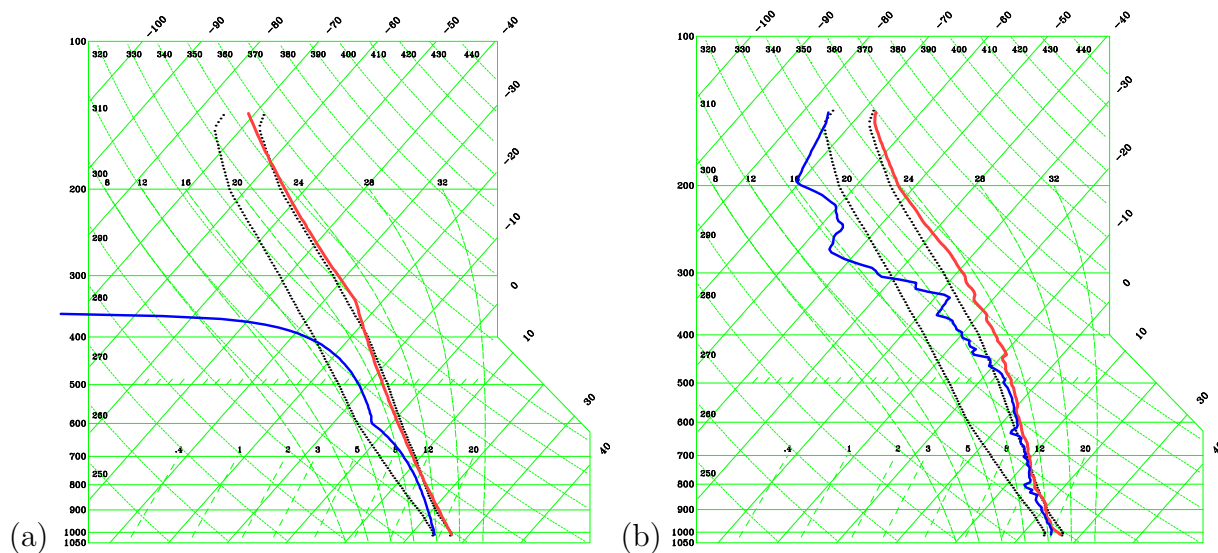

Figure 5.3: Skew-T log-p diagram showing the temperature (right solid curve) and dew point temperature (left solid curve) of the: (a) standard sounding and (b) the PREDICT sounding from September 2nd, 17:03 UTC. For comparison, the dotted curves show the temperature (right curve) and dew point temperature (left curve) for the mean tropical sounding of Dunion and Marron (2008).

A prerequisite for storm splitting is a sufficiently large low-level vertical shear. However, for a given sounding, large vertical shear tends to inhibit convection because the initial thermal becomes elongated and weakened. Therefore, in a strongly-sheared environment, a particularly unstable sounding may be necessary to initiate convection. An example of such a sounding is one observed during the PREDICT experiment, which was used in Experiment 6-8 of Chapter 4. This sounding, shown in Figure 5.3 (b), has moderate CAPE (1650 J kg^{-1}), but zero CIN, and a TPW value of 67.1 kg m^{-2}. In Experiment 8 of Chapter 4, it was possible to initiate a deep convective updraught with an initial warm temperature excess of only 0.25 K. This sounding is used in Experiments 3, 4, 9 and 10 because the CIN of the standard sounding used in the other experiments is too large for convection to be triggered at larger magnitudes of vertical shear.

5.2.5 Initiation of convection

Convection is initiated by a symmetric thermal perturbation with a horizontal radius of 5 km and a vertical extent of 1 km as in previous chapters. The temperature excess has a maximum at the surface at the centre of the perturbation and decreases monotonically to zero at the perturbation's edge. The perturbation centre coincides with the centre of the domain. In general, the details of the ensuing convection such as the maximum updraught strength and the updraught depth will depend on the spatial structure and amplitude of the thermal perturbation.

5.3 Uni-directional vertical shear with and without boundary-layer wind

Experiments 1-4 are designed as a preliminary step towards determining the combined effects of ambient horizontal and vertical shear on vertical vorticity production in tropical convection. In Experiments 1-3 cases of convection developing in an environment with uni-directional vertical shear are examined, and in Experiment 4 the development in an environment of pure uniform *horizontal* shear is examined, in all cases with no background rotation. In this section Experiments 1 and 2 are discussed, and Experiments 3 and 4 are examined in sections 5.4 and 5.5, respectively.

Experiment 1 serves as a control experiment: it has maximum wind speeds at the surface and a negative vertical shear from the surface to the upper troposphere, characteristic of the wind structure in a warm-cored vortex. Experiment 2 is a little more realistic and designed to investigate the additional effects of a boundary-layer wind profile where the wind speed increases with height to a maximum near a height of 1 km before declining. Therefore the horizontal vorticity changes from positive to negative at this height, which is near the top of the boundary layer. In other respects the experiment is the same as Experiment 1.

Details of the maximum updraught and downdraught strength at selected heights are given in Table 5.2, while those of the maximum and minimum vertical vorticity at selected heights are given in Table 5.3 for all experiments. The imposition of a boundary-layer wind profile has a dramatic effect on the vertical velocity: whereas in Experiment 1, w_{max} is 26.8 m s^{-1}, in Experiment 2 it is only 15.5 m s^{-1} (Table 5.2). Moreover, in Experiment 2, the updraught barely extends above a height of 9 km, the maximum vertical velocity at a height of 9 km, $w9_{max}$, being only 1 m s^{-1} at 70 min. In addition to much stronger updraught, the maximum downdraught strength in Experiment 1 (6.9 m s^{-1}) is more than twice that in Experiment 2 (3.3 m s^{-1}).

To help interpret the foregoing results another two experiments were performed (results not shown in Table 5.2), one where the layer of positive vertical shear is confined to the lowest 500 m instead of the lowest 1 km, essentially doubling the amount of vertical shear in the lowest 500 m compared to Experiment 2. In the other experiment, the wind profile in Experiment 1 above a height of 1 km is extrapolated linearly to the surface so that

Expt.	w_{max}	w_{min}	$w2_{max}$	$t(w2_{max})$	$w5_{max}$	$t(w5_{max})$	$w9_{max}$	$t(w9_{max})$	$w2_{min}$	$t(w2_{min})$
			m s^{-1}	min	m s^{-1}	min	m s^{-1}	min	m s^{-1}	min
1	26.8	-6.9	10.8	26	25.3	30	6.1	44	-3.3	40
2	15.5	-3.3	6.2	38	14.2	48	1.0	70	-1.7	40
3	16.5	-7.8	13.2	120	15.6	110	13.2	120	-5.9	110
4	20.1	-6.8	13.6	20	16.5	26	11.5	46	-5.5	28
5	23.8	-6.4	9.4	28	21.5	34	4.5	48	-2.9	34
6	23.2	-6.6	9.6	28	20.8	34	4.7	48	-2.7	40
7	23.6	-6.4	9.6	28	21.4	34	5.3	48	-2.6	40
8	26.1	-8.3	11.4	26	23.4	30	4.5	44	-4.4	42
9	18.7	-7.6	13.6	52	16.4	114	14.9	52	-6.6	98
10	21.6	-8.1	14.8	104	17.7	102	15.3	102	-7.0	84

Table 5.2: Maximum vertical velocity, wN_{max}, and minimum vertical velocity, wN_{min}, at a height of N km and the times at which they occur, $t(wN_{max})$ and $t(wN_{min})$, respectively in Experiments 1-10. The first two columns display the maximum and minimum velocities throughout the domain and the two hour integration time.

the maximum wind speed occurs at the surface and there is everywhere uniform negative shear. In the first of these experiments no convection occurred. The reason is because the increased low-level shear deforms the initial thermal bubble so that it becomes too weak to generate convection. The second of these experiments produces a similar vertical velocity maximum to that found in Experiment 2. Thus, low-level vertical shear weakens the initial thermal before convection occurs whether or not the shear is positive or negative. The weakening depends only on the magnitude of the shear. Note that Experiment 1, which has little vertical shear in the lowest 1 km, produces the strongest updraught. The weakening of the thermal bubble by shear is confirmed by height-time plots of the maximum temperature perturbation in the different experiments at early times (not shown).

Figure 5.4 shows time-height cross sections of maximum[2] vertical vorticity in Experiments 1 and 2, while details of the maxima and minima at selected heights are given in Table 5.3.

In Experiment 1, the vertical gradient of V is small from the surface to around 2 km (Figure 5.1), whereupon there is very little horizontal vorticity available to be tilted into the vertical. This fact explains why values of vertical vorticity are weak at low levels in Figure 5.4(a). There is significant vertical shear above a height of 2 km so that tilting of

---

[2]The evolution of the updraught associated with the rising thermal bubble is similar to that described in Chapter 3, although the depiction here is slightly different. In the previous chapters, there was no ambient vertical shear so that the first convective cell was upright and axi-symmetric about its central axis. This feature allowed the depiction of the evolution of updraughts and downdraughts as height-time series along this axis without ambiguity. The presence here of an ambient vertical shear means that updraughts and downdraughts are tilted so that the extrema of vertical velocity and vertical vorticity occur at different spatial locations at different times. This feature which makes a single cross-section for updraughts and downdraught extrema or for positive and negative vorticity inappropriate. Plots of the minimum vertical vorticity are omitted in this section because, in the absence of background rotation or horizontal wind shear, they are a mirror image of the maximum plots.
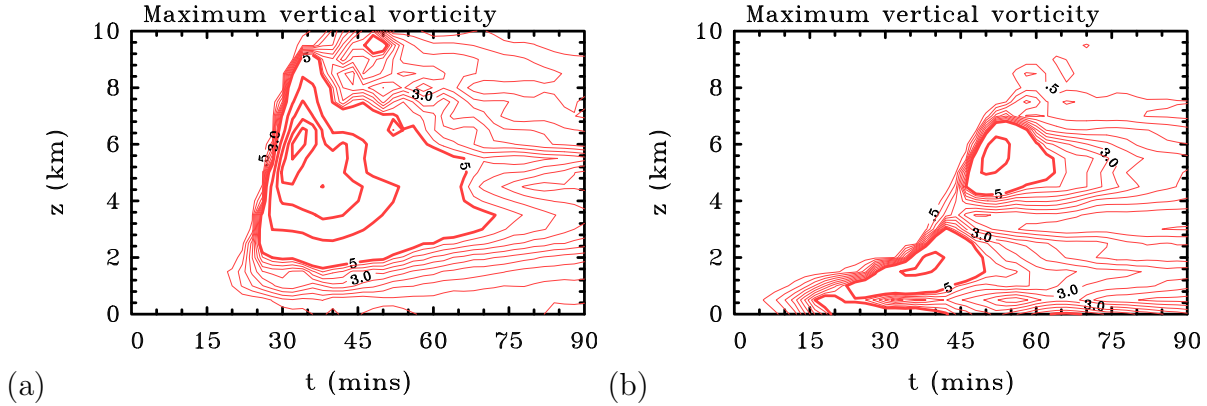
Figure 5.4: Time-height series of maximum vertical vorticity in Experiments: (a) Experiment 1 and (b) Experiment 2. Contour interval: thin contours 0.5×10^{-3} s^{-1} to 4.5×10^{-3} s^{-1}; thick contours 5×10^{-3} s^{-1}.

horizontal vorticity by the updraught leads to values of vertical vorticity there that are much larger. Note that $\zeta_{max} = 2.6 \times 10^{-2}$ s^{-1} at a height of 6.5 km (see Table 5.3).

Expt.	ζ_{max} 10^{-3} s^{-1}	$z(\zeta_{max})$ km	$\zeta 0.5_{max}$ 10^{-3} s^{-1}	$t(\zeta 0.5_{max})$ min	$\zeta 1_{max}$ s^{-1}	$t(\zeta 1_{max})$ min	$\zeta 4_{max}$ 10^{-3} s^{-1}	$t(\zeta 4_{max})$ min	$\zeta 1_{min}$ 10^{-3} s^{-1}	$t(\zeta 1_{min})$ min	$\zeta 4_{min}$ 10^{-3} s^{-1}	$t(\zeta 4_{min})$ min
1	26.2	6.5	1.0	40	2.9	34	18.9	42	-2.9	34	-18.9	42
2	12.2	6.0	5.6	20	8.1	34	3.6	54	-8.1	34	-3.6	54
3	39.4	8.0	22.4	46	29.3	56	31.9	104	-29.3	56	-31.9	104
4	32.7	7.0	24.8	22	23.4	24	20.5	72	-13.7	74	-29.5	40
5	20.0	3.5	8.6	24	12.2	30	19.9	32	-11.5	30	-23.4	32
6	21.6	4.0	13.1	22	14.6	30	21.6	32	-9.4	28	-19.9	32
7	24.0	0.0	15.2	24	17.6	28	20.0	32	-8.2	28	-19.6	32
8	22.2	4.5	10.6	22	11.9	26	21.2	30	-11.9	44	-27.2	30
9	35.2	1.5	19.5	85	28.2	60	31.0	34	-28.2	60	-31.0	34
10	37.5	4.0	19.3	26	27.3	56	37.5	90	-30.8	46	-34.7	110

Table 5.3: Maximum of the vertical component of relative vorticity, ζN_{max}, at heights N of 500 m, 1 km and 4 km and the times at which they occur, $t(\zeta N_{max})$, in Experiments 1-10. Shown also is minimum of this vorticity component at a height of 1 km and 4 km, together with the time at which they occur.

In Experiment 2 there is positive vertical shear below a height of about 1 km and negative shear above. Thus, the sign of background horizontal vorticity reverses at this height and there is an elevated layer in which the magnitude of the horizontal vorticity is small and hence the vertical vorticity production by tilting is small. For this reason, there is an intermediate layer centred around 4 km in height with small vertical vorticity values in Figure 5.4b.

Figure 5.5 shows horizontal cross sections of the vertical component of relative vorticity for Experiment 1 and 2 at 30 min at a height of 1 km and at 54 min at a height of 6 km (left and middle panels). In Experiment 1 the background horizontal vorticity does not change sign with height, but the vorticity generated at low levels is much weaker than in

the middle troposphere. Again this is due to the relatively small amount of background horizontal vorticity available for tilting because of the small vertical gradient of V in the wind profile used in this experiment (compare with the low-level plot in Figure 5.4a).
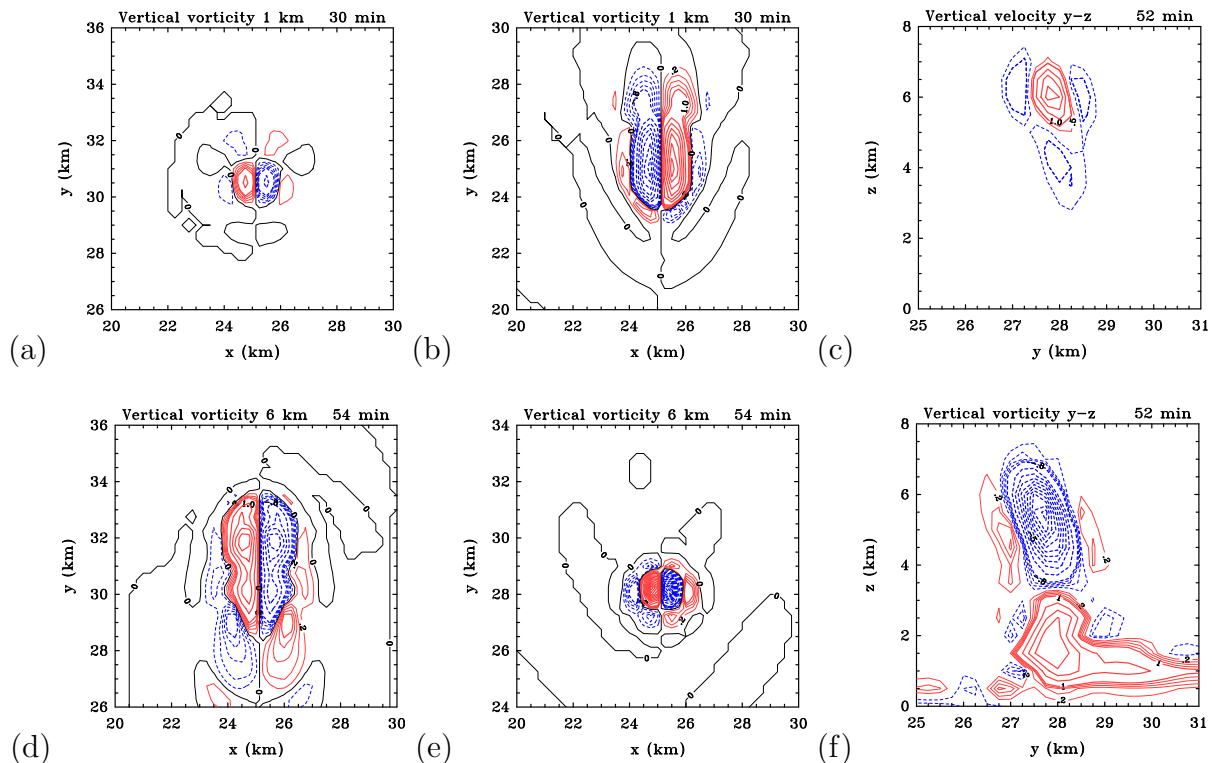

Figure 5.5: Horizontal cross sections of maximum vertical vorticity in Experiment 1 (left) and Experiment 2 (middle) at: (a, b) 30 minutes at a height of 1 km and (d, e) 54 minutes at a height of 6 km. Contour interval: thin contours 2×10^{-4} s^{-1} to 8×10^{-4} s^{-1}; thick contours 1×10^{-3} s^{-1}. Solid (red) contours positive, dashed (blue) contours negative. The thin black curve shows the zero contour. Panels (c) and (f) show vertical cross sections (y-z) at 52 min for Experiment 2 of: vertical velocity (c), and vertical vorticity (f), through the center of the low level positive vorticity anomaly. Contour interval: vertical velocity in thin contour 0.5 m s^{-1}; thick contours 1 m s^{-1}, vertical vorticity thin contour 2×10^{-4} s^{-1} to 8×10^{-4} s^{-1}; thick contours 1×10^{-3} s^{-1}. Solid (red) contours positive, dashed (blue) contours negative.

Below a height of 1 km in Experiment 2, tilting by a convective updraught creates a vertical vorticity dipole with a negative vorticity anomaly to the left of the mean flow (which is in the y-direction) and positive one to the right. Above 1 km, the vorticity dipole is reversed with positive vorticity to the left of the flow direction and negative to the right. Figures 5.5(c) and (f) show y-z cross sections of vertical velocity and vertical vorticity through the centre of the low-level positive vorticity anomaly at 52 min for Experiment 2. At this time the updraught has a maximum at a height of 6 km, but there is a region of subsidence below, centred at a height of 4 km. There are regions of subsidence also

on each side of the updraught. The latter are associated with the downward branch of the rising thermal, while the downdraught centred at a height of 4 km is associated with precipitation. Panel (f) shows clearly the tilting effect of the background wind field in which the low-level positive vorticity anomaly is tilted in the positive y-direction and the upper-level negative vorticity anomaly is tilted in the negative y-direction. The upper-level negative vorticity anomaly is relatively strong in magnitude at this time as the minimum vorticity lies in a region of strong divergence between the updraught and downdraught. The vorticity structure in the y-z through the low-level negative vorticity anomaly is the same as that in Figures 5.5(f), but with the sign of vorticity reversed (not shown). These findings would suggest that interpretations of the merger of convectively-induced cyclonic vorticity anomalies in terms of barotropic dynamics (e.g. Nguyen *et al.* 2008) may be over-simplistic. A recent analysis of convective structures in the principal rainband of Hurricane Rita (2005) by Didlake and Houze (2011; their Figure 8 and 9) shows slanting patterns of vertical vorticity with alternating sign. Didlake and Houze speculate that these patterns may be a result of vortex Rossby waves. However, the mechanisms described above might provide an alternative interpretation as the updraughts occur in regimes where the vertical shear presumably changes sign with height.

The low-level shear in Experiment 2 causes the initial thermal to spread out horizontally and weaken, leading to a spatially larger convective cell at low levels. However, at upper levels the updraught is weaker than in Experiment 1 and smaller in cross section. For this reason the generation of vorticity is weaker and the vorticity anomalies are smaller in horizontal cross section (see Figure 5.5 and Table 5.2).

In line with vertical velocity values, the vertical vorticity is much larger in Experiment 1, where $\zeta_{max} = 2.6 \times 10^{-2}$ s^{-1}, than in Experiment 2, where $\zeta_{max} = 1.2 \times 10^{-2}$ s^{-1}. In both experiments ζ_{max} occurs at a height of 6-6.5 km. These two experiments have no ambient vertical vorticity so that, initially, vertical vorticity is generated only by the tilting of horizontal vorticity into the vertical. However, once some vertical vorticity has been produced, it can be further amplified by stretching. In the absence of background vorticity, the positive and negative vortical structures that develop are symmetric and equal in strength, with neither member of the dipole strengthened more than the other, as confirmed by the identical magnitudes of ζ_{max} and ζ_{min} at heights of 1 and 4 km (Table 5.3).

In summary, the imposition of a boundary-layer wind profile has a dramatic effect on convection, markedly weakening convective updraughts and downdraughts, thereby reducing the amplification of vertical vorticity, and lowering the height to which updraughts penetrate. The weakening results largely from the deformation of the initial bubble by the low-level vertical shear.
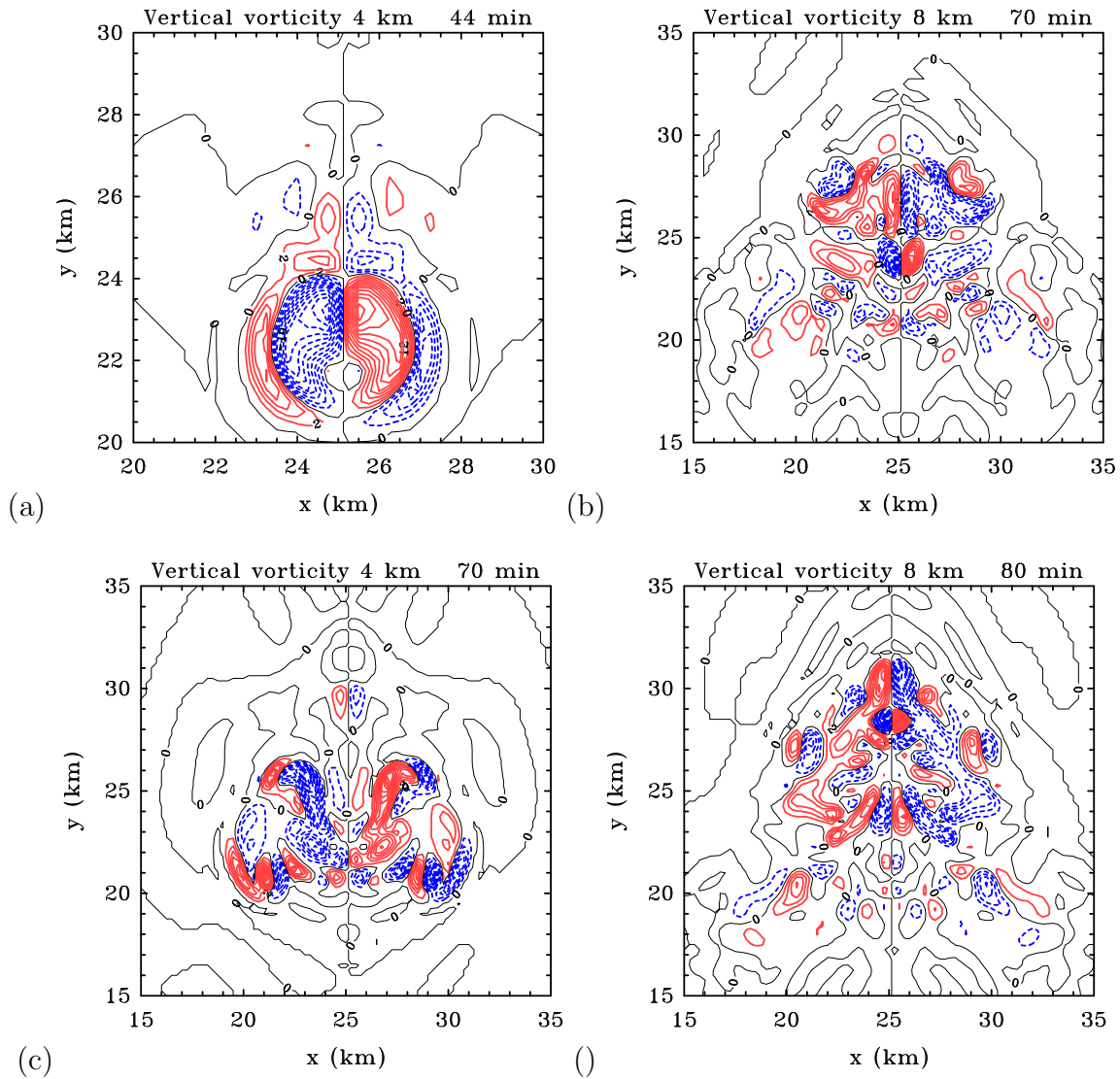
(a)

(b)

(c)

()

Figure 5.6: Horizontal cross section of the vertical vorticity at heights of 4 km and 8 km in Experiment 3 at chosen times. Contour interval: 2×10^{-3} s^{-1}. Solid (red) contours positive, dashed (blue) contours negative. The thin black curve shows the zero contour.

5.4   Storm splitting in a pure vertically-sheared environment

Experiments 3 and 4 are designed to investigate storm splitting in a warm-cored vortex environment, the former in pure vertical shear and the latter in pure horizontal shear. Because of its effect in distorting the initial thermal, vertical wind shear has a detrimental effect on convective initiation in these experiments for a given thermodynamic sounding. Indeed, in an early experiment with vertical shear and the relatively stable sounding of Experiments 1 and 2, convection does not occur (results not shown). For this reason, Experiment 3 uses the more unstable sounding, discussed in Section 5.2.4. Even ignoring the additional complexities of the strong radial wind component in the boundary layer of a tropical cyclone, the results of Section 5.3 show that a change in sign of the vertical shear implies a change in sign at some height of the vertical vorticity dipole produced by the updraught. As far as is known, the consequences of the change of sign of this dipole for the vorticity structure of successive updraughts in the case of a split storm has not been discussed previously in the literature. Experiment 3 is designed to examine this issue.

Since storm splitting is known to occur in mid-latitude storms in a regime of high vertical wind shear at low levels, Experiment 3 uses the same wind profile as Experiment 2, but with a smaller surface wind speed, and therefore a larger magnitude of vertical wind shear in the boundary layer. Figure 5.6 shows the pattern of vertical vorticity in horizontal cross sections at selected times at heights of 4 km (left panels) and 8 km (right panels) for this experiment. At a height of 4 km a split develops between 44 and 70 mins (panel (a) and (c) of Figure 5.6) with a patch of cyclonic vorticity moving from the domain centre to the right of the mean wind, and an anticyclonic patch moving to the left. At a height of 8 km, the sign of each vorticity patch is reversed with a large positive anomaly on the left of the ordinate and a large negative anomaly on the right. These vorticity patterns are similar to those of Experiment 2, although they are more complex because new convective cells are repeatedly initiated in the more unstable environment. This pattern of reversing vorticity with height in the split cells is different from the classical updraught structure of mid-latitude storms.

A notable feature of this simulation is that the domain maximum updraught and down-draught velocities occur late in the simulation, after 110 min (Table 5.2), and unlike the values in Experiments 1 and 2, are not representative of the initial cell. Thus the strongest vertical motion, and with it, the largest value of vertical vorticity, occurs *after storm splitting*. With the more unstable sounding and the larger low-level vertical shear compared with the configuration of Experiment 2, the maximum vertical vorticity (3.9×10^{-2}) is more than three times as large as in Experiment 2, but like Experiment 2, this maximum occurs in the upper troposphere (above 6 km).
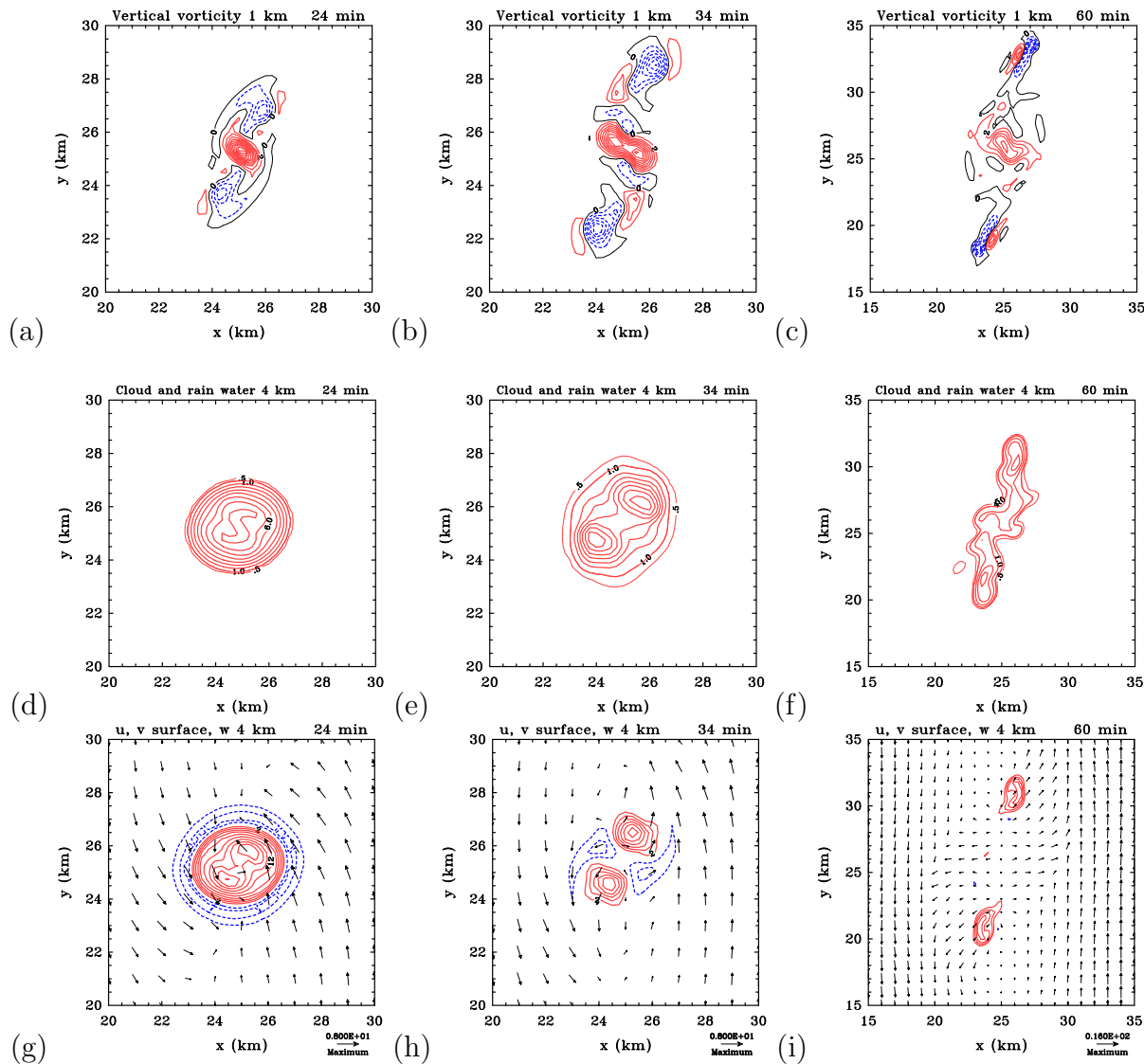
Figure 5.7: Horizontal cross section of: (top) the vertical vorticity at a height of 1 km, (middle) cloud and rain water at a height of 4 km, (bottom) vertical velocity at a height of 4 km overlying surface wind vectors for Experiment 4 at chosen times. Contour interval: vertical vorticity contours 2×10^{-3} s^{-1}, rain and cloud water contours: thin contour 0.5 g kg^{-1} and thick contours 1 g kg^{-1}, vertical velocity contours 2 m s^{-1}, surface wind vectors are relative to the maximum vector at the bottom right of plots (g), (h) and (i). The maximum wind vector is 15 m s^{-1}. Solid (red) contours positive, dashed (blue) contours negative. The thin black curve shows the zero contour.

5.5   Storm splitting in a pure horizontally-sheared environment

Experiment 4 is similar to Experiment 2 of Wissmeier and Smith (2011), but has a uniform, cyclonic, horizontal shear that is three times as large, sufficient to instigate storm splitting in this configuration. Horizontal cross sections of various quantities in this experiment are shown in Figure 5.7 at selected times. These include the vertical vorticity at a height of 1 km (upper panels), cloud and rain water at a height of 4 km (middle panels) and contours of vertical velocity at a height of 4 km superimposed on surface wind vectors (lower panels). By 24 min (left panels), the cloud and rain water contours, and the vertical velocity contours are still relatively axisymmetric, but the vertical vorticity fields show the effects of the background horizontal shear. By 34 min, a split is evident in the vertical velocity field and by 60 min the two updraughts are separated by approximately 10 km. At this time a large patch of positive vorticity remains where the original cell developed. There is a vorticity dipole structure also: this is associated with both the north and south moving cells. Interestingly the vertical vorticity minimum at heights of 1 and 4 km for Experiment 4 have values of -1.4×10^{-2} s^{-1} and -2.9×10^{-2} s^{-1}, respectively (both are stronger in magnitude than the vorticity maximum in Experiment 2). Thus, an appreciable *negative vorticity* anomaly is generated, even when the initial background vorticity is purely cyclonic. This negative vorticity is produced by the tilting of horizontal vorticity associated with the cold air outflow from the initial cell. The tilting is produced by the split updraughts that move over the cold pool and subsequently amplify the vertical vorticity by stretching. Because the background rotation is cyclonic, the cyclonic vorticity anomaly of the dipole is stronger in magnitude than the anticyclonic one.

The maximum updraught and downdraught strengths in Experiment 4 are 20.1 m s^{-1} and 6.8 m s^{-1}, respectively, and they occur *before the initial cell splits*. The domain-maximum vertical vorticity in Experiment 4 is 3.3×10^{-2} s^{-1} at a height of 7 km. The vorticity maxima at heights of 500 m and 1 km occur before splitting, while the maximum at a height of 4 km occurs after. This behaviour for pure horizontal shear is different from that of pure vertical shear, where the maxima of all these quantities occur after splitting.

As far as is known, the only previous study of storm splitting in horizontal shear is that of Rozoff (2007) and it is appropriate to compare the results of this section with his. Besides the different models used, there are two main differences between the experimental configuration in this study and in his. First, the largest value of horizontal shear used by Rozoff (2007) is -6×10^{-4} s^{-1}, while this study uses 9×10^{-4} s^{-1} in Experiment 4. Second, there are differences between the initial thermal bubbles. His bubble has a horizontal radius of 27.5 km, which is larger than the entire domain here. Moreover, his temperature perturbation of 2 K is built up gradually over the first 200 s, while in the case here it is imposed at the initial instant. In a regime of strong horizontal shear, the thermal perturbation becomes progressively elongated, and the gradual addition of incremental temperature perturbations over a time period of 200 s can be expected to increase the horizontal extent of the perturbation further.

To examine the consequences of the differences between the formulation of the thermal bubble, two more horizontal shear experiments were performed with different initial bubble configurations, both of which use the more stable standard sounding (results not shown). In the first experiment, the initial thermal bubble from this study was used as well as the more stable sounding, and it is found that cell splitting *does not occur*; rather convection evolves as described in Wissmeier and Smith (2011). This experiment was repeated with an initial thermal almost identical in size, position, and temperature excess when compared to that used by Rozoff. In this experiment, *splitting does occur with the more stable sounding*. It turns out that, as the spatial extent of the initial thermal is increased, the local buoyancy near the thermal centre (which is located at the domain centre) is reduced, so that convection does not occur as quickly as that initiated with a bubble of smaller horizontal scale. The delayed development allows the background horizontal shear to elongate the thermal before convective cells form at its longitudinal ends.

5.6 Combined horizontal and vertical shear

Experiments 5-8 are considered now, which are similar to Experiments 2, 3, 5 and 8 of Wissmeier and Smith (2011), respectively, but have a different thermodynamic sounding and include vertical shear also. Experiments 6 and 7 are carried out on an f-plane, the former with the Coriolis parameter $f = 0.5\zeta_o$ and the latter with $f = \zeta_o$ (Experiments 5 and 8 have no background rotation). Experiment 8 is a repeat of Experiment 5 with a representation of ice microphysics.

5.6.1 Vertical velocity

Figure 5.8 shows horizontal cross sections of vertical velocity for Experiment 5 at a height of 2 km at 28 min and 34 min after the initial time. The earlier time is that at which the updraught velocity is a maximum at this level and the later time is when the downdraught is a maximum. These cross sections are typical of those in the other experiments at similar stages of development. The annular region of downdraught surrounding the updraught core in Figure 5.8 (a) is part of the subsiding branch of the upward propagating thermal, and moves upwards with the thermal. This region is separate from the low-level downdraught, which is rain induced.

The updraught and downdraught strengths in Experiments 5-7 are broadly similar, and therefore insensitive to the background rotation rate, but there is not a monotonic increase in the magnitude of these two quantities with increasing background rotation rate (Table 5.2). This insensitivity is in contrast to the dependence on background rotation found in Wissmeier and Smith (2011) and is likely due to the smaller values of CIN in the present sounding. While CAPE values between the sounding in Wissmeier and Smith (2011) and the standard one used in this study are broadly similar (1800 J kg^{-1} compared with 2080 J kg^{-1}), the necessity of a 3.5 K thermal bubble to initiate convection in Wissmeier and Smith's study indicates that there is substantially more CIN present in their sounding.
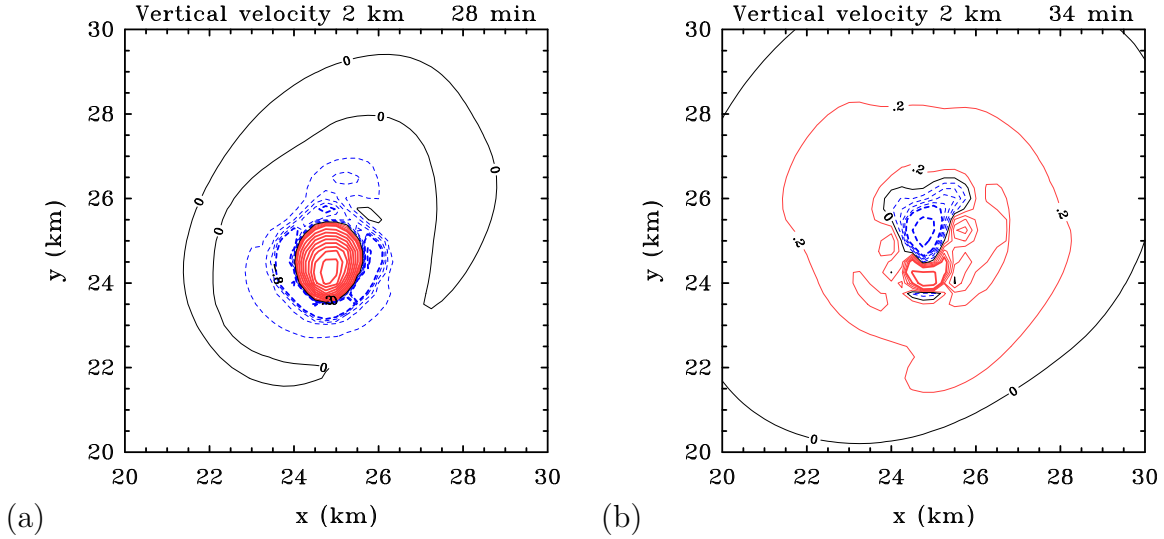
Figure 5.8: Horizontal cross section of the vertical velocity at a height of 2 km in Experiment 5 at: (a) 28 min, and (b) 34 min. The former time is when the updraught at this level is a maximum, the latter time when the downdraught is a maximum. Contour interval: thin contours 0.2 m s^{-1} to 0.8 m s^{-1}; thick contours 1 m s^{-1}. Solid (red) contours positive, dashed (blue) contours negative. The thin black curve shows the zero contour.

With ice processes included, the updraught[3] and downdraught are stronger in Experiment 8 than in Experiment 5, with $w_{max} = 26.1$ m s^{-1} compared with 23.8 m s^{-1} and w_{min} at an altitude of 2 km equal to -4.4 m s^{-1}, compared with -2.9 m s^{-1}. The stronger updraught in the experiment with ice processes is due to the additional buoyancy provided by the latent heat of freezing and the stronger downdraught is due to the cooling associated with melting of falling ice particles.

5.6.2   Relative vorticity

The top panels of Figure 5.9 show vertical cross sections of vertical velocity in the x-z and y-z planes and vertical vorticity in the x-z plane with rain water superimposed in Experiment 5 at 32 min. Panel (a) shows a relatively axisymmetric cell with the updraught maximum located near a height of 4 km. By this time a significant amount of rainwater has formed within it as seen by the co-location of the updraught maximum and the rain water maximum. The strongest downdraughts at this time occur in an annular region around the updraught core at a height of about 4 km. This downdraught is part of the subsiding

---

[3]Notice that w_{max} at an altitude of 2 km is 2 m s^{-1} larger when ice processes are included, although at this stage, no ice has formed! This feature was traced to the fact that the Gilmore ice scheme uses a different formulation of warm rain processes in Bryan's model than in the scheme for warm rain only. Since it is unclear which warm-rain scheme is most accurate, it has not been sought to implement one common scheme, but caution that this difference may overestimate the quantitative effects of including ice processes.

branch of the upward propagating thermal, as noted previously in reference to Figure 5.8. Figure 5.9b shows a slice through the middle of Figure 5.9a. In this plane, the effects of the vertical wind shear are evident in the tilt of the updraught with height towards the y-direction.

The vorticity profile in the x-z cross section (Figure 5.9c) is slightly asymmetric about the domain centre and has an inner dipole structure with cyclonic vorticity to the right and a weaker dipole structure outside of it with cyclonic vorticity to the left. To understand this structure, it is noted that the buoyancy of the rising thermal creates toroidal vorticity, which, together with ambient horizontal and vertical vorticity is tilted by the horizontal gradient of vertical velocity and stretched by the vertical gradient thereof. The tilting effect is not symmetric, as the toroidal vorticity, which is related largely to the horizontal gradient of vertical velocity, is not symmetric about the ordinate, having stronger values to the left in this case. This non-symmetric toroidal vorticity generation explains why the vertical vorticity *minimum* at a height of 4 km is larger in magnitude than the vertical vorticity maximum, when intuition might suggest that the latter quantity should be larger because of the presence of *cyclonic* background vorticity.

Panels (d) and (e) of Figure 5.9 show horizontal cross sections of vertical vorticity, vertical velocity and the horizontal wind structure at a height of 4 km in Experiment 5 at 30 min and 32 min. Panel (d) shows the moment that the updraught reaches a height of 4 km, with the horizontal winds diverging outwards. The non-symmetric vorticity features are evident as the positive vorticity anomaly is stronger in magnitude on the left of the updraught. By 32 min (panel (e)) there is a significant difference, as a vorticity dipole (generated by the updraught as it tilts the background vorticity) becomes the main vortical structure. An annular downdraught region is apparent and the horizontal wind field is now convergent towards the updraught centre.

Figure 5.10 shows horizontal cross sections of the vertical component of relative vorticity at a height of 500 m in Expts. 5-8 after 20 min, 44 min and 60 min of integration. Superimposed on these cross sections are the contours of vertical motion with magnitude greater than 1 m s^{-1}, where they exist. Prominent updraughts (vertical velocity > 1 m s^{-1}) at this level are delineated by a thick solid black contour and prominent downdraughts (vertical velocity < -1 m s^{-1}) are delineated by a thick black dashed contour. Unlike the corresponding patterns of vertical velocity, and unlike the vorticity fields in Wissmeier and Smith's experiments, the vorticity fields are far from axisymmetric, having mostly a prominent dipole or quadrupole structure. The dipole features at 20 min (upper panels of Figure 5.10) are clearly a result of the tilting of horizontal vorticity associated with the background shear into the vertical by the updraught of the first convective cell, which is located over the centre of the vorticity dipole. Note that tilting acting alone would produce positive and negative vorticity anomalies of about equal strength, whereas the additional effect here of the stretching of ambient cyclonic vertical vorticity leads to a stronger cyclonic gyre.

At later times (middle and lower panels of Figure 5.10), the vorticity fields have a quadrupole-like structure comprising a pair of dipoles. Animations of the fields show that the lower dipole constitutes the remnant vorticity that was formed by the first convective
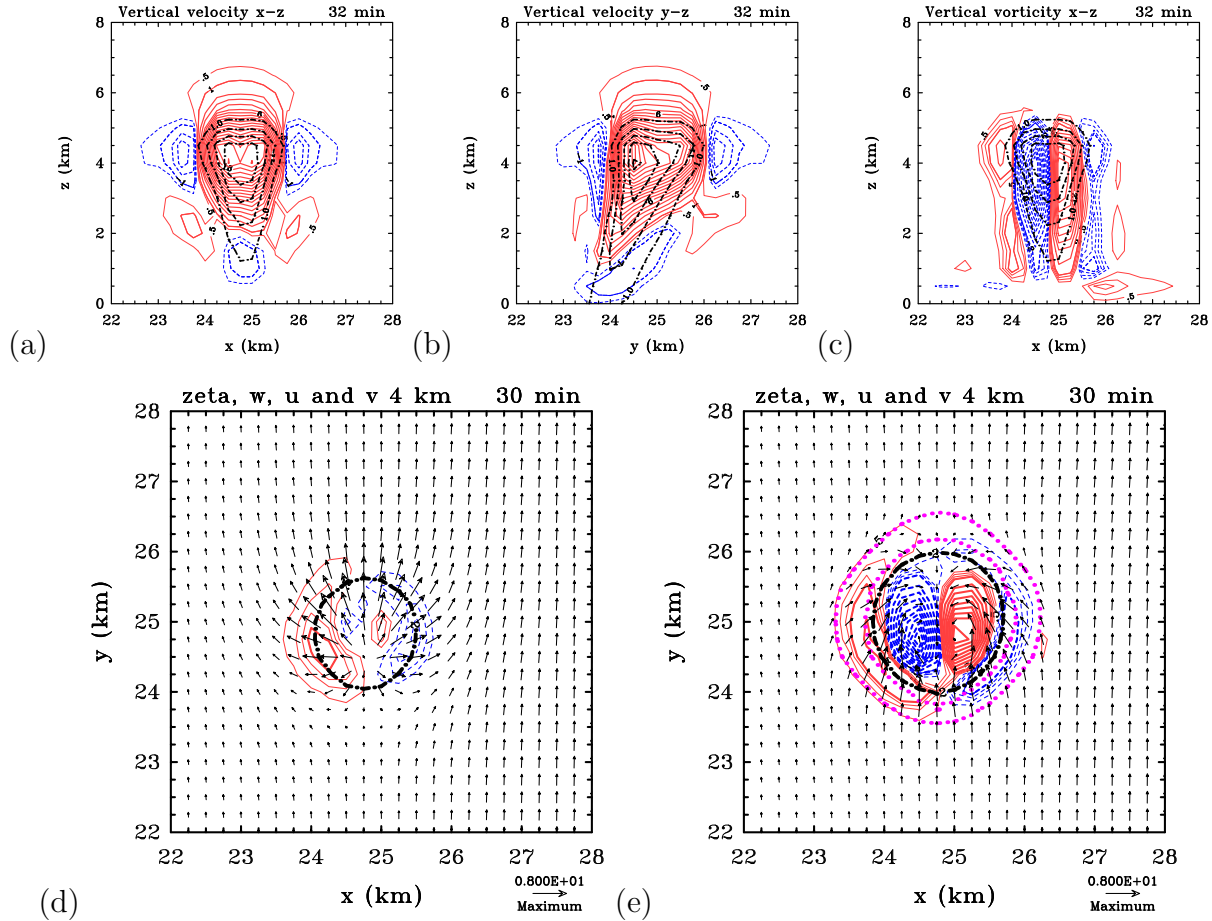
Figure 5.9: Panels (a) and (b) show vertical cross sections (x-z and y-z) of vertical velocity, with contours of cloud water mixing ratio, through the center of the domain at 32 mins for Experiment 5, where the cell is located at this time. Panel (c) shows a vertical cross section (x-z) of vertical vorticity, with contours of cloud water mixing ratio, through the center of the domain at 32 mins for Experiment 5. Contour interval: vertical velocity in: thin contour 0.5 m s^{-1}; thick contours 1 m s^{-1}, vertical vorticity thin contour 5×10^{-4} s^{-1} and thick contours 1×10^{-3} s^{-1}. Solid (red) contours positive, dashed (blue) contours negative. Rain water contours: 1 g kg^{-1} in dot-dashed (black) contours. The lower panels show horizontal cross sections of vertical vorticity, vertical velocity and horizontal winds at a height of 4 km at 30 and 32 mins for Experiment 5. Contour interval: vertical vorticity thin contours 5×10^{-4} s^{-1} to 1.5 $times 10^{-3}$ s^{-1}; thick contours 2×10^{-3} s^{-1}. Solid (red) contours positive, dashed (blue) contours negative. Vertical velocity: thick countour 2 m s^{-1}, dot-dashed (black) contours positive, dotted (pink) contours negative. Surface wind vectors are relative to the maximum vector at the bottom right of plots (d) and (e). The maximum wind vector is 10 m s^{-1}.

cell, while the upper dipole has formed by the tilting of background horizontal vorticity by the downdraught. Note that the downdraught occurs ahead of the tilted updraught in the y-direction (Figure 5.8b). At 44 min, the downdraught is colocated with the upper vertical vorticity dipole, while the updraught at the height of the cross section has all but decayed (in Expt. 5 it had already decayed at low levels by 32 min: see Figure 5.9 (a) and (b)). As the background rotation rate is increased in Expts. 5-7, the two positive vorticity anomalies are enhanced by the stretching of background cyclonic vorticity and they subsequently merge to form a single elongated anomaly (three left middle panels of Figure 5.10). At 60 min the two dipole pairs remain in all four experiments (lower panels of Figure 5.10).

In the simulations of Wissmeier and Smith (2011) and in Chapters 3 and 4, the maximum amplification of vertical vorticity occurs near the surface and is associated with stretching of vertical vorticity by the vertical gradient of the updraught mass flux. At early times the latter is large and positive near the surface because the buoyancy of the initial thermal is a maximum there. In Experiments 1-3 of Chapter 4, there was little or no amplification of vorticity above a height of 5 km. The results of Wissmeier and Smith (2011) show that, in a non-sheared environment containing ambient background rotation, the maximum amplification occurs close to the surface. In the current study, in the presence of vertical shear, tilting plays a large role in vorticity generation, and increases the depth to which significant vorticity anomalies occur.

Details of the vorticity maxima and minima at selected heights for Experiments 5-8 are included in Table 5.3. As the background rotation rate is increased from zero in Experiment 5 to ζ_0 in Experiment 7, ζ_{max} increases, while the magnitude of $\zeta 1_{min}$ and $\zeta 4_{min}$ decreases (Table 5.3). The low-level vorticity characterized, for example by $\zeta 1_{max}$, increases from 1.2×10^{-2} s^{-1} to 1.8×10^{-2} s^{-1}, whereas the magnitude of $\zeta 1_{min}$ decreases from 1.2×10^{-2} s^{-1} to 8.2×10^{-3} s^{-1}. The increase in $\zeta 0.5_{max}$ is even larger than $\zeta 1_{max}$ as the rotation rate is increased. Thus, at low-levels, where the stretching of background vorticity is largest, cyclonic vorticity anomalies are increased in magnitude, while anticyclonic anomalies are decreased. At a height of 4 km there is little change in the magnitude of the cyclonic vorticity anomalies as the background rotation increases, implying that the largest contribution to cyclonic vertical vorticity is by tilting at these levels. Interestingly, the maximum anticyclonic vorticity anomaly at a height of 4 km is largest when there is no background rotation and weakens slightly with increasing rotation. As explained above, this behaviour is due to the non-symmetric horizontal vorticity structure produced by the sheared thermal as it generates toroidal vorticity. The finding here that the negative vorticity anomaly is larger in magnitude than the positive anomaly may not be a general result, and may be related to the particular signs of the background horizontal and vertical shear in these experiments.

At least in the absence of background rotation, the inclusion of ice microphysics has little impact on the amplification of low-level vorticity. For example, $\zeta 0.5_{max}$ and $\zeta 1_{max}$ have values of 1.1×10^{-2} s^{-1} and 1.2×10^{-2} s^{-1} in Experiment 8, compared with 8.6×10^{-3} s^{-1} and 1.2×10^{-2} s^{-1}, respectively, in Experiment 5. This finding is consistent with the fact that the inclusion of ice microphysics leads to additional buoyancy only above the

freezing level (i.e. above a height of 5 km).

Figure 5.11 shows time-height cross sections of the maximum vertical vorticity in Experiments 5-8 and the minimum vertical vorticity in Experiments 5 and 8 (recall footnote 3 in Section 5.3). Features to notice are that there is a significant generation of vertical vorticity to heights of 5-8 km in the experiments with warm rain only (Experiments 5-7) and up to 10 km in the experiment with ice microphysics (Experiment 8). Another significant feature is that, as the background rotation rate increases, there is a marked increase in the magnitude of low-level vertical vorticity, as discussed previously (Figure 5.11a-c). There is an increase also in the magnitude of vertical vorticity located near a height of 4 km, as the background rotation rate increases. In contrast, the vorticity anomaly located at a height of 6 km weakens earlier as the background rotation rate increases. A small patch of vorticity located above a height of 8 km in Figure 5.11b and 5.11c is due to the stretching of background vertical vorticity by gravity waves generated by the updraught.

While the inclusion of ice processes has little effect on the generation of vorticity at low levels, there is a significant effect on middle tropospheric vorticity enhancement (compare Figure 5.11a and 5.11d). The vorticity maxima are mostly comparable between Experiments 5 and 8, but the region of enhanced vorticity in Experiment 8 extends through a larger depth and persists longer than in the warm rain experiment. Again, this finding is consistent with the fact that the inclusion of ice microphysics leads to additional buoyancy only above the freezing level.

In summary, at early times the convection produced in Experiments 5-8 has a prominent vorticity dipole structure associated with the tilting of ambient horizontal vorticity by the updraught. At later times a second vorticity dipole forms ahead of the slanted updraught through the tilting of ambient vorticity by the convective downdraught. The strength of the cyclonic vertical vorticity anomalies increases at low levels as the background rotation rate increases, presumably because of the increased stretching of ambient cyclonic vertical vorticity. In fact the vorticity maximum in the experiment with the largest background rotation rate is located at the surface. At mid levels there is little change in the magnitude of the vorticity maxima as the background rotation increases, implying that the largest contribution to vertical vorticity is by tilting at these levels. In the presence of background vertical shear, tilting plays an important role in vertical vorticity generation and increases the depth to which significant vorticity anomalies occur. In contrast, in similar calculations without vertical shear, there is no appreciable amplification of vorticity above a height of 5 km.

The inclusion of ice microphysics increases the updraught and downdraught strength as expected, and provides a much deeper area of enhanced vorticity that persists longer than in the warm rain experiment.
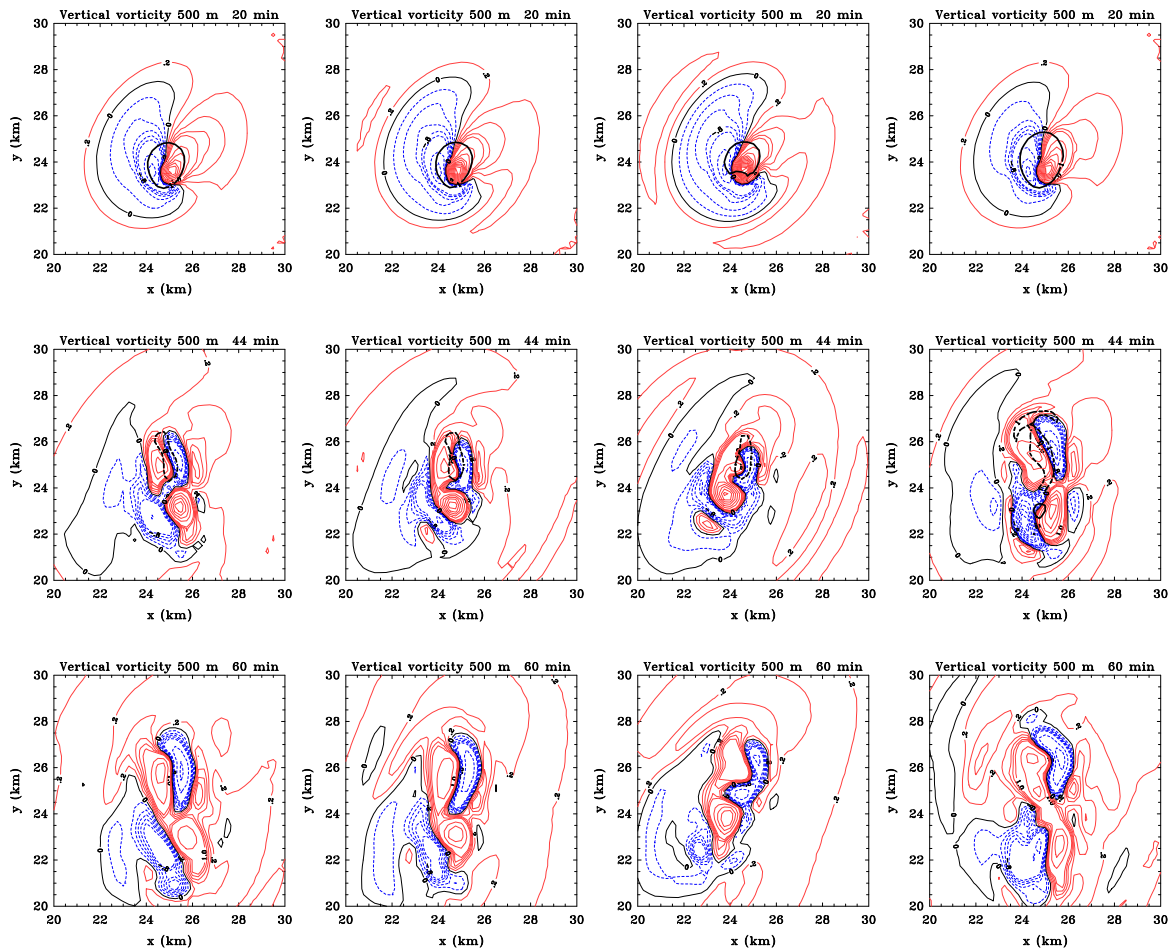
Figure 5.10: Horizontal cross section of the vertical component of relative vorticity at 20 min (upper panels), 44 min (middle panels) and 60 min (lower panels) at a height of 500 m in the four experiments: from left to right Expt. 5, Expt. 6, Expt. 7 and Expt. 8. Contour interval: thin contours 2×10^{-4} s^{-1} to 8×10^{-4} s^{-1}; thick contours 1×10^{-3} s^{-1}. Solid (red) contours positive, dashed (blue) contours negative. The thin black curve shows the zero contour. The thick black contours show the 1 m s^{-1} (solid) and -1 m s^{-1} (dashed) contour of vertical velocity.
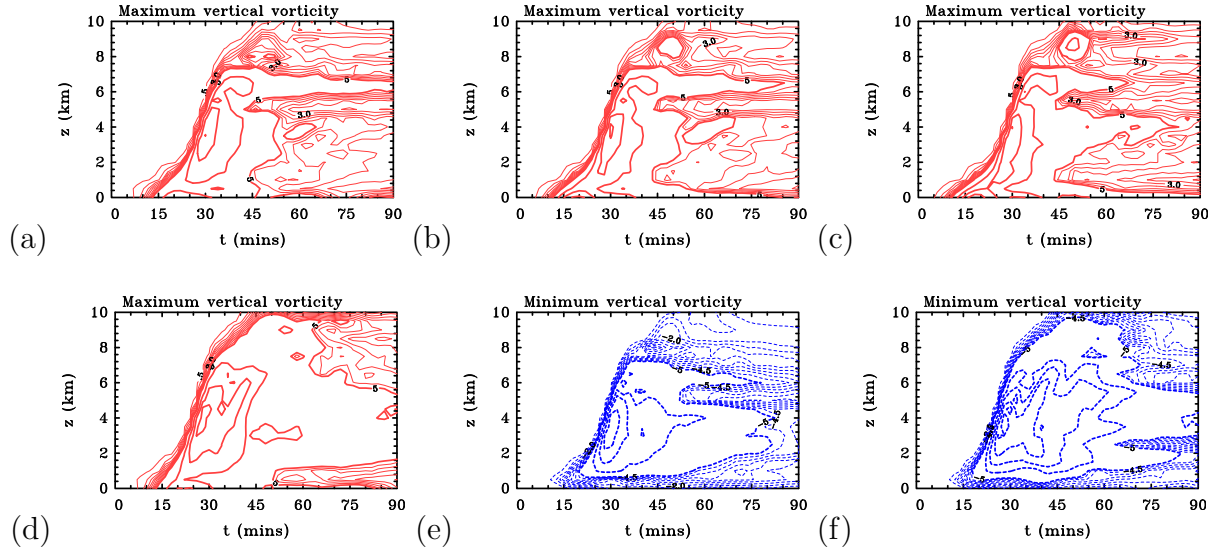
Figure 5.11: Time-height series of maximum vertical vorticity in four Experiments: (a) Experiment 5, (b) Experiment 6, (c) Experiment 7, (d) Experiment 8, and the minimum vertical vorticity in: (e) Experiment 5, (f) Experiment 8. Contour interval: thin contours 0.5×10^{-3} s^{-1} to 4.5×10^{-3} s^{-1}; thick contours 5×10^{-3} s^{-1}. Solid (red) contours positive, dashed (blue) contours negative. The thin black curve shows the zero contour.

5.7 Updraught splitting in combined horizontal and vertical shear

Updraught splitting is now examined in a background flow with both horizontal and vertical shear in a configuration similar to that in the previous section, but without background rotation. The next two experiments are guided by the results of Sections 5.4 and 5.5, which showed that splitting is favoured by relatively unstable soundings and relatively large low-level vertical shear. In these experiments the amount of low-level shear is increased compared to that in the standard wind profile (shown in Figure 5.2) and the unstable sounding is used. First an experiment with no horizontal shear (Experiment 9) is performed. This experiment differs from Experiments 2 and 3 in that the background wind becomes effectively constant with height above about 2 km, a necessary simplification in order to interpret the results more easily. Experiment 10 is a repeat of Experiment 9 with horizontal shear included. In both experiments the increased low-level vertical shear is achieved by trebling the value of b in Equation 3.

Table 5.2 shows the maximum updraught and downdraught strengths at various heights for these experiments. The larger maximum vertical velocity occurs in the experiment with horizontal shear (21.6 m s^{-1} compared to 18.7 m s^{-1}). The domain maximum updraught velocities listed in Table 5.2 for Experiment 10 occur late in the simulation (after 100 min), while some of the values for Experiment 9 occur much sooner (after 50 min), indicating that the most vigorous convection occurs later in the presence of horizontal shear. While

the maximum downdraught velocities are largely comparable in the two experiments, it is interesting to note that both these experiments contain the strongest downdraughts at a height of 2 km found in this study. These strong downdraughts account for the ease with which new cells develop along the gust front and, therefore, for the complexity of the vorticity structure at later times.

Experiments 9 and 10 have maximum vertical vorticities of 3.5×10^{-2} s^{-1} and 3.8×10^{-2} s^{-1}, respectively (Table 5.3). The maximum found in Experiment 9 occurs at a height of 1.5 km, which is in contrast to the finding of the previous uni-directional vertical shear experiments (recall that in Experiments 2 and 3, the vertical vorticity maxima are found at heights of 6 and 8 km, respectively). The vorticity maximum at low levels in Experiment 9 is a result of using the standard wind profile, which has no vertical shear above a height of 2 km, so that there is little contribution to vorticity production by tilting much above this height.

Figure 5.12 shows horizontal cross sections of the vertical component of relative vorticity at a height of 4 km for Experiments 9 and 10 at selected times. Shown also is the 2 m s^{-1} contour of vertical velocity, which is used to determine whether updraught splitting has occurred. In the presence of vertical shear only (panels (a)-(d)), the vorticity features remain symmetric about the ordinate throughout the simulation. At 30 min and 44 min, the pattern is dominated by an inner dipole associated with the tilting of horizontal vorticity by the updraught of the rising thermal and by an outer dipole, opposite in sign, on the flanks of the updraught, which is associated with the tilting of vorticity by the downward motion there. A split in the updraught has begun to appear as early as 44 min at this level. At 70 mins a complete split has occurred, with a distance of nearly 5 km separating the two most prominent updraughts. At 80 min, the vorticity pattern is more complex, reflecting the development of additional convective cells.

When horizontal shear is included, the vorticity pattern is again approximately symmetric about the ordinate at 30 min (Figure 5.13a), although a slight distortion by the horizontal shear is evident. However, even at 44 min, the symmetry has become lost and, as in Experiment 9, the updraught has started to split at this level. By this time, an intense cyclonic vorticity anomaly has developed in the upper half of the domain (panel (b)). Vertical cross sections in the x and y-directions through the vorticity maximum in Figure 5.13b (not shown) indicate that this feature is associated with an updraught-downdraught couplet which breaks off from the main updraught cell, generating cyclonic vertical vorticity between the updraught and downdraught, presumably by stretching. This updraught-downdraught couplet rapidly decays, but the vorticity signature decays less rapidly. This process is repeated several times before the end of the calculation. The vertical vorticity on the flanks of the main dipole, associated with the subsiding part of the thermal, has a stronger cyclonic anomaly and a weaker anticyclonic one than in Experiment 9 (panels (b) of Figure 5.12 and (b) of Figure 5.13).

The subsequent evolution of the vorticity field is different from that in Experiment 9, even before splitting occurs at around 70 min. At this time the updraught that is co-located with the anticyclonic vorticity anomaly is noticeably filamented, and has wrapped around the cyclonic vorticity patch associated with the overturning thermal (see panel (c) of Figure

Figure 5.12: Horizontal cross section of the vertical component of relative vorticity for Experiment 9 at four different times: 30 mins, 44 mins, 70 mins and 80 mins. Contour interval: thick contours 2×10^{-3} s^{-1}. Solid (red) contours positive, dashed (blue) contours negative. The thick black curve shows the 2 m s^{-1} contour of vertical velocity . Note that it is necessary to use a larger domain in plots showing 70 and 80 mins to show all the necessary convective features.
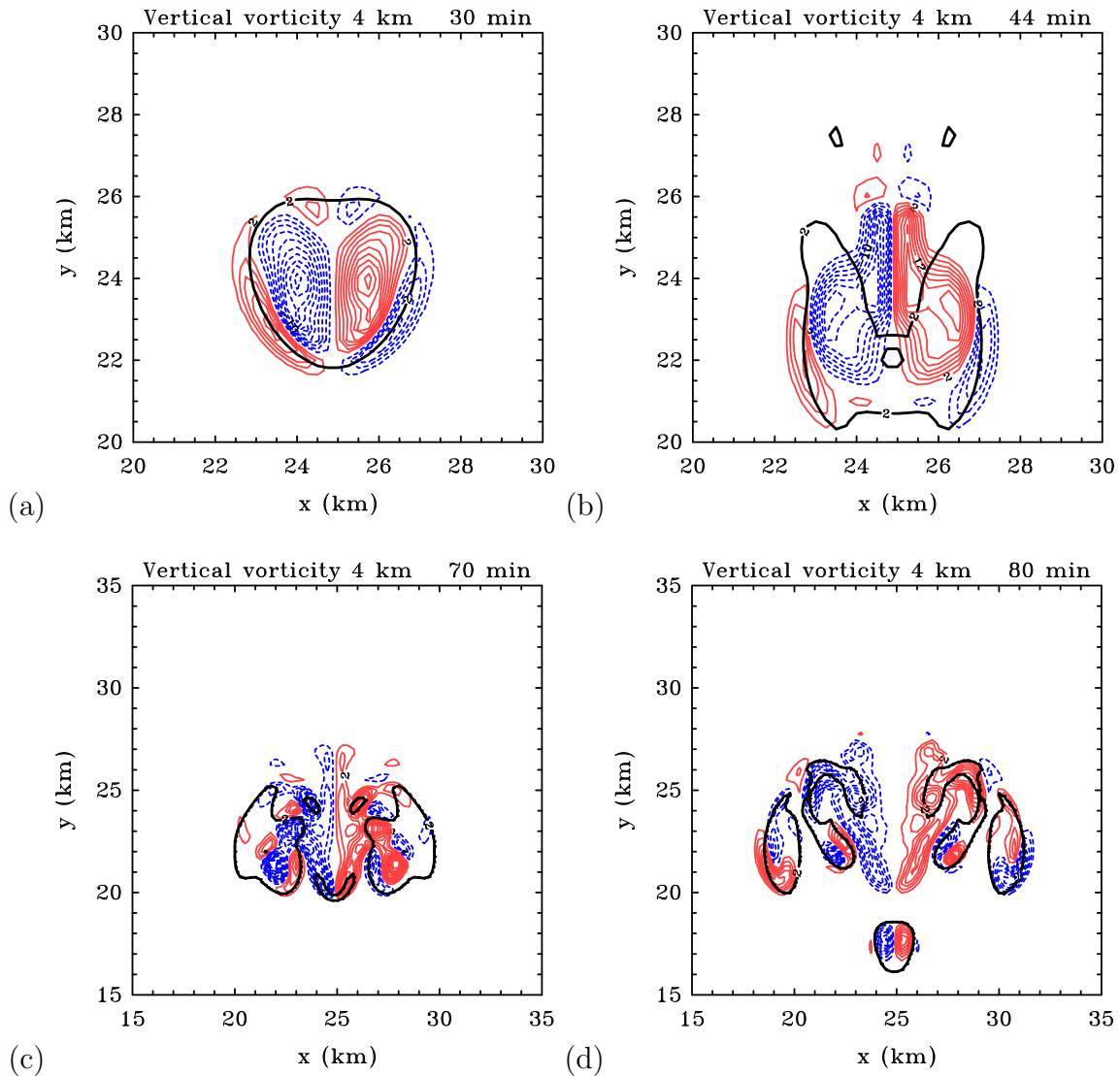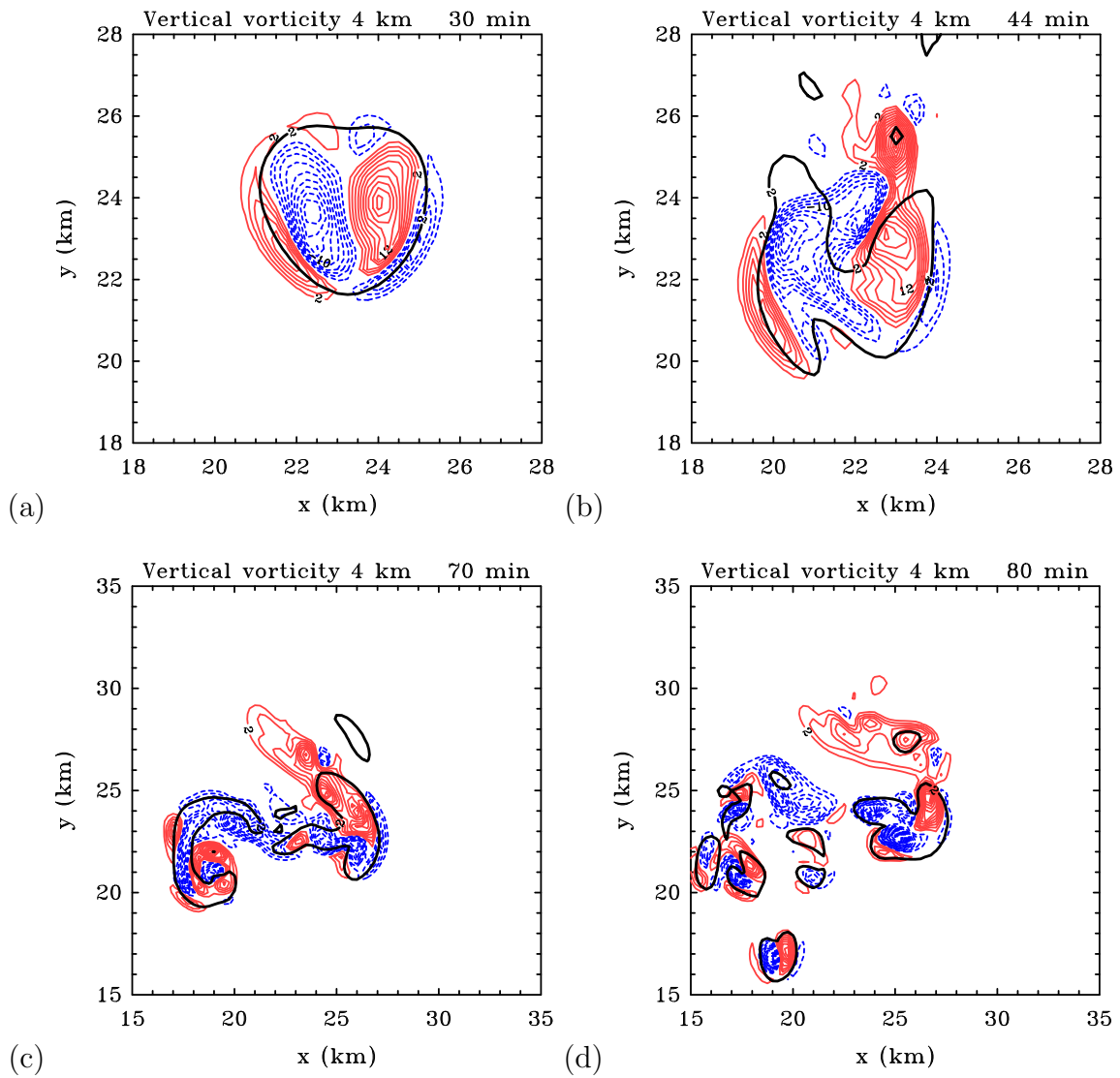
Figure 5.13: Horizontal cross section of the vertical component of relative vorticity for Experiment 10 at four different times: 30 mins, 44 mins, 70 mins and 80 mins. Contour interval: Same as Figure 5.12.

5.13). The vorticity features are predominantly cyclonic on the right side of the domain, and predominantly anticyclonic on the left side. By 80 min, there is a large coherent patch of cyclonic vorticity with little updraught signature in the upper part of the domain. This feature is a manifestation of the successive vorticity generated by the "cut-off" updraught-downdraught couplets as described above. The updraught centre located to the right of the domain has evolved from the updraught on the right of the first split cell and contains anticyclonic vorticity associated with tilting of background horizontal vorticity. In both experiments, new convective cells have formed along the spreading gust front and have generated new vorticity dipoles on both the right and left sides of the domain.

5.8   Conclusions

Herein are described a series of numerical experiments designed to isolate the effects of ambient wind shear, both horizontal and vertical, on the generation of vertical vorticity by deep convection in tropical disturbances.

The first aim of this chapter was to examine the role of a deep layer of negative vertical shear overlying a shallow layer of positive vertical shear on storm morphology. This pattern of shear arises in the tangential wind direction in tropical cyclones, although the complete boundary-layer flow in a tropical cyclone is not unidirectional.
The first set of experiments examined the effect of a uni-directional boundary-layer-type wind profile on vorticity generation. It was found that the implementation of such a profile has a dramatic effect on convection, markedly weakening convective updraughts and downdraughts, thereby reducing the amplification of vertical vorticity and lowering the height to which updraughts penetrate. In the boundary-layer-type wind simulation, the weakening results largely from the deformation of the initial bubble by the low-level vertical shear. This bubble rises first through a layer of positive vertical shear and subsequently through one of negative vertical shear, so that the sign of the background horizontal vorticity it experiences reverses. Thus, two oppositely-signed vorticity dipoles emerge within the updraught, one in the layer of positive vertical wind shear, and the other, in the layer of negative vertical wind shear. This finding would suggest that interpretations of the merger of convectively-induced cyclonic vorticity anomalies in terms of barotropic dynamics may be oversimplistic.

A second aim of this chapter was to extend the study of Wissmeier and Smith (2011) by investigating and quantifying the combined effects of both horizontal and vertical wind shear on deep convection that develops in a thermodynamic environment typical of a tropical depression.
Three experiments were carried out to examine the effects of adding background rotation to the standard boundary-layer-type wind shear profile. It was found that the convection produced has a prominent vorticity dipole associated with the tilting of horizontal

vorticity. A second oppositely-signed dipole is produced at later times, generated by the tilting of ambient horizontal vorticity by the convective *downdraught*. As the background rotation rate increases, so does the strength of the positive low-level vertical vorticity anomalies. However, there is little effect on the strength of those in the middle troposphere, indicating that the largest contribution to vertical vorticity production at these levels is by tilting. The inclusion of ice microphysics increases the updraught and downdraught strengths and leads also to a much deeper layer of amplified vorticity than in the warm rain experiment, and one that persists for longer.

A third aim of this chapter was to re-examine the mechanisms involved in storm splitting discussed by Rozoff (2007), again giving particular attention to vertical vorticity generation. Since there is observational evidence for the existence of supercell convection in tropical storms (e.g. Gentry *et al.* 1970, Black 1983), it may be presumed that storm splitting is a relevant process in these systems also.
Two experiments were carried out to examine the effect that storm splitting has on vorticity generation, one in a purely vertically-sheared environment, and one in a purely horizontally-sheared environment. In the experiment with pure vertical shear, the maximum vertical velocity and vorticity occur after storm splitting. However, in the experiment with pure horizontal shear, the maximum values of vertical velocity and low-level vertical vorticity occur before splitting. In the latter experiment, a large patch of anticyclonic vertical vorticity is generated despite there being no background source of horizontal vorticity or negative vertical vorticity. This feature may be attributed to the spreading cold pool, which generates horizontal vorticity. This horizontal vorticity is subsequently tilted into the vertical by the split updraughts. Finally two more experiments were carried out to examine vorticity generation in the case of storm splitting in a combined horizontal and low-level vertical shear environment. In the presence of vertical shear only, the vorticity features remain symmetric about the direction of shear throughout the simulation, whereas horizontal shear destroys this symmetry and the evolution of the vorticity field becomes more complex with new flanking cells continuously flaring up.

Chapter 6

Effects of a vortex boundary-layer wind profile on deep convection

6.1   Introduction

An additional complication in the context of tropical cyclones is that there is a significant radial wind component in the boundary layer and this component may increase or decrease with height at low levels, depending on the radius (see e.g. Smith and Montgomery 2013). Thus, experiments with uni-directional vertical wind profiles examined may be over simplistic in application to such vortices. For this reason, a further series of numerical experiments are carried out to examine the additional effects of a typical radial wind profile in a tropical-cyclone on the evolution of deep convection, focussing on vertical vorticity production.

A key question to be addressed in this chapter is how does a typical vortex boundary-layer-type wind profile structure affect the generation of vertical vorticity and its vertical structure? The results provide an essential first step to understanding the interaction between deep convective elements in a tropical depression or tropical cyclone. Cases are considered in which there is either no vertical shear above the boundary layer, or negative vertical shear appropriate to a warm-cored vortex.

A second aim of this chapter is to quantify the effects of an increase in the magnitude of boundary-layer shear on vertical vorticity production.

A third aim is to examine the production of vertical vorticity in a more realistic tropical depression environment. Tropical depressions and tropical cyclones have not only elevated levels of background vertical vorticity, but because of the larger wind speeds, they represent convective environments with elevated levels of low-level horizontal vorticity as well.

The calculations provide a basis for appraising a recently proposed conceptual model for the inward contraction of eyewall convection in tropical cyclones.

The chapter is organized as follows. In section 6.2 a brief overview of the numerical model and the configuration of the experiments is given. The results are presented in sections 6.3-6.7 and an appraisal of the Hogsett and Stewart conjecture is given in section 6.8. The conclusions are given in section 6.9.

6.2   Experimental setup

6.2.1   Model configuration

The experiments use the same model configurations as those of Chapter 5. The horizontal domain size is 50 km × 50 km with a uniform horizontal grid spacing of 250 m. The vertical domain extends to a height of 28 km with the vertical grid interval stretching smoothly from 120 m at the surface to 1000 m at the top. There are 50 grid levels in the vertical, 8 of which are below 850 mb. The large time step is 3.7 seconds and the integration time is 2 h. There are 8 small time steps per large time step to resolve fast-moving sound waves. The default "open" boundary conditions are used at the lateral boundaries. A sponge-layer is implemented in the uppermost 2 km to inhibit the reflection of gravity waves from the upper boundary. All experiments include warm rain physics.

6.2.2   The numerical experiments

Seven numerical experiments are described, details of which are summarized and compared in Table 6.1. Further details about the experiments and their purpose are given in the appropriate sections.

6.2.3   Background wind profiles

The ambient vertical wind profiles $(U(z), V(z))$ used in the experiments are shown in Figure 6.1. These are expressed in a rectangular coordinate system (x, y, z), where z is the height. The profiles are obtained from the linear vortex boundary-layer solution of Vogl and Smith (2009), in which $U(z)$ and $V(z)$ are the radial and tangential wind components. and they have the form:

$$U(z) = -V_a \exp(-Z_a) \left[A_1 \sin Z_a + A_2 \cos Z_a\right] \tag{6.1}$$

$$V(z) = V_a \left(1 - \exp(-Z_a)\right) \left[B_1 \cos Z_a - B_2 \sin Z_a\right] \tag{6.2}$$

where A_1, A_2, B_1, B_2 are constants, $Z_a = z/Z_g$ is a nondimensional height, Z_g is the boundary-layer depth scale, and V_a is the (tangential) wind speed at the top of the boundary layer.

Exp	f	BL profile	above BL	V_a
1	0	standard	no shear	$10\ \mathrm{m\ s^{-1}}$
2	0	standard	neg shear	$10\ \mathrm{m\ s^{-1}}$
3	0	standard	no shear	$5\ \mathrm{m\ s^{-1}}$
4	0	standard	no shear	$15\ \mathrm{m\ s^{-1}}$
5	ζ_o	standard	no shear	$10\ \mathrm{m\ s^{-1}}$
6	ζ_o	gale force	no shear	$17\ \mathrm{m\ s^{-1}}$
7	ζ_o	gale force	neg shear	$17\ \mathrm{m\ s^{-1}}$

Table 6.1: Details of the seven experiments studied herein. ζ_0 has the value $3 \times 10^{-4}\ \mathrm{s^{-1}}$. All experiments are initiated with a 3 K thermal perturbation. V_a is the (tangential) wind speed at the top of the boundary layer. The wind profiles are discussed further in section 6.2.3.

The profile for Experiments 1-5 has parameters: $A_1 = 0.356$, $A_2 = 0.192$, $B_1 = A_1$, $B_2 = A_2$, $Z_g = 632$ m, and V_a as given in Table 6.1. These values are appropriate for a classic turbulent Ekman-layer profile. In Experiment 2, a wind profile with unidirectional, negative vertical shear is blended with the above profile above a height of 2 km so that $V(z)$ decreases with height. The equation for $V(z)$ above 2 km is given in Chapter 5 and was used in its Experiments 1-3. The low-level wind profile for Experiments 6 and 7 is characteristic of the region of gales in a tropical cyclone and has parameters: $A_1 = -0.415$, $A_2 = 0.202$, $B_1 = -0.304$, $B_2 = -0.625$, $Z_g = 472$ m, and $V_a = 17$ m s^{-1}. In Experiment 6, there is a uniform flow with gale-force strength (17 m s^{-1}) above 2 km, while Experiment 7 has a profile with negative shear profile, similar to Experiment 2. The profiles are shown in Figure 6.1, labeled "ET" for Experiments 1 and 3-5, "E2" for Experiment 2, and "E6" for Experiment 6.

Figure 6.2 shows the nondimensional wind hodograph for the ambient vertical wind profiles described above. The magnitude and orientation of the horizontal vorticity is indicated by arrowed lines normal to the wind curves at the surface and at heights of 200 m, 500 m and 1 km. The magnitude of horizontal vorticity is larger in the wind profile used in Experiments 6 and 7 at the surface and heights of 200 m and 500 m than in the profile used in Experiments 1-5. At a height of 1 km both profiles have roughly the same magnitude of horizontal vorticity, while there is practically no horizontal vorticity at and above a height of 2 km, except in the profile used in Experiments 2 and 7, which have unidirectional vertical shear above a height of 2 km.

While highly idealized, these profiles have the qualitative structure of a vortex boundary layer. The profiles are quiet realistic when compared to the atmosphere as they include the effects of frictional surface drag law on the wind field. The surface wind components are nonzero, the total surface wind being about 0.6 times that at large heights in the profiles used for Experiments 1-5. In the wind profiles without negative wind shear at mid-upper levels the V-component has a constant wind speed of V_a, while the U-component decays to zero in all experiments above a height of 2 km.
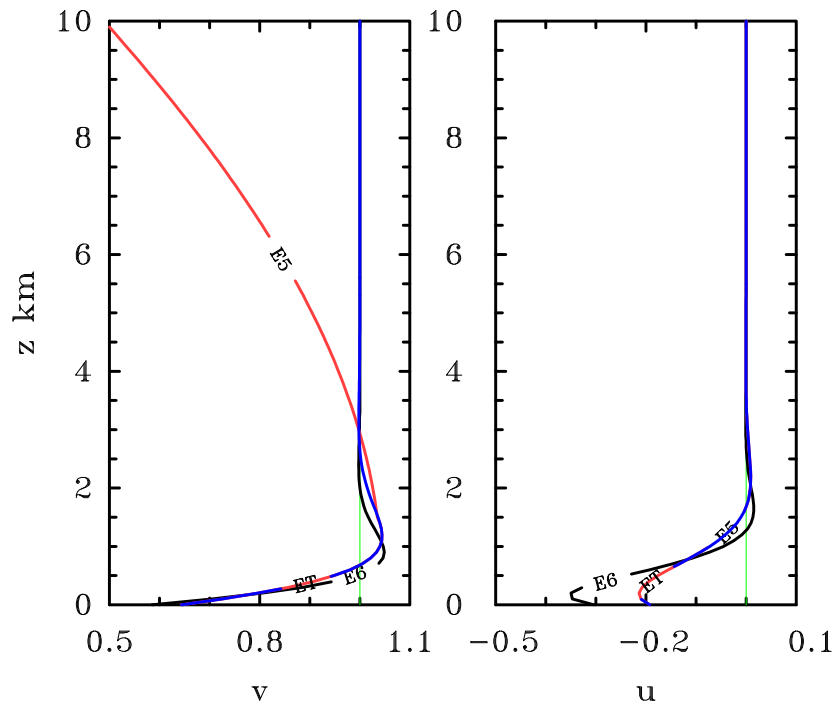
Figure 6.1: The background wind flow used for all experiments. The left profile denotes the nondimensional V component and the right profile denotes the nondimensional U component for the wind profiles in Experiments 1 and 3-5 (blue contour labeled ET), Experiment 2 (light blue contour labeled E2) and for Experiment 6 (red contour labeled E6). Experiment 7 combines the boundary-layer profile used in Experiment 6 and the upper level negative shear profile used in Experiment 2. These profiles are multiplied by the reference wind value given in Table 6.1 for each experiment.

A uniform flow is added to the wind profile in all experiments in order to keep the convection near the centre of the computational domain. The value of this flow is determined by trial and error and is different for each experiment.

6.2.4   Representation of vertical vorticity

The calculation in Experiments 5-7 are carried out on an f-plane with the Coriolis parameter $f = \zeta_o$, where $\zeta_o = 3 \times 10^{-4}$ s^{-1}, a value typical of that in a tropical depression[1]. The use of an f-plane with an enhanced value of f beyond a typical tropical value is a simple expedient to model the background rotation of the vortex in the present problem.

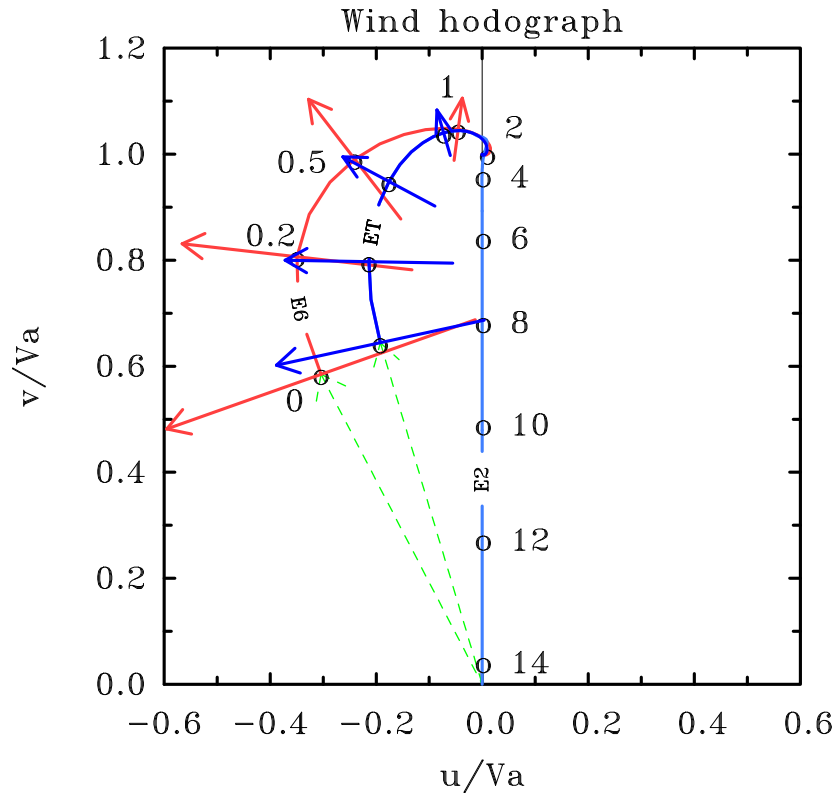[1]See Foster and Lyons 1984, Wissmeier and Smith 2011, section 2.3.

Figure 6.2: The background wind hodograph for the nondimensional wind profiles in Experiments 1 and 3-5 (blue contour labeled ET) and for Experiment 6 (red contour labeled E6). The light blue (labeled E2) line represents the uni-directional vertical wind shear for heights above 2 km in Experiment 2. This experiment has the same wind profile as Experiments 1 and 3-5 below a height of 2 km. Experiment 7 combines the boundary layer profile used in Experiment 6 and the upper-level negative shear profile used in Experiment 2. The circular marks and accompanying numbers represent heights. The arrows normal to the curves labeled ET and E6 show the direction and relative magnitude of the horizontal vorticity at those heights. The thin dashed (green) lines represent the wind vectors at the surface.

6.2.5   Thermodynamic sounding

All experiments use the standard idealized thermodynamic sounding used in Chapter 5.

6.2.6   Initiation of convection

Convection is initiated by a symmetric thermal perturbation with a horizontal radius of 5 km and a vertical extent of 1 km as previous chapters. The temperature excess has a maximum at the surface at the centre of the perturbation and decreases monotonically to zero at the perturbation's edge. The perturbation centre coincides with the centre of the

domain. In general, the details of the ensuing convection such as the maximum updraught strength and the updraught depth will depend on the spatial structure and amplitude of the thermal perturbation. A maximum temperature perturbation of 3 K is used in all experiments, which is 1 K larger than that used in Chapter 5. The larger thermal perturbation used here is due to the fact that the low-level vertical wind shear in these experiments completely suppresses convection with a bubble of only 2 K.

While this method for the initiation of convection is necessarily artificial, it is unclear how to significantly improve upon it and for this reason it has been widely used in numerical studies of deep convection (see e.g. Weisman and Klemp 1982, Gilmore *et al.* 2004, Rozoff 2007, Wissmeier 2009[2] and Wissmeier and Smith 2011.) In reality, thermal perturbations over the ocean will be linked to surface heat fluxes, but there are other ways in which convection may be triggered such as lifting at gust front boundaries generated by prior convection. It is planned to examine the effects of such processes on vertical vorticity generation in a subsequent study. One possibly more realistic method to initiate convection is to begin with a low-level cold pool that induces sufficient lifting at its boundary to bring environmental air to its level of free convection. In fact two experiments were explored to examine this possibility. These had the same configuration as Experiments 5 and 8 in Chapter 5, but convection was initiated with a cold pool and the more unstable sounding from that chapter was used. In both experiments convection developed into a squall line structure, while the squall line in the experiment with ice-microphysics had a larger horizontal extent with greater magnitudes of vertical motion. The results were hard to interpret as new cells continuously flared up and interacted with each other, making it difficult to isolate the effects of the background flow on any individual cell. For this reason, these calculations have not been included in this thesis. One interesting result from those experiments is that the vertical vorticity maxima were comparable to the largest values found in that chapter. This result indicates that the large vertical vorticity values found in experiments initiated with an initial thermal perturbation may not be so unrealistic, when comparable values are found in experiments where convection is initiated with a cold pool.

6.2.7   The experiments in brief

Experiment 1 is designed to isolate the effects of boundary-layer shear and serves as a control experiment. It has a background reference wind of 10 m s^{-1} and no background rotation (Table 6.1). A detailed analysis of this experiment is carried out in the next section. Experiment 2 is similar to Experiment 1, but has a unidirectional vertical wind profile with negative vertical shear above 2 km, making it more realistic vis-à-vis a tropical warm-cored vortex. Experiments 3 and 4 are similar to Experiment 1, but have wind speeds above 2 km that are half or 1.5 times that in Experiment 1, respectively, giving smaller or larger low-level wind shear. These experiments are designed to examine the dependence

---

[2]Section 3.4.2 therein examines the sensitivity of the storm's initial updraught strength on the warm bubble parameters (width, depth, temperature excess).

Expt.	w_{max}	w_{min}	$w2_{max}$ m s^{-1}	$t(w2_{max})$ min	$w5_{max}$ m s^{-1}	$t(w5_{max})$ min	$w9_{max}$ m s^{-1}	$t(w9_{max})$ min	$w2_{min}$ m s^{-1}	$t(w2_{min})$ min
1	25.8	-10.5	9.6	24	25.8	28	4.9	40	-5.9	40
2	25.7	-10.7	9.7	24	25.7	28	6.6	42	-7.1	40
3	28.4	-11.7	10.4	22	24.3	26	8.9	34	-5.3	22
4	25.9	-9.7	8.2	28	25.9	32	5.5	50	-4.4	34
5	25.2	-11.2	9.8	24	24.0	28	6.4	46	-4.8	38
6	18.5	-4.5	5.9	32	18.5	40	6.3	54	-2.2	52
7	19.1	-4.2	6.0	34	19.1	40	6.4	54	-1.9	32

Table 6.2: Maximum vertical velocity, wN_{max}, and minimum vertical velocity, wN_{min}, at a height of N km and the times at which they occur, $t(wN_{max})$ and $t(wN_{min})$, respectively in Experiments 1-7. The first two columns display the maximum and minimum velocities throughout the domain and the two hour integration time.

of the ensuing convection on the magnitude of the low-level wind shear. Experiment 5 is a repeat of Experiment 1 with background vertical vorticity typical of that in a tropical depression. Finally, Experiments 6 and 7 are repeats of Experiments 1 and 2, but have a 70 % stronger wind speed at a height of 2 km and up to 70 % stronger transverse flow in the layer below 2 km, making the wind profile more typical of that in the region of gales in a tropical cyclone. The results of Experiments 2-5 are discussed in sections 6.4-6.6, respectively and those of Experiments 6 and 7 in section 6.7.

As a broad means for making quantitative comparisons of the various experiments, Table 6.2 gives details of the maximum updraught and downdraught strength at selected heights for all experiments and Table 6.3 lists the corresponding maximum and minimum vertical vorticity in these experiments.

Expt.	ζ_{max} 10^{-3} s^{-1}	$z(\zeta_{max})$ km	$\zeta 0.5_{max}$ 10^{-3} s^{-1}	$t(\zeta 0.5_{max})$ min	$\zeta 1_{max}$ 10^{-3} s^{-1}	$t(\zeta 1_{max})$ min	$\zeta 4_{max}$ 10^{-3} s^{-1}	$t(\zeta 4_{max})$ min	$\zeta 1_{min}$ 10^{-3} s^{-1}	$t(\zeta 1_{min})$ min	$\zeta 4_{min}$ 10^{-3} s^{-1}	$t(\zeta 4_{min})$ min
1	32.2	2.5	14.9	20	16.3	22	30.1	28	-13.1	24	-22.1	28
2	33.1	4.0	14.9	20	16.1	22	33.1	28	-13.0	22	-21.1	28
3	22.7	1.5	12.8	18	18.8	22	16.1	34	-13.1	18	-16.8	32
4	24.7	2.5	15.5	18	13.6	38	19.5	32	-9.4	22	-21.6	32
5	35.5	2.5	24.4	20	22.3	24	24.5	28	-10.6	22	-20.3	28
6	31.5	0.0	17.1	18	10.3	32	12.0	42	-7.2	28	-9.3	40
7	31.7	0.0	16.3	18	9.3	34	11.7	40	-7.4	28	-8.0	44

Table 6.3: Maximum of the vertical component of relative vorticity, ζN_{max}, at heights N of 500 m, 1 km and 4 km and the times at which they occur, $t(\zeta N_{max})$, in Experiments 1-7. Shown also is minimum of this vorticity component at a height of 1 km and 4 km, together with the time at which they occur.

6.3   Control experiment

Experiment 1 has a uniform background wind of 10 m s^{-1} above the boundary layer, and no background rotation (Table 6.1). The principal features of updraught evolution are as follows.

6.3.1   Vertical velocity

The maximum updraught and downdraught strengths, w_{max} and w_{min}, are 25.8 m s^{-1} and -10.5 m s^{-1}, respectively (Table 6.2). While w_{max} is comparable to those in the previous chapter, despite the thermal bubble being stronger in this chapter, w_{min}, is larger in magnitude than any found in the previous chapter. An explanation for the stronger downdraught lies in the fact that the larger thermal bubble used in this chapter, in combination with the low-level vertical shear, leads to the development of a convective cell of larger horizontal extent. The cell shown in Figure 6.3 spans about 4 km in the $y-$direction, including the annular downdraught region. In Chapter 5 (Figure 8a) the convective cell spans about 2 km in in the $y-$direction. The larger cell in this chapter contains also more cloud condensate and rain droplets, which strengthens the downdraught by water loading (results not shown).

The upper panels of Figure 6.3 shows horizontal cross sections of vertical velocity at a height of 2 km for Experiment 1 at 24 min and 40 min after the initial time. The earlier time is that at which the updraught velocity is a maximum at this level and the later time is when the downdraught is a maximum. These cross sections are typical of those in the other experiments at similar stages of development. The annular region of downdraught surrounding the updraught core in Figure 6.3(a) is part of the subsiding branch of the upward propagating thermal, and moves upwards with the thermal. This region is separate from the low-level, rain-induced downdraught that occurs at later times. Because of the low-level vertical shear, the updraught at 2 km does not remain symmetric: the subsiding branch of the rising thermal is weaker on the upper-right of the cell, while stronger positive gradients of vertical velocity occur on the left of the cell (Figure 6.3 (a)). The patterns of weak vertical motion outside the subsiding branch of the thermal are presumably gravity waves generated by the cell. At 40 min, when the downdraught at 2 km is a maximum (Figure 6.3 (b)), the updraught at this level has all but decayed, being less than 2 m s^{-1}. The downdraught falls directly into the updraught centre which accelerates the decay of the updraught at this level.

6.3.2   Vertical vorticity

Vorticity structure

The left and middle columns of Figure 6.4 show horizontal cross sections of the vertical component of relative vorticity in Experiment 1 at heights of 1 km (panels (a) and (b)) and 2 km (panels (d) and (e)) at 24 min and 40 min. Regions of ascent exceeding 2 m s^{-1} at
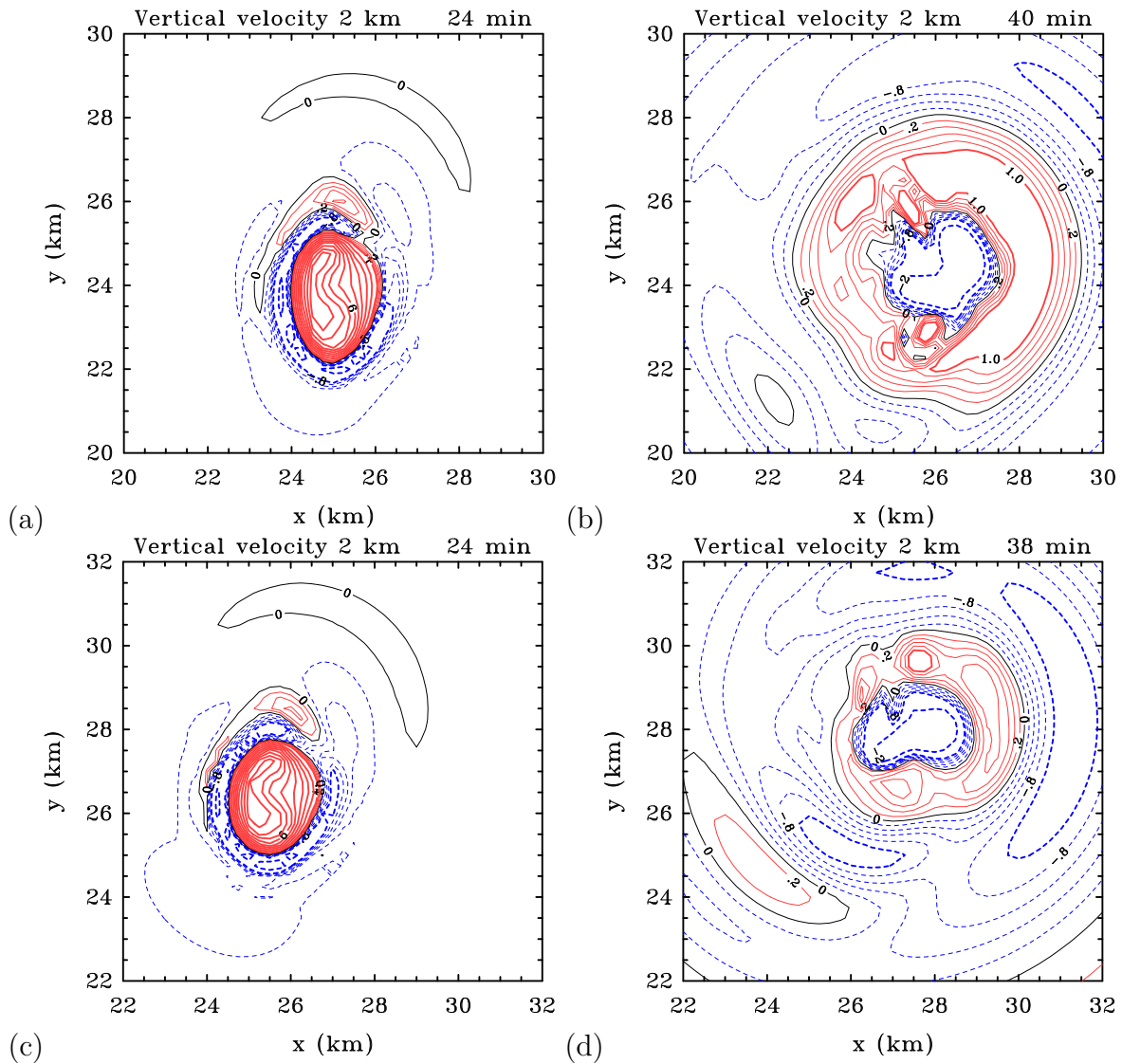
Figure 6.3: Horizontal cross section of the vertical velocity at a height of 2 km in Experiment 1 at: (a) 24 min, and (b) 40 min and in Experiment 2 at: (c) 24 min, and (d) 38 min. The former time for both experiments is when the updraught at this level is a maximum, the latter time when the downdraught is a maximum. Contour interval: thin contours 0.2 m s^{-1} to 0.8 m s^{-1}; thick contours 1 m s^{-1}. Solid (red) contours positive, dashed (blue) contours negative. The thin black curve shows the zero contour.

heights of 2 and 4 km and regions of descent with magnitude exceeding 2 m s^{-1} at heights of 1 km and 2 km are shown also. At 24 min, the vorticity dipole at a height of 1 km is elongated in the south-north[3] direction, as is the vertically-tilted updraught above this level. The axis of the dipole (the line joining the location of the maximum and minimum vorticity) at 1 km has an orientation close to west-east, while the background horizontal vorticity at this height is orientated closer to south-north (see Figure 6.2). It would appear that the pattern of vertical vorticity shown at 24 min at a height of 1 km is dominated by the lifting and tilting of initially horizontal vortex lines *from levels near 200 m* by the updraught, where the horizontal vortex lines are orientated approximately west-east (Figure 6.2). At this time the vorticity dipole at a height of 2 km has an orientation closer to north-south, while a weaker anticyclonic vorticity anomaly remaining to the southwest of the cyclonic anomaly. Animations of the vorticity fields show that the anticyclonic anomaly to the southwest is an extension of the dipole that is present at 1 km and is associated with the lifting and tilting of vortex lines from this level, while the anticyclonic anomaly to the north has formed from the lifting and tilting of horizontal vorticity from heights between 1 and 2 km, where the background horizontal vorticity has a more south-north orientation. These interpretations are supported by an analysis of contributions to the vorticity tendency shown below.

At 40 min, three dipoles are evident at a height of 1 km, while only two are present at 2 km (Figure 6.4(b) and (e)). This complex vorticity pattern is a result of the remnant vorticity produced by the updraught together with new dipole patterns resulting from the downward displacement and tilting of vortex lines by the downdraught. Of course, stretching of vorticity will enhance the local vorticity anomalies and compression will diminish their magnitude [4].

The formation of pairs of vorticity dipoles was discussed in Chapter 5, with animations confirming the subsequent role of the tilting of horizontal vorticity by the convective *downdraught*. Because there was stronger background flow aloft in that chapter, the downdraught developed ahead of the updraught and generated a new vorticity dipole ahead of and largely separate from the older one. In this chapter, in Experiment 1, the absence of vertical shear aloft leads to the downdraught falling directly into the updraught (Figure 6.3(b)). Thus, it is not just mainly the background horizontal vorticity that is being tilted, but rather that which has developed during the updraught phase. Because of the complexity of the vorticity patterns at later times, the value is not clear in performing a quantitative analysis of the contributions to the individual vorticity tendencies from the various processes at later times as it is hard to see how these tendencies might generalize to other situations. Nevertheless, the implications of these complexities are pointed out for understanding the merger of convectively-induced vorticity anomalies during vortex

---

[3]While the orientation of the coordinate axes has no particular significance in these calculations, to aid our description it is assumed that y points northwards and x eastwards.

[4]As mentioned previously the stretching and thereby amplification of ambient (or system-scale) vorticity by convection by itself does not lead to an increase in the circulation around a fixed loop embedded in the flow because stretching leads to a contraction in the areal extent of the amplified vorticity (see Haynes and McIntyre 1987, Raymond *et al.* 2013).

evolution (Nguyen *et al.* 2008, Deng *et al.* 2012). Indeed, the present calculations are seen as a first step in developing such an understanding. The foregoing complexities need to be considered also when appraising the conceptual model for eyewall contraction proposed by Hogsett and Stewart (2013).

Vorticity tendencies

In support of the foregoing interpretations of the vertical vorticity structures given above, an analysis of the contributions of various terms in the tendency equation for vertical vorticity, ζ is now presented. This equation may be written in the form:

$$\frac{\partial \zeta}{\partial t} = -\mathbf{u}_h \cdot \nabla_h (\zeta + f) - w \frac{\partial \zeta}{\partial z} + \frac{\zeta + f}{\rho} \frac{\partial \rho w}{\partial z} + \left(\frac{\partial w}{\partial y} \frac{\partial u}{\partial z} - \frac{\partial w}{\partial x} \frac{\partial v}{\partial z} \right) + \frac{1}{\rho^2} \left(\frac{\partial \rho}{\partial x} \frac{\partial p}{\partial y} - \frac{\partial \rho}{\partial y} \frac{\partial p}{\partial x} \right), \tag{6.3}$$

where ρ is the density, (u, v, w) are the velocity components in the rectangular coordinate system (x, y, z), $\mathbf{u}_h = (u, v, 0)$ is the horizontal velocity vector and ∇_h is the horizontal gradient operator. The five terms on the right-hand-side of (6.3) represent the horizontal advection of ζ, the vertical advection of ζ, the amplification of absolute vorticity by stretching, the tilting of horizontal vorticity $(\xi, \eta, 0)$ into the vertical and the solenoidal generation of ζ, respectively.

Figures 6.5 and 6.6 show the first four vorticity tendencies at a height of 1 km at 14 min and 4 km at 26 min, times at which the updraught was a maximum at these levels (the solenoidal term simply produces toroidal vorticity as a result of the cloud buoyancy). At a height of 1 km, the main contribution to the vorticity tendency is from the vertical advection term, which has a dipole pattern similar to that of the vorticity itself at this time. In contrast, the tilting term is weaker in magnitude and has a dipole pattern oriented approximately north-south reflecting the orientation of background horizontal vorticity at this level (Fig. 6.2). The vorticity tendency from horizontal advection is much weaker in magnitude than the other terms, whereas the stretching term is comparable in magnitude to the tilting term, but has a pattern similar to the sum of the vertical advection and tilting terms.

At 2 km height (not shown) the vertical advection term is dominant also, at least initially. As a result, at early times the structure of the vertical vorticity dipole at this level reflects that at levels below 2 km. However, as the vertical velocity approaches its maximum at 2 km, the other tendency terms becomes appreciable also and lead to a clockwise rotation of the dipole so that its axis is oriented north-south.

At 4 km height, the tendency terms (Figure 6.6) are particularly interesting because this level is well above the height at which there is any background horizontal vorticity to be tilted. Nevertheless, the maximum ζ is 3.1×10^{-2} s^{-1}, which is only marginally smaller than the absolute maximum that occurs at a height of 2.5 km (Table 6.3). Again, the vertical advection tendency term is the dominant one and its structure is similar, therefore, to that of ζ at 4 km. Despite the absence of background horizontal vorticity at
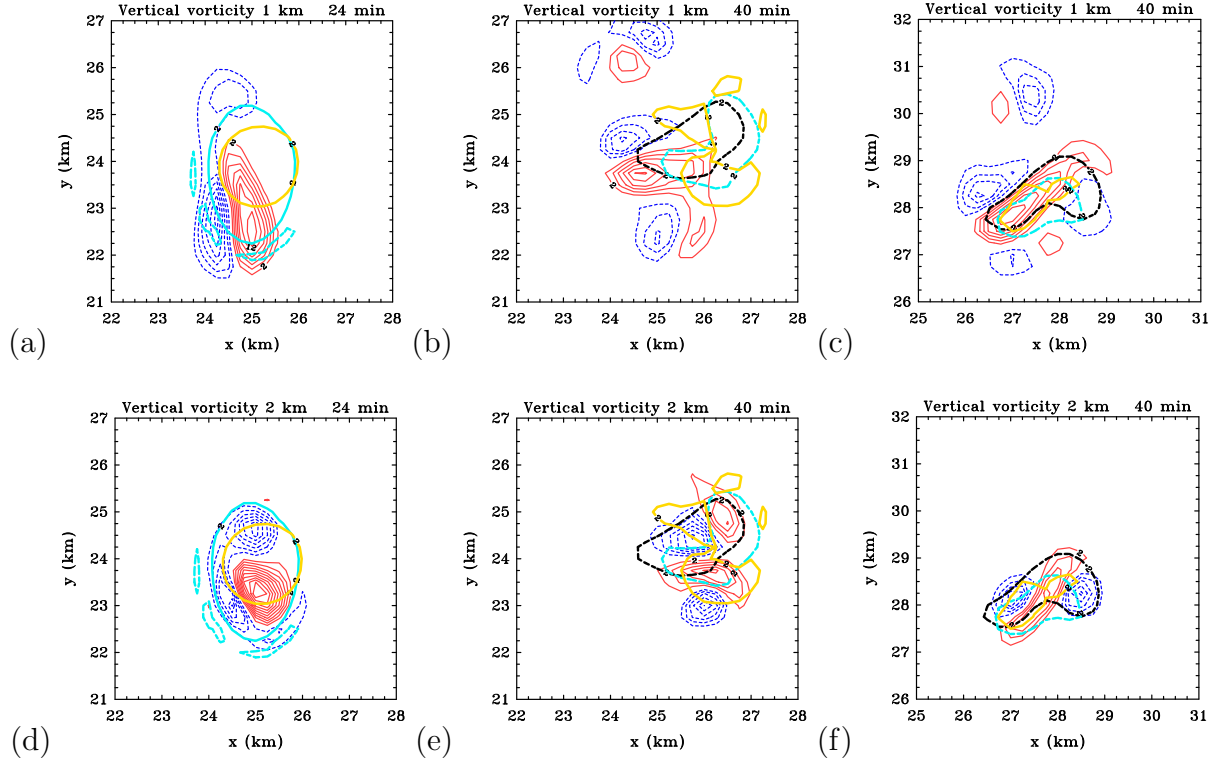
Figure 6.4: Horizontal cross section of the vertical vorticity at heights of 1 km and 2 km in Experiment 1 (a,b,d,e) and Experiment 5 (c,f) at chosen times. Contour interval: 2×10^{-3} s^{-1}. Solid (red) contours positive, dashed (blue) contours negative. The thick solid contours show the 2 m s^{-1} vertical velocity at heights of 2 km (aqua) and 4 km (yellow) and thick dashed contour shows the -2 m s^{-1} vertical velocity at heights of 1 km (black) and 2 km (aqua).

this level, the tilting tendency is non-negligible and is associated presumably with toroidal vorticity generated by the updraught buoyancy (represented by the solenoidal term in Eq. (6.3)). The structure of the stretching term is such as to enhance the magnitude of the dipole, while that of the horizontal advection term is to rotate the dipole clockwise and to shear it. Note that the linear theory of vertical vorticity generation presented by Rotunno (1981) and Rotunno and Klemp (1982) is mute on the structure of the vertical vorticity at levels where there is no background vertical shear.

Vertical vorticity extrema

Details of the maximum and minimum vertical vorticity at selected heights for Experiment 1 are included in Table 6.3. In this experiment, the overall maximum ζ_{max} is 3.2×10^{-2} s^{-1} and occurs at a height of 2.5 km. The maximum vorticity occurs at a relatively low altitude compared to those in Chapter 5 on account of the absence of background horizontal vorticity above a height of 2 km. With the standard wind profile, there is no
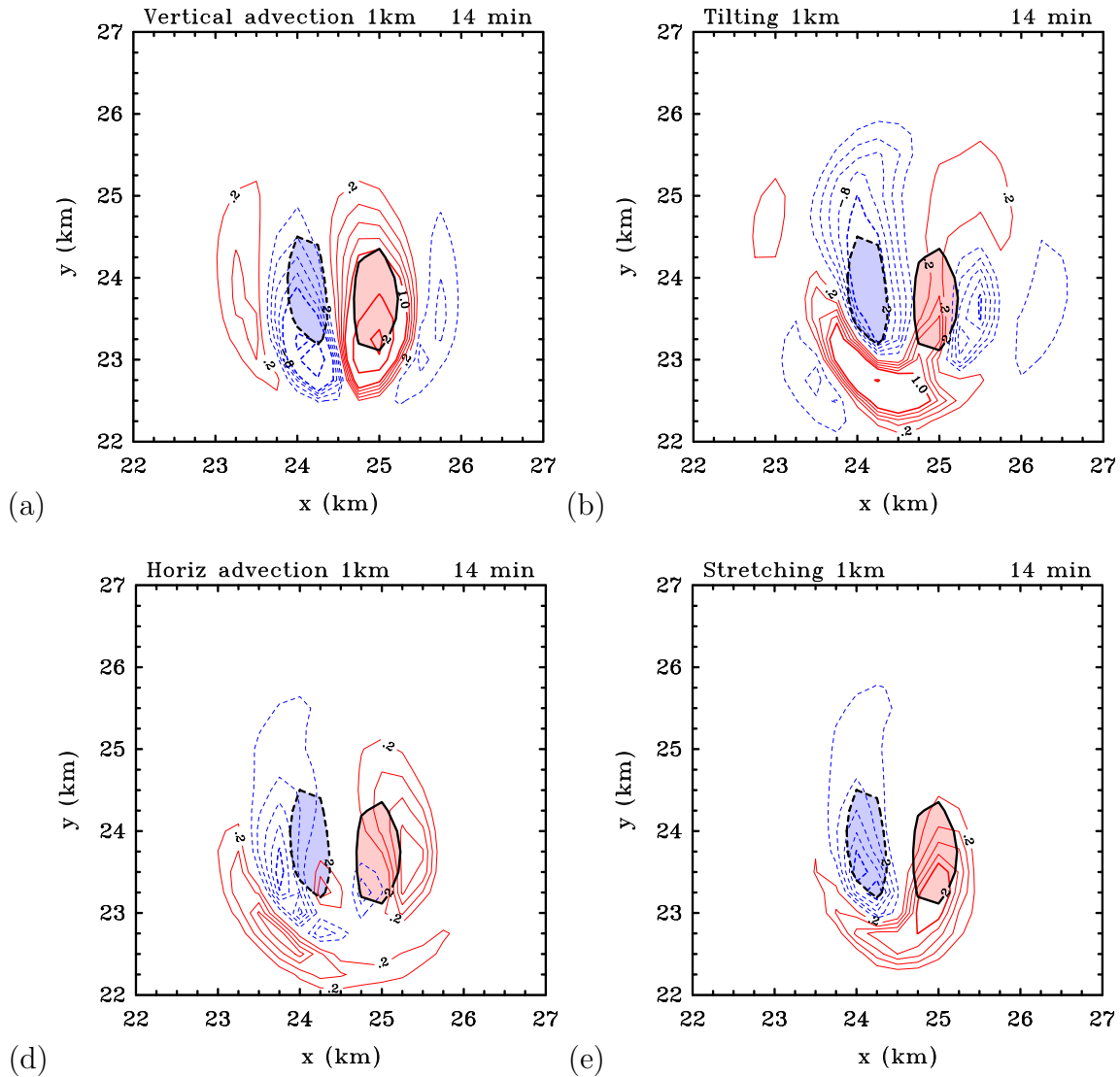
Figure 6.5: Vorticity tendencies at 14 min at a height of 1 km for Experiment 1. Contour interval: thin contours 2×10^{-6} s^{-2} to 8×10^{-6} s^{-2}; thick contours 1×10^{-5} s^{-2} in upper panels, 2×10^{-5} s^{-2} in lower panels. Solid (red) contours positive, dashed (blue) contours negative. The shaded regions enclosed by the black contour shows the 2×10^{-3} s^{-1} positive (solid contour and red shading) and negative (dashed contour and blue shading) vertical vorticity.
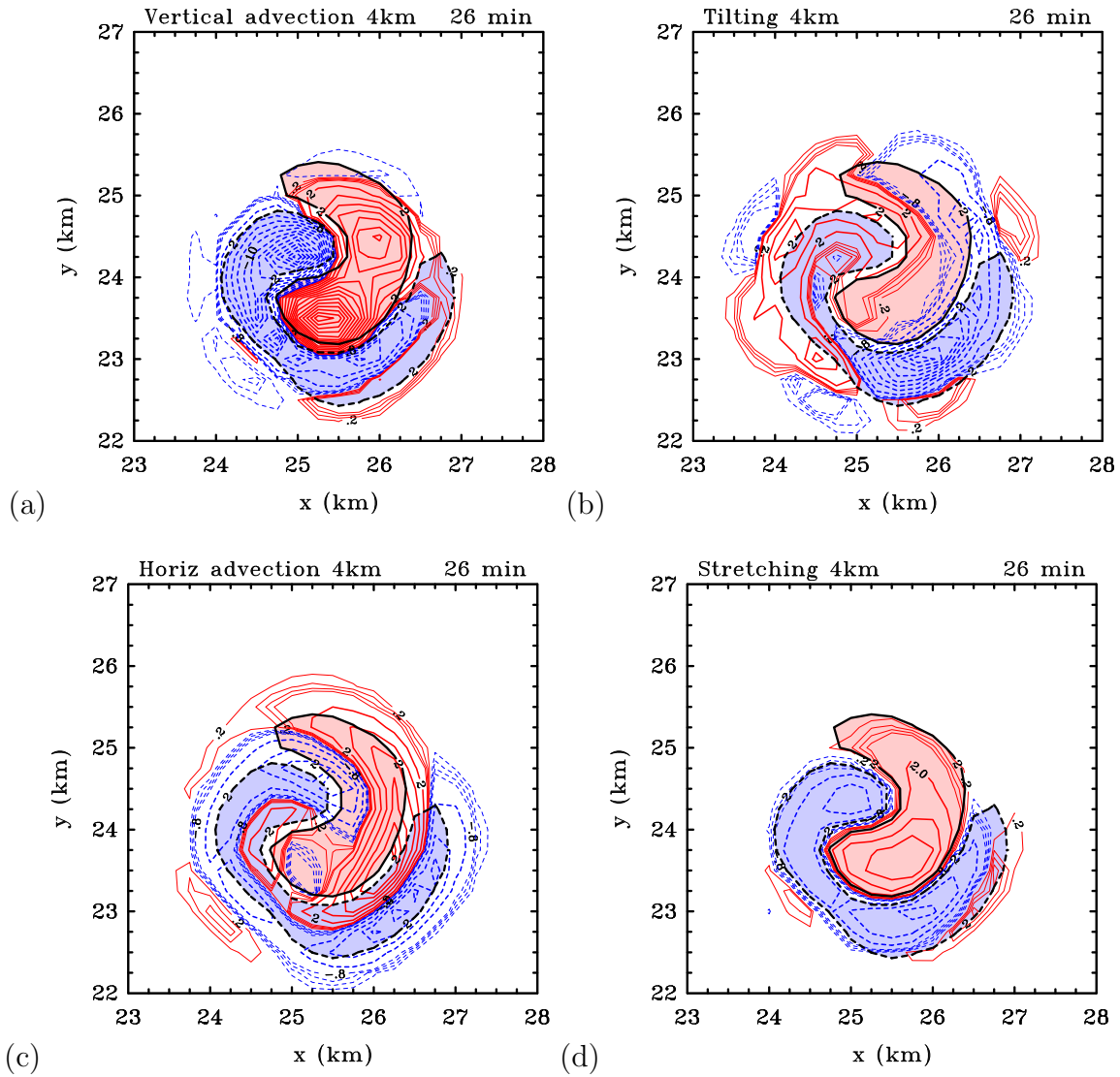
Figure 6.6: Vorticity tendencies at 26 min at a height of 4 km for Experiment 1. Contour interval: See Figure 6.5

background vertical shear and therefore no horizontal vorticity to be tilted at these levels. The maximum vorticity at a height of 1 km, $\zeta 1_{max}$ is 1.6×10^{-2} s^{-1}, while the minimum vorticity at this height, $\zeta 1_{min}$ is -1.3×10^{-2} s^{-1}. The difference in the magnitude between $\zeta 1_{max}$ and $\zeta 1_{min}$ is due to the clockwise turning hodograph, which, as noted above, favours the cyclonic member of the vorticity dipole. The magnitude of the cyclonic vorticity at a height of 4 km, $\zeta 4_{max}$, is larger also than that of the anticyclonic vorticity, $\zeta 4_{min}$, which have values of 3.0×10^{-2} s^{-1} and -2.2×10^{-2} s^{-1}, respectively.

All experiments have a background wind hodograph that turns clockwise with height. As found by Klemp and Wilhelmson (1978) this turning results in the cyclonic member of the vorticity dipole becoming the dominant one. An explanation for this result was given by Rotunno and Klemp (1982). They showed that, in the presence of vertical shear, dynamic pressure perturbations are induced with a high pressure anomaly forming on the upshear side of the updraught and a low pressure anomaly forming on the downshear side. If the shear vector does not change direction with height, these pressure anomalies will be stacked vertically, whereas when the shear vector rotates clockwise with height, so does the induced pressure anomaly dipole. When the induced pressure anomaly dipole rotates clockwise with height, a favourable vertical pressure gradient is created to enhance the updraught in the region of the cyclonic vertical vorticity anomaly, i.e. cyclonic vorticity and updraught production are positively correlated. A stronger updraught over the cyclonic vorticity anomaly leads to an increase in cyclonic vorticity production by tilting and stretching.

Tendency for updraught splitting

Figure 6.7 shows the evolution of the vorticity dipole at a height of 2 km in Experiment 1 from 20 to 36 min. The orientation of the dipole rotates clockwise with time from a west-east orientation at 20 min, to a north-south orientation at 28 and 36 mins. The background flow at this height is southerly, and at lower levels it has an easterly component (Figure 6.2). At 28 min there is a split of the updraught at a height of 2 km, with two distinct updraught cores, one over each member of the vorticity dipole. These two cores are separated by a downdraught which falls through the middle of the vorticity dipole. The split is not seen at higher levels, as shown by the thick (yellow) vertical velocity contour at a height of 4 km. By 36 min the split updraughts have all but decayed and the downdraught has grown in horizontal extent. An updraught at a height of 4 km still occurs, although it is smaller in horizontal extent than 8 min earlier. Presumably, in a more unstable environment, the downdraught induced spreading cold pool could lift the environmental air to its LFC, leading to the formation of a classic supercell storm.

Figure 6.8 shows vertical cross sections of vertical velocity in the x-z and y-z planes through the location of w_{max} (panels a and b). It shows also vertical cross sections of vertical vorticity in the x-z plane through the location of maximum relative vorticity at a height of 2 km (panel c). Panels (a) and (b) show a relatively asymmetric cell with the updraught maximum located near a height of 4 km. The strongest downdraught at this time occurs in an annular region around the updraught core at a height of about 4 km. This downdraught is part of the subsiding branch of the upward propagating thermal. The
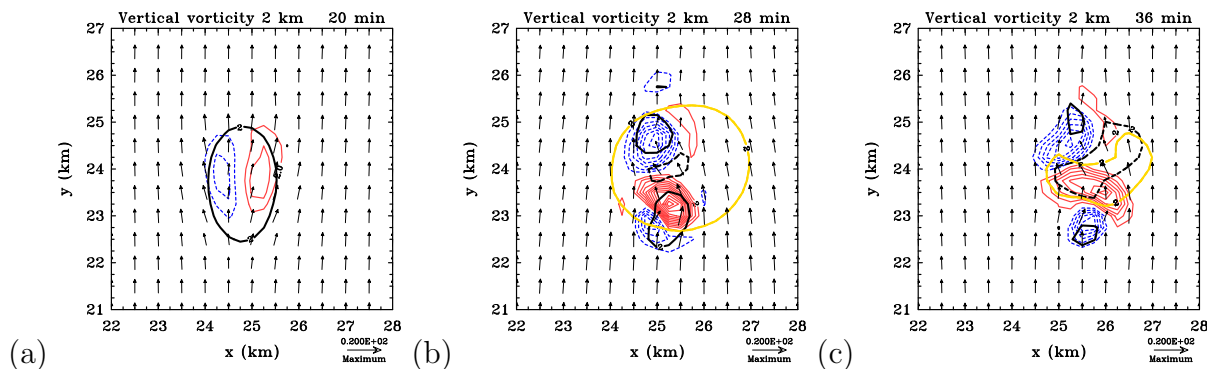
Figure 6.7: Horizontal cross sections of vertical vorticity for Experiment 1 at a height of 2 km. Contour interval: vertical vorticity contours 2×10^{-3} s^{-1}. Solid (red) contours positive, dashed (blue) contours negative. Vertical velocity: thick countour 2 m s^{-1}, solid (black) contour positive, dashed (black) contour negative. The thick solid yellow contour shows the 2 m s^{-1} vertical velocity at a height 4 km. Wind vectors are relative to the maximum vector at the bottom right of the plot. The uniform flow, added to the wind profile before the calculation in order to keep the convection near the centre of the computational domain, is subtracted here.

effects of the vertical wind shear in tilting the updraught with height are clearly evident in the y-z plane, but less so in the x-z plane. The developing cell split can be seen in the y-z plane, and occurs as water loading in the core of the cell begins to decelerate the updraught at mid-levels and to induce a downdraught at lower levels (not shown). The 2 km horizontal cross section of vertical velocity at a later time (Figure 6.3 (b)) shows also that the downdraught falls directly beneath the updraught, while weak ascent remains in a ring around the downdraught. In this connection it is worth recalling that the development of water loading in the updraught and the subsequent formation of a downdraught is not an essential requirement for storm splitting, but it accelerates the splitting process (Rotunno and Klemp 1985).

The vorticity structure in the y-z cross sections (Figure 6.8c) shows an inner dipole structure with cyclonic vorticity to the left and anticyclonic vorticity to the right, embedded in a weaker dipole structure outside of it with cyclonic vorticity to the right and anticyclonic vorticity to the left. To understand this structure, it is noted that the buoyancy of the rising thermal creates toroidal vorticity, which, together with the ambient horizontal vorticity, is tilted by the horizontal gradient of vertical velocity and further processed. Interestingly, in Figure 6.8 (c), there is only very weak anticyclonic vorticity located below a height of about 1.7 km, in comparison to the relatively large cyclonic anomaly. This feature is evident also in a parallel slice through the vertical vorticity minimum (not shown). Rotunno (1981) shows similar results where the low-level cyclonic vorticity is dominant. He attributes this dominance to vortex stretching, which is most prominent at low levels. As the clockwise turning hodograph favours cyclonic vertical vorticity production by vortex line tilting, the stretching term then enhances the low-level vertical vorticity anomaly more than the
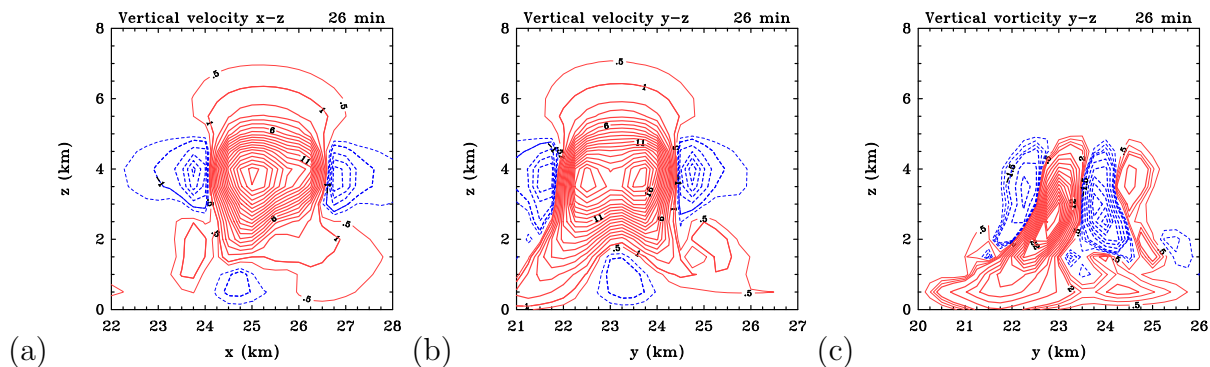
Figure 6.8: Panels (a) and (b) show vertical cross sections (x-z and y-z) of vertical velocity through the centre of the domain w_{max} at 26 mins for Experiment 1. Panel (c) shows a vertical cross section (y-z) of vertical vorticity through the centre of the $\zeta 2_{max}$ at 26 mins for Experiment 1. Contour interval: vertical velocity: thin contour 0.5 m s^{-1}; thick contours 1 m s^{-1}, vertical vorticity thin contours 5×10^{-4} s^{-1} to 1.5×10^{-3} s^{-1} and thick contours 2×10^{-3} s^{-1}. Solid (red) contours positive, dashed (blue) contours negative.

anticyclonic one. Over time both dipole anomalies diminish in strength due to vortex-line compression by the downdraught, but the stronger cyclonic anomaly persists at later times.

Vorticity maximum evolution

Figure 6.9 shows time-height cross sections of the maximum and minimum vertical vorticity (which may not occur at the same horizontal location) in Experiment 1. Note that significant vertical vorticity is generated up to a height of about 10 km (Panel a), even though there is no horizontal vorticity above a height of 2 km and no background vertical vorticity at all. Thus, the vertical advection and tilting of vortex lines originating in the boundary layer has a significant effect through a large depth of the troposphere. The maximum cyclonic and anticyclonic vorticity occurs between 2 and 4 km and persists longest within this height range. This result has implications for the barotropic merger of convectively-induced vorticity anomalies during vortex evolution and for the conjecture of Hogsett and Stewart (2013), which does not include a boundary-layer-type wind profile in their theory.

Section summary

In summary, the convective cell develops a dipole vertical vorticity structure due to the lifting and tilting of background horizontal vortex lines into the vertical. Due to the clockwise turning hodograph, the cyclonic vorticity maximum at various heights is stronger in magnitude than the anticyclonic vorticity minimum. The clockwise turning hodograph affects also the orientation of the dipole of vertical vorticity, which rotates clockwise with height, in line with the turning of the horizontal vorticity vectors. The rotation of the vertical vorticity dipole is explained by the vertical advection of vertical vorticity from
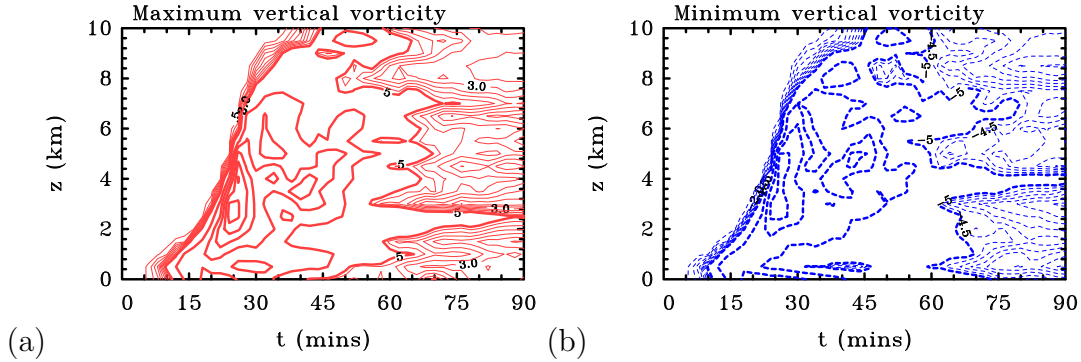
Figure 6.9: Time-height series of maximum vertical vorticity (a) and minimum vertical (b) vorticity in Experiment 1. Contour interval: thin contours 0.5×10^{-3} s^{-1} to 4.5×10^{-3} s^{-1}; thick contours 5×10^{-3} s^{-1}.

lower levels. Vertical vorticity forms first at lower levels by the tilting of horizontal vorticity lines that are orientated in the west-east direction. This tilting forms a west-east orientated vertical vorticity dipole, and the updraught advects the structure upwards. At larger heights in the boundary layer the horizontal vorticity lines are rotated into a south-north direction. Vertical vorticity generated by tilting at these heights leads to a south-north orientated dipole. The vertical vorticity profiles at larger heights are constructed from the advection from lower levels as well as from tilting and stretching at the current level.

Tilting of horizontal vorticity occurs from the surface to a height of 2 km, where the background horizontal vorticity becomes zero. Above a height of 2 km the vertical vorticity can further be strengthened by stretching. The lifting of vortex lines from the boundary layer by the updraught plays an important role, as significant magnitudes of vertical vorticity are found up to a height of 10 km. This result has implications for the barotropic merger of convectively-induced vorticity anomalies during vortex evolution and for the conjecture of Hogsett and Stewart (2013), which do not include a boundary-layer-type wind profile in their theory.

6.4   Negative vertical shear above the boundary layer

Experiment 1 was designed to isolate the effects of boundary-layer shear, but, of course, the assumption of no shear above the boundary layer is not particularly realistic. For this reason, Experiment 2 is a repeat of Experiment 1 with a negative vertical wind shear profile for the meridional wind component (V) above a height of 2 km. Below this height, the wind profile is identical to that used in Experiment 1. This experiment is an extension of Experiments 2 and 3 in Chapter 5, which both had a low-level layer of positive vertical wind shear underlying an upper layer of negative vertical shear, but there the shear was everywhere unidirectional.

The most notable differences between the vertical velocity maxima and minima in

Experiment 2 compared with those in Experiment 1 are the slightly larger maximum at a height of 9 km and the stronger downdraught at a height of 2 km (Table 6.2). The value of ζ_{max} in Experiment 2 is similar also to that in Experiment 1 (Table 6.3). The maximum at heights of 500 m and 1 km are almost identical in both experiments, which is expected as both have identical wind profiles below a height of 2 km. The maximum at a height of 4 km is larger in Experiment 2, which is due to the additional vertical vorticity generated by the tilting of horizontal vorticity above a height of 2 km.

In Chapter 5 it was shown that a convective cell that develops in an environment where the horizontal vorticity changes sign at some height has a vertical vorticity dipole that reverses in sign with height. Figure 6.10 shows horizontal cross sections of the vertical component of relative vorticity in Experiment 2, at various times and heights. The top panels of Figure 6.10 show the vorticity dipole at early times and at lower levels, where the background vertical wind shear is positive. There is a vertical vorticity dipole that "twists" and changes its orientation with height, similar to the vorticity dipoles shown above. The lower panels of Figure 6.10 show the vorticity dipole at heights where the background vertical shear is negative. The vertical vorticity dipole reverses in sign between heights of 4 km and 6 km, similar to Experiments 2 and 3 in Chapter 5. The dipole at a height of 4 km is the smallest in horizontal extent of all heights shown as it nears the height where it reverses in sign.

In summary, the convective cell that develops in an environment with a clockwise turning hodograph in the boundary layer, and with negative shear above that, develops a vertical vorticity dipole that rotates at lower levels with height and time, and reverses in sign at mid-upper levels. The rotation of the dipole occurs as described in previous sections, and is due to the rotation of the horizontal vorticity vectors associated with the clockwise turning hodograph. Above the boundary layer the horizontal vorticity reverses in sign as the vertical shear becomes negative, and the vertical vorticity dipole reverses also in sign, corroborating results from Chapter 5.

6.5   Stronger and weaker background flow

Experiments 3 and 4 are repeats of Experiment 1 with different magnitudes of background wind speed aloft, V_a, which is 5 m s^{-1} in Experiment 3 and 15 m s^{-1} in Experiment 4, compared to 10 m s^{-1} in Experiment 1 (Table 6.1). Thus Experiment 3 has weaker vertical shear at low levels than in Experiment 1, while Experiment 4 has stronger vertical shear.

The magnitudes of w_{max} and w_{min} found in Experiment 3 are the largest of all the experiments performed, with values of 28.4 and 11.7 m s^{-1}, respectively (Table 6.2). This result is consistent with the findings of Rozoff (2007), Wissmeier and Smith (2011) and Chapter 5 that convective cells rising in a environment with weaker vertical or horizontal shear tend to have the strongest vertical velocities. In Experiment 3 the $w2_{max}$, $w5_{max}$ and $w9_{max}$ occur sooner than in any other experiment, while the $w2_{max}$ and $w9_{max}$ are the largest found in this chapter. In the weakly-sheared environment the initial thermal experiences less deformation and develops more rapidly, a result found also in the previous
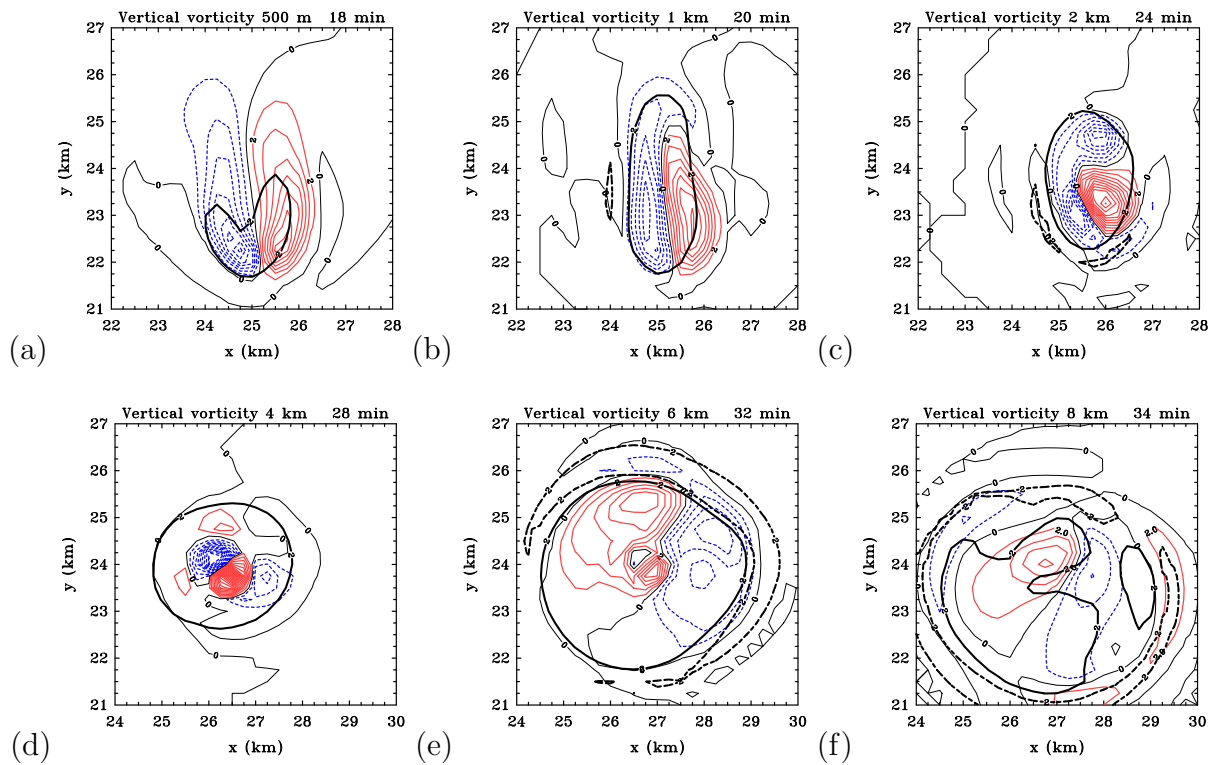
Figure 6.10: Horizontal cross section of the vertical vorticity at various heights in Experiment 2 at chosen times. Contour interval: 2×10^{-3} s^{-1}. Solid (red) contours positive, dashed (blue) contours negative. The thin black curve shows the zero contour. The thick black solid contour shows the 2 m s^{-1} vertical velocity and thick black dashed contour shows the -2 m s^{-1} vertical velocity.
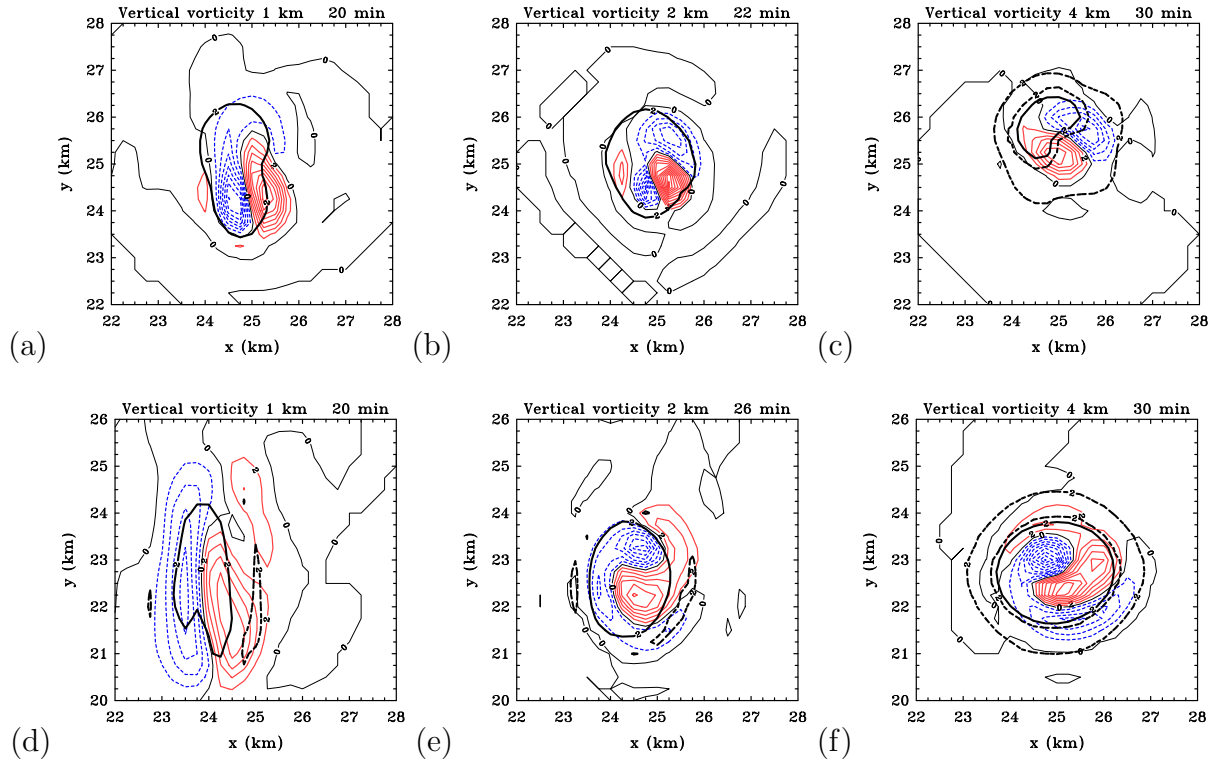
Figure 6.11: Horizontal cross section of the vertical vorticity at heights of 1 km, 2 km and 4 km in Experiment 3 (a, b and c) and Experiment 4 (d, e and f) at chosen times. Contour interval: see Figure 6.10.

chapter. In contrast, the magnitude of w_{max} and w_{min} in Experiment 4 are smaller than those in Experiment 3, and are more comparable to those in Experiment 1. Further, $w2_{max}$, $w5_{max}$ and $w9_{max}$ occur later because of the larger deformation of the initial thermal by the stronger vertical shear.

Despite having the largest w_{max}, Experiment 3 has the smallest ζ_{max}, $\zeta0.5_{max}$ and $\zeta4_{max}$ in this chapter (Table 6.2). The reason may be traced to the smaller vertical wind shear, and thus smaller magnitude of low-level horizontal vorticity available to be tilted into the vertical. In contrast, the ζ_{max} in Experiment 4 is smaller in magnitude than that in Experiment 1 for a different reason. The larger magnitude of vertical shear in this experiment leads to a weaker low-level updraught (see Table 6.2), which, in turn, leads to a weaker ζ_{max} in this experiment than in Experiment 1, despite there being a larger magnitude of horizontal vorticity available to be tilted into the vertical (recall that all of the background horizontal vorticity is located below a height of 2 km).

Horizontal cross sections of the vertical component of relative vorticity at heights of 1, 2 and 4 km in Experiments 3 and 4 are shown in Figure 6.11 at particular times. At 20 min, and at a height of 1 km, the vorticity dipole in Experiment 3 has a slightly north-westerly orientation (panel (a)) while at a height of 4 km (panel (c)), the dipole is orientated in a more north-westerly direction. At 22 min (panel (b)) there is a vorticity tripole, with

negative patches of vorticity on the east and north of the positive vorticity patch. This structure is similar to that shown in Figure 6.4 (d) and Figure 6.7 (b) where there is a *twisting* of the original dipole. A new negative vorticity patch develops north of the original dipole, while the old negative patch in the dipole decays. In Experiment 4 (panels d, e and f) the vorticity dipole at a height of 1 km is larger in horizontal extent when compared to Experiment 3. This is due to the increased deformation of the initial thermal bubble at early times by the larger vertical wind shear. By 30 min, the vorticity dipole is orientated in a north-easterly direction, a difference of about 90 degrees in the clockwise direction when compared to the dipole in Experiment 3.

In summary, the convective cell rising in the experiment with weak vertical shear has the strongest updraught and downdraught in this chapter. In this weakly-sheared environment, the initial thermal experiences less deformation and develops more rapidly, so the updraught reaches a maximum at any height sooner than in the other experiments. In contrast, the updraught maximum at a particular height occurs later in the strongly-sheared environment because of the larger deformation of the initial thermal by the stronger vertical shear. Despite having the largest updraught maximum, the experiment with weak vertical shear has the smallest vertical vorticity maximum because of the smaller vertical wind shear, and thus smaller low-level horizontal vorticity available to be tilted into the vertical.

6.6   Effects of background rotation

Tropical depressions and tropical cyclones have elevated levels of background vertical vorticity enabling vortex tube stretching to play an important role in the amplification of vertical vorticity. As a first step to examine the effects of background vertical vorticity Experiment 1 is repeated but with an f-plane with Coriolis parameter $f = \zeta_o$ (see section 6.2.4). This calculation is designated as Experiment 5.

The maximum and minimum vertical velocities in Experiments 1 and 5 are largely comparable (Table 6.2), although the w_{max} is a little less than in Experiment 1 and the magnitude of w_{min} is a little larger. Experiment 5 has also a slightly smaller $w5_{max}$ when compared to Experiment 1. These results corroborate those of Wissmeier and Smith (2011), who showed a reduction in the updraught maximum in the presence of ambient vertical vorticity.

Panels (c) and (d) of Figure 6.3 show horizontal cross sections of vertical velocity at a height of 2 km for Experiment 5 at 24 min and 38 min after the initial time. The earlier time is that at which the updraught velocity is a maximum at this level and the later time is when the downdraught is a maximum. The features are largely similar to those of Experiment 1, shown in panels (a) and (b)), respectively, especially at 24 min, although at the later time, the ring of convection encircling the convective downdraught is weaker and smaller in horizontal extent in Experiment 1.

Figures 6.4(c) and (f) show horizontal cross sections of the vertical component of relative vorticity in Experiment 5 at 40 min. Plots at the earlier times are not shown for this

experiment as they are practically identical to the corresponding plots shown for Experiment 1. At 40 min the vorticity features in Experiment 5 are quite different to those in the corresponding plots for Experiment 1 (compare middle and right columns of Figure 6.4). The positive vorticity anomaly at a height of 1 km is slightly stronger (compare panels b and c) while the quadrapole structure at a height of 2 km has been replaced by a tripole vorticity structure (compare panels (e) and (f) of Figure 6.4). The downdraught is centred on the positive vorticity anomaly in both the 1 km and 2 km plots for Experiment 5. As discussed in section 6.3.2, the downdraught falling into the vicinity of the initial vorticity dipole leads to a complex pattern of vertical vorticity resulting from the tilting of horizontal vorticity by the convective downdraught. In this case a vorticity tripole emerges where a larger patch of positive vorticity is flanked by two smaller negative patches. This finding may have further implications for understanding the merger of convectively-induced vorticity anomalies during vortex evolution.

The larger value of ζ_{max} in Experiment 5 (3.6×10^{-2} s^{-1} compared with 3.2×10^{-2} s^{-1} in Experiment 1) is to be expected because of the additional amplification of existing vertical vorticity by stretching in regions where the vertical gradient of mass flux is positive.

In Chapter 5 it was shown that presence of background vertical vorticity strengthens the vertical vorticity maximum at low levels, where the vertical gradient of updraught mass flux is positive. This is the case also in Experiment 5, where $\zeta 0.5_{max} = 2.4 \times 10^{-2}$ s^{-1}, compared with 1.5×10^{-2} s^{-1} in Experiment 1. In contrast, the vorticity maximum at a height of 4 km, $\zeta 4_{max}$, is smaller in Experiment 5 than in Experiment 1. In both experiments there is little contribution to vorticity generation by stretching at this height, because the vertical gradient of mass flux is relatively small. The updraught in Experiment 5 is slightly weaker at mid-levels as the presence of ambient vertical vorticity reduces updraught strength (Wissmeier and Smith 2011). The weaker updraught leads to a weaker vertical vorticity maximum at mid-levels in Experiment 5 as there is less horizontal vorticity tilted into the vertical (compare $\zeta 4_{max}$ of Experiments 1 and 5 in Table 6.3 and $w5_{max}$ in Table 6.2). The vorticity maximum at a height of 4 km is larger in magnitude than the minimum at the same height. Due to the combination of the clockwise turning hodograph and the stretching of background cyclonic vorticity at low levels the magnitude of the 1 km maximum is over twice as large as the magnitude of the minimum at this height.

Figure 6.12 shows time-height cross sections of the maximum and minimum vertical vorticity in Experiment 5. Features to notice are that there is a significant generation of vertical vorticity near the surface between 10 and 30 min in Experiment 5 (panel (a)) when compared to the experiment without background rotation (Figure 6.9a). The amplified vorticity at the surface persists until 90 min. The minimum vertical vorticity decreases in magnitude at low levels when background rotation is included, and this anticyclonic vorticity decays sooner than in the experiment without background rotation (compare Figures 5.12b and 6.9b).

In summary, the presence of background vertical vorticity leads to an increase in the vertical vorticity maximum, the increase being most pronounced at low levels. This increase may be attributed to the additional stretching of background vertical vorticity at low levels. The low-level cyclonic vorticity persists longer while the low-level anticyclonic vorticity
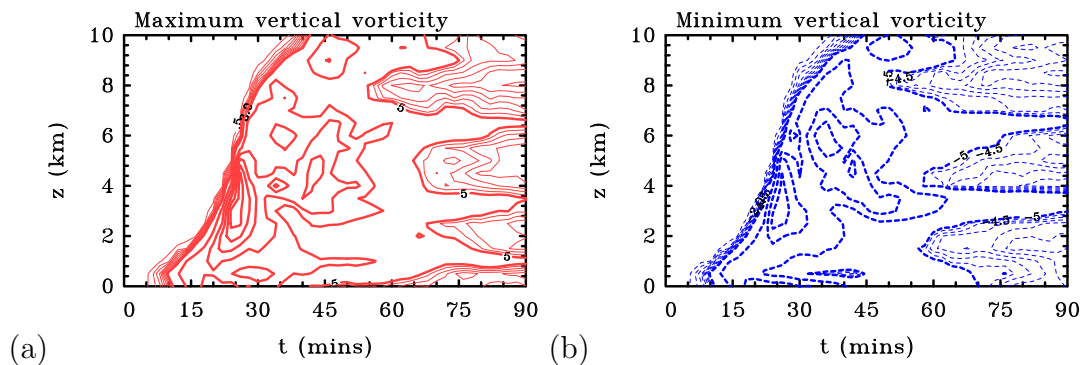
(a)   (b)

Figure 6.12: Time-height series of maximum vertical vorticity (a) and minimum vertical vorticity (b) in Experiment 5. Contour interval: thin contours 0.5×10^{-3} s^{-1} to 4.5×10^{-3} s^{-1}; thick contours 5×10^{-3} s^{-1}.

decays sooner than in an environment without background rotation.

6.7   Tropical cyclone boundary layer

Tropical depressions and tropical cyclones have not only elevated levels of background vertical vorticity, but because of the larger wind speeds, they represent convective environments with elevated levels of low-level horizontal vorticity as well. Experiments 6 and 7 are designed to investigate the growth of convection in such environments. These have a vertical wind profile characteristic of the boundary layer in the outer region of a tropical cyclone with gale force winds (17 m s^{-1}) assumed above the boundary layer and, like Experiment 5, they include background rotation. The difference between the experiments is that Experiment 6 has a uniform background flow above the boundary layer, while Experiment 7 has negative uniform shear like Experiment 2, making it more realistic vis-à-vis tropical cyclones. The stronger background wind speed in these experiments gives a larger vertical shear[5] at low levels (see Figures 6.1 and 6.2), which has an appreciable effect on the strength of the updraught and downdraught.

The magnitude of w_{max} found in Experiment 6 is the smallest of all the experiments performed, with a value of 18.5 m s^{-1} (Table 6.2). The larger shear delays the updraught considerably, with the $w2_{max}$, $w5_{max}$ and $w9_{max}$ occurring up to 14 min later than in Expt 1. Further, the $w5_{max}$ of 18.5 m s^{-1} is more than 5.5 m s^{-1} smaller than in any previous experiment.

The value of ζ_{max} in Experiment 6 is comparable to that in Experiment 1 (see Table 6.3) and occurs at the surface, lower than in any previous experiment. A similar result

---

[5]It may be worth noting that the magnitude of vertical shear used here is relatively weak when compared to that in previous studies. The vertical winds in Experiment 7 change by about 6 m s^{-1} in magnitude over the depth 2-8 km, whereas in Rotunno and Klemp (1982) the vertical winds change in magnitude by 30 m s^{-1} over a depth of 0-4 km. Stern and Nolan (2011) show a decay of roughly 10 m s^{-1} of the tangential winds in the 2-8 km layer over a range of TC cases and intensities.

was found also in Experiment 7 of Chapter 5, which included the same level of background rotation. The amplification of background vorticity by stretching plays an important role in generating vorticity at low levels and would explain why the vorticity maximum is located at the surface. The maximum vorticity at a height of 500 m is relatively large (1.7×10^{-2} s^{-1}) and comparable to those found in other experiments, yet the maximum at a height of 1 km is 1.0×10^{-2} s^{-1}, smaller than in any previous experiment. Even though the low-level updraught is weaker than in most other experiments (see Table 6.2), the magnitude of horizontal vorticity at a height of 500 m is larger than in all other experiments (see Figure 6.2), enabling the weaker updraught to generate a vertical vorticity maximum that is comparable to those in other experiments at this height. Because of the presence of background rotation, the stretching of vertical vorticity is important at this height also. At a height of 1 km, the magnitude of the background horizontal vorticity is comparable to that in the other experiments (see Figure 6.2), and the weaker low-level updraught leads to a smaller value of $\zeta 1_{max}$ than in the previous experiments.

Experiment 7 has similar values of vertical velocity to Experiment 6, but the maximum is marginally stronger. The value of ζ_{max} in this experiment is almost identical to that in Experiment 6 (31.5×10^{-3} s^{-1} compared with 31.7×10^{-3} s^{-1}) and occurs also at the surface. These small differences are not surprising because both experiments have the same boundary-layer wind profile.

Figure 6.13 shows isopleths of the perturbation pressure, the 1 m s^{-1} contours of vertical velocity, which delineate the updraught and downdraught, and regions of vertical vorticity exceeding 1×10^{-3} s^{-1} in magnitude for Experiment 7 at 16 min at a height of 1 km. The fields in Experiment 6 at this time are nearly identical (not shown), a result to be expected since both experiments have the same configuration in the lowest 2 km. These fields are similar to those shown in Rotunno and Klemp (1982, their Fig. 4). As discussed earlier these authors explained the perturbation pressure distribution in terms of linear theory, showing that high pressure forms on the upshear flank of the updraught and low pressure on the downshear flank, while vertical vorticity perturbations are aligned perpendicular to the shear vector.

The shear vector at a height of 1 km in Experiment 7 points west-east (see Figure 6.2) so that, according to the linear theory of Rotunno and Klemp (1982), the vertical vorticity dipole should be aligned perpendicular to the shear vector. This is clearly not the case in Fig. 6.13 and points to the importance here of the vertical advection terms in the vorticity tendency equation (Equation 6.3), which are absent in the linear theory. This inference is based on the orientation of the vortex dipole at 1 km, which is aligned with the shear vector at a height of about 200 m. The inaccuracy of the linear theory evidently flows through to interpreting the pressure distribution, which even in the sheared boundary layer, is not as expected on the basis of the linear theory.

While the updraught is slightly stronger at mid-levels in Experiment 7 than in Experiment 6, $\zeta 4_{max}$ is slightly smaller. A possible reason for the smaller $\zeta 4_{max}$ is that, at this height, the updraught in Experiment 7 is beginning to tilt horizontal vorticity that has the opposite sign to that at lower levels, due to a reversal of the vertical shear vector with height. The local tilting at a height of 4 km may actually act to weaken the existing dipole
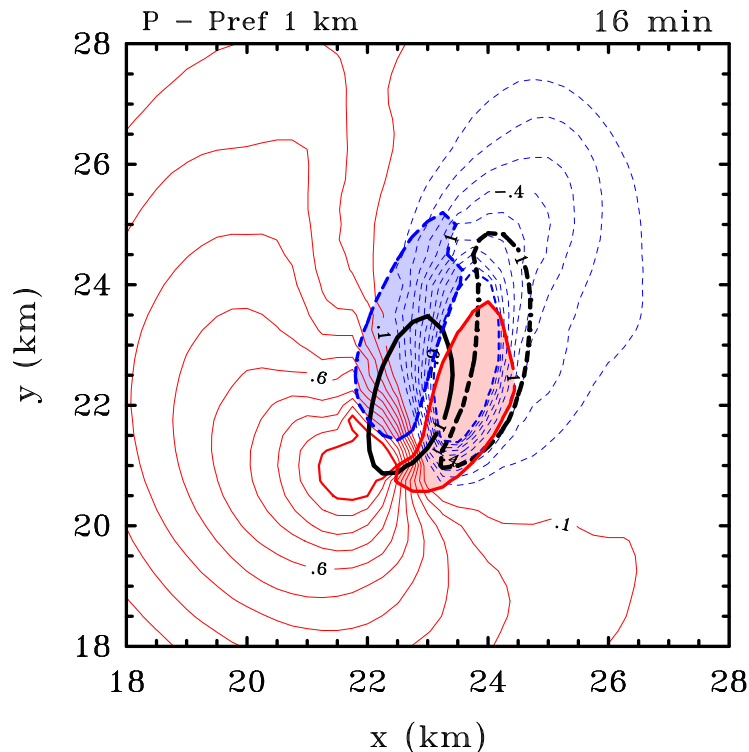
Figure 6.13: Pressure perturbation plot for Experiment 6 at a height of 1 km at 16 min. The plot depicts the time when the updraught reaches this level. Contours: thin contours 1×10^{-2} hPa to 9×10^{-2} hPa; thick contours 1×10^{-1} hPa. Solid (red) contours positive, dashed (blue) contours negative. The thick black solid contour shows the 1 m s^{-1} vertical velocity and thick black dashed contour shows the -1 m s^{-1} vertical velocity. Vertical vorticity contours: 1×10^{-3} s^{-1}. Thick solid (red) contour positive, dashed (blue) contour negative. Regions of vertical vorticity shaded (red) positive and (blue) negative.

that was advected upwards, before it reverses in sign. At a height of 6 km, the tilting of horizontal vorticity associated with the negative vertical shear becomes apparent because the vertical vorticity dipole at that level has a reversed sign to that at 4 km (the fields are not shown as they are qualitatively similar to those in Figures 6.10(d) and (e)). The value of $\zeta6_{max}$ is 2.3×10^{-2} s^{-1} in Experiment 7 compared with only 4.6×10^{-3} s^{-1} in Experiment 6, suggesting that the tilting of the horizontal vorticity associated with the negative vertical shear above the boundary layer becomes important at a height of around 6 km.

At this point it is worth returning to the argument of Deng *et al.* (2012) that the development of vortex dipoles in updraughts in the presence of strong low-level vertical shear inhibits the aggregation of cloud-induced vorticity, and is thereby detrimental to the formation of a larger-scale vortex. The results of this chapter show that while the magnitude of the low-level vertical shear has a strong effect on vertical vorticity generation, the anticyclonic anomaly is weakened in the presence of both background rotation and a

clockwise turning hodograph, which is typical of a warm cored vortex boundary layer. As shown by Rotunno and Klemp (1982), the turning hodograph leads to a positive vertical perturbation pressure gradient that enhances the updraught in the region of the cyclonic vorticity anomaly. The result is that the stronger updraught strengthens the cyclonic vorticity anomaly at low-levels as a result of stretching and tilting. The interaction of the vorticity remnants that evolve in a rotating environment with a clockwise turning hodograph in the boundary layer, and with negative vertical shear above is the topic of a future study.

6.8 Storm splitting

The Hogsett and Stewart (2013) conceptual model which seeks to explain the inward contraction of eyewall convection in tropical cyclones is now examined. The model is based on the idea that deep convection growing in the rapidly-rotating environment of a tropical cyclone might have a character similar to "supercell convection", which, in the middle latitudes is a by-product of storm splitting. In the previous chapter a number of experiments were carried out to investigate storm splitting in a warm-cored vortex environment (see below). As it turns out, storm splitting does not occur in any of the experiments performed in this chapter, but there are signs that at low levels the updraught is dividing into two and that perhaps in a more unstable environment, storm splitting could be achieved.

Experiments 3 and 4 of Chapter 5 were designed to investigate storm splitting in a warm-cored vortex, the former in pure vertical shear and the latter in pure horizontal shear. Because of its effect in distorting the initial thermal, vertical wind shear was found to have a detrimental effect on the initiation of convection in those experiments for a given thermodynamic sounding. Indeed, in early experiments with vertical shear and the relatively stable sounding (the same sounding used in this chapter), convection did not occur. For that reason, Experiments 3 and 4 of Chapter 5 used a more unstable sounding to initiate convection, while the present chapter uses a larger thermal perturbation to initiate the convection (see section 6.2.5). The foregoing finding is relevant to the Hogsett and Stewart's conceptual model concerning left-moving split cells in the inner region of tropical cyclones. Since this region is typically one of reduced convective instability and has larger values of CIN, at least in the later stages of storm evolution and warm core development, it cannot be taken for granted that splitting will occur.

A further issue concerning the Hogsett and Stewart's conceptual model is that, as noted above, the vertical shear of the azimuthal-mean tangential wind in a tropical cyclone changes in sign with height near the top of the boundary layer. Even ignoring the additional complexities of the strong radial wind component in the boundary layer of a tropical cyclone, the results of section 5.3 in Chapter 5 and Experiments 2 and 7 from this chapter show that a change in sign of the vertical shear leads to a reversal in sign of the vertical vorticity dipole produced by the updraught at some height. In these experiments, the sign of each vorticity patch is reversed at upper level with a large positive anomaly on the left of

the ordinate and a large negative anomaly on the right, the opposite to what occurs at low levels. This reversal of the sign of vorticity with height in the split cells is different from the classical updraught structure of midlatitude storms. The consequences of the change of sign of this dipole for the vorticity structure of successive updraughts in the case of a split storm has not been discussed previously in the literature. At least Hogsett and Stewart (2013) did acknowledge that the "strongly sheared boundary layer is a critical complexity" that they intend to examine in a future study.

In this chapter, the additional complexities of the strong radial wind component in the boundary layer of a tropical cyclone are included in the wind profile. As well as a changing in sign of the vorticity dipole with height, there is a rotation of the low-level vorticity dipole with height and time. The additional complexities of dipole rotation due to the strong radial wind component and the dipole changing in sign with height would appear to have important implications for Hogsett and Stewart's conjecture.

6.9   Conclusions

A series of idealized numerical model experiments have been presented to investigate aspects of deep convection in tropical depressions and the outer region of tropical cyclones.

A key question in this chapter was: how does a typical vortex boundary-layer-type wind profile structure affect the generation of vertical vorticity and its vertical structure?
Experiments were carried out to quantify the effects of an Ekman-type boundary-layer wind profile on convective structure, and in particular on vertical vorticity production by convection. Consistent with previous chapters, it was found that deep convection that develops in a background of low-level vertical shear and cyclonic vertical vorticity leads to dipole structures of vertical relative vorticity in which the cyclonic gyre is favoured. This dipole structure extends through the lower to middle troposphere and outlives the convection that generates it. The dipole structure changes its orientation with both height and time, as it aligns itself with the local background wind shear at different levels. At early times, the orientation of the dipole corresponds to the orientation of the ambient horizontal vortex lines near the surface as the initial thermal begins to rise. As time proceeds, the vorticity dipole extends vertically as vortex lines are carried upwards by the thermal. At levels where the ambient horizontal vorticity vector rotates with height, so does the axis of the vertical vorticity dipole, but to a lesser extent. The dipole continues to develop with the updraught, even at heights well above those where there is any ambient horizontal vorticity and the vorticity can continue to be amplified by stretching. Convection developing in a vortex boundary layer with negative unidirectional shear above the layer leads to dipole structures of vertical relative vorticity in which the dipole reverses in sign with height.

A second aim of this chapter was to quantify the effects of an increase in

the magnitude of boundary-layer shear on vertical vorticity production.

It was found that in the weakly-sheared boundary layer environment, the initial thermal experiences less deformation and develops more rapidly, with the updraught maximum occurring sooner at a given height than in experiments with larger vertical shear. Likewise, in the strongly-sheared environment, the updraught maximum at a given height occurs later because of the larger deformation of the initial thermal by the stronger shear. Nevertheless, despite having the largest updraught maximum, the experiment with weakest boundary-layer shear has the smallest vertical vorticity maximum on account of the smaller low-level horizontal vorticity available to be tilted into the vertical.

A third aim was to examine the production of vertical vorticity in a more realistic tropical depression environment.

The presence of ambient vertical vorticity was found to lead to additional amplification of low-level vorticity by stretching, especially near the surface. Further, the cyclonic vorticity anomaly at low levels persists longer while the anticyclonic anomaly decays sooner compared to the cell developing in an environment without ambient rotation. The large magnitude of low-level vertical shear in the wind profile that is more realistic for the boundary layer in the outer region of a tropical cyclone is detrimental to the growth of convection, weakening both the updraught and the downdraught. However, the maximum vertical vorticity generated near the surface is relatively large because of the large horizontal vorticity near the surface. In contrast, the maximum vorticity at a height of 1 km is much weaker due to a combination of a weaker updraught and more comparable magnitude of horizontal vorticity to other experiments.

The calculations provide a basis for appraising a recently proposed conceptual model for the inward contraction of eyewall convection in tropical cyclones.

Cell splitting is an essential element of Hogsett and Stewart's conceptual model to explain the inward contraction of eyewall convection in tropical cyclones. Splitting did not occur in any of the experiments performed here, although there was an indication at low-levels that splitting could occur if the thermodynamical environment were more unstable. Since the inner-core tropical cyclone region is typically one of reduced convective instability and has larger values of CIN than in the sounding used here, at least in the later stages of storm evolution and warm core development, it cannot be taken for granted that splitting will occur. The additional complexities of dipole rotation due to the strong radial wind component and the dipole changing in sign with height would appear to have important implications for Hogsett and Stewart's conjecture.

Chapter 7

Conclusions and discussion

7.1   Conclusions

In Chapter 3 the typical evolution of a convective cell in a quiescent environment was described. The updraught that forms the first convective cell was initiated by the buoyancy of the initial bubble. The updraught develops slowly at first, but increases rapidly in vertical extent and strength as additional buoyancy is generated by the latent heat release of condensation. Eventually, a fraction of the condensate that is carried aloft in the updraught grows large enough to fall against the updraught as ice, snow or rain, and subsequently generates a downdraught. As the rain drops fall into the unsaturated air below cloud base they partially evaporate, cooling the surrounding air and strengthening the downdraught. The entire process takes about 20 min, and when the convection decays the air at the surface has low values of θ_e, brought down from the upper levels by the downdraught. Cross sections of the vertical component of relative vorticity indicate a significant amplification of the ambient vorticity extends almost to the top of the cloud, while the vorticity maximum remains located at low levels. The amplified vorticity is a legacy of that generated by stretching during the earlier stages of updraught development, and survives long after the convective cell decays.

Chapter 4 presented a series of numerical experiments designed to isolate the effects of dry air aloft on deep convection, including the efficacy of the convection in amplifying the vertical component of low-level ambient vorticity. Experiments were carried out also to determine the effects of the initial thermal trigger on the ensuing convection. The main focus was on convection that develops within a tropical depression environment using a few thermodynamic soundings acquired during the 2010 PREDICT experiment, or idealized soundings based on these. The initial structure of vertical vorticity was idealized by assuming solid body rotation, but with a value characteristic of disturbances observed during the experiment.

The calculations do not support a common perception that dry air aloft produces stronger convective downdraughts and more intense outflows. Rather, the entrainment of

dry air aloft was found to weaken both convective updraughts and downdraughts. Consistent with recent findings of Wissmeier and Smith (2011), growing convective cells amplify locally the ambient rotation at low levels by more than an order of magnitude and this vorticity, which is produced by the stretching of existing ambient vorticity, persists long after the initial updraught has decayed.

The main aims of Chapter 4 were to answer the questions: if *convective* downdraughts are not strengthened by the presence of dry air, what aspects of the ensuing convection might be detrimental to tropical cyclogenesis? By reducing the updraught strength does the dry air reduce the ability of the convection to amplify vorticity?

It was found that significant amplification of vorticity occurs even for clouds of only moderate vertical extent. The maximum amplification of vorticity was relatively insensitive to the maximum updraught strength, and/or the height at which it occurs. Extending the findings of Wissmeier and Smith (2011), it was shown that the degree of amplification is insensitive to the presence of dry air aloft. Thus these results provide an answer to the question posed earlier: does the reduction of the updraught strength by dry air entrainment have the most detrimental effect on tropical cyclogenesis by reducing the ability of the convection to amplify ambient rotation? The results of this chapter suggest that the answer to this question is no. Nevertheless, the reduction in the depth of the strengthened rotation may be an important effect of dry air on the dynamics of tropical cyclogenesis. For example, it might be speculated that a deeper circulation may be less prone to decay, a possibility that merits further investigation.

Another aim of Chapter 4 was to examine the dependence of the ensuing convection on the temperature excess of the initial bubble.

The results for a limited number of different environmental soundings showed that the maximum amplification of vorticity increases monotonically with the strength of the thermal perturbation used to initiate the convection. However, the amount of increase depends also on the thermodynamic structure of the sounding. Thus, in reality, the amplification of vorticity may depend strongly on the strength of the trigger that initiates the convection, which is generally not known. It depends also on the low-level thermodynamic structure of sounding. The current understanding of the way in which the amplification of vertical vorticity by stretching in convective clouds influences tropical cyclogenesis is not yet complete. However, there is mounting evidence that the interaction between the vorticity remnants of clouds promotes an upscale cascade of cyclonic vorticity that is an important component in the formation of a nascent cyclone-scale vortex. This work is conceived as a useful building block for future studies of this issue.

Chapter 5 described a series of numerical experiments designed to isolate the effects of ambient wind shear, both horizontal and vertical, on the generation of vertical vorticity by deep convection in tropical disturbances.

The first aim of this chapter was to examine the role of a deep layer of negative vertical shear overlying a shallow layer of positive vertical shear on storm morphology. This pattern of shear arises in the tangential wind direction in tropical cyclones, although the complete boundary-layer flow in a tropical cyclone is not unidirectional.

The first set of experiments examined the effect of a uni-directional boundary-layer-type wind profile on vorticity generation. It was found that the implementation of such a profile had a dramatic effect on convection, markedly weakening convective updraughts and downdraughts, thereby reducing the amplification of vertical vorticity and lowering the height to which updraughts penetrate. In the boundary-layer-type wind simulation, the weakening results largely from the deformation of the initial bubble by the low-level vertical shear. This bubble rises first through a layer of positive vertical shear and subsequently through one of negative vertical shear, so that the sign of the background horizontal vorticity it experiences reverses. Thus, two oppositely-signed vorticity dipoles emerge within the updraught, one in the layer of positive vertical wind shear, and the other, in the layer of negative vertical wind shear. This finding would suggest that interpretations of the merger of convectively-induced cyclonic vorticity anomalies in terms of barotropic dynamics may be oversimplistic.

A second aim of Chapter 5 was to extend the study of Wissmeier and Smith (2011) by investigating and quantifying the combined effects of both horizontal and vertical wind shear on deep convection that develops in a thermodynamic environment typical of a tropical depression.

Three experiments were carried out to examine the effects of adding background rotation to the standard boundary-layer-type wind shear profile. It was found that the convection produced had a prominent vorticity dipole associated with the tilting of horizontal vorticity. A second oppositely-signed dipole was produced at later times, generated by the tilting of ambient horizontal vorticity by the convective *downdraught*. As the background rotation rate increases, so does the strength of the positive low-level vertical vorticity anomalies. However, there is little effect on the strength of those in the middle troposphere, indicating that the largest contribution to vertical vorticity production at these levels is by tilting. The inclusion of ice microphysics increases the updraught and downdraught strengths and leads also to a much deeper layer of amplified vorticity than in the warm rain experiment, and one that persists for longer.

A third aim of Chapter 5 was to re-examine the mechanisms involved in storm splitting discussed by Rozoff (2007), again giving particular attention to vertical vorticity generation. Since there is observational evidence for the existence of supercell convection in tropical storms (e.g. Gentry *et al.* 1970, Black 1983), it may be presumed that storm splitting is a relevant process in these systems also.

Two experiments were carried out to examine the effect that storm splitting has on vorticity generation, one in a purely vertically-sheared environment, and one in a purely

horizontally-sheared environment. In the experiment with pure vertical shear, it was found that the maximum vertical velocity and vorticity occur after storm splitting. However, in the experiment with pure horizontal shear, the maximum values of vertical velocity and low-level vertical vorticity occur before splitting. In the latter experiment, a large patch of anticyclonic vertical vorticity is generated despite there being no background source of horizontal vorticity or negative vertical vorticity. This feature may be attributed to the spreading cold pool, which generates horizontal vorticity. This horizontal vorticity is subsequently tilted into the vertical by the split updraughts. Finally two more experiments were carried out to examine vorticity generation in the case of storm splitting in a combined horizontal and low-level vertical shear environment. In the presence of vertical shear only, the vorticity features remain symmetric about the direction of shear throughout the simulation, whereas horizontal shear destroys this symmetry and the evolution of the vorticity field becomes more complex with new flanking cells continuously flaring up.

Chapter 6 presented a series of idealized numerical model experiments to investigate aspects of deep convection in tropical depressions and the outer region of tropical cyclones.

A key question in this chapter was how does a typical vortex boundary-layer-type wind profile structure affect the generation of vertical vorticity and its vertical structure?

Experiments were carried out to quantify the effects of an Ekman-type boundary-layer wind profile on convective structure, and in particular on vertical vorticity production by convection. It was found that deep convection that develops in a background of low-level vertical shear and cyclonic vertical vorticity leads to dipole structures of vertical relative vorticity in which the cyclonic gyre is favoured. This dipole structure extends through the lower to middle troposphere and outlives the convection that generates it. The dipole structure changes its orientation with both height and time, as it aligns itself with the local background wind shear at different levels. At early times, the orientation of the dipole corresponds to the orientation of the ambient horizontal vortex lines near the surface as the initial thermal begins to rise. As time proceeds, the vorticity dipole extends vertically as vortex lines are carried upwards by the thermal. At levels where the ambient horizontal vorticity vector rotates with height, so does the axis of the vertical vorticity dipole, but to a lesser extent. The dipole continues to develop with the updraught, even at heights well above those where there is any ambient horizontal vorticity and the vorticity can continue to be amplified by stretching. Convection developing in a vortex boundary layer with negative unidirectional shear above the layer leads to dipole structures of vertical relative vorticity in which the dipole reverses in sign with height.

A second aim of Chapter 6 was to quantify the effects of an increase in the magnitude of boundary-layer shear on vertical vorticity production.

It was found that in the weakly-sheared boundary layer environment, the initial thermal experiences less deformation and develops more rapidly, with the updraught maximum occurring sooner at a given height than in experiments with larger vertical shear. Likewise, in the strongly-sheared environment, the updraught maximum at a given height occurs later

because of the larger deformation of the initial thermal by the stronger shear. Nevertheless, despite having the largest updraught maximum, the experiment with weakest boundary-layer shear has the smallest vertical vorticity maximum on account of the smaller low-level horizontal vorticity available to be tilted into the vertical.

A third aim of Chapter 6 was to examine the production of vertical vorticity in a more realistic tropical depression environment.
It was found that the presence of ambient vertical vorticity leads to additional amplification of low-level vorticity by stretching, especially near the surface. Further, the cyclonic vorticity anomaly at low levels persists longer while the anticyclonic anomaly decays sooner compared to the cell developing in an environment without ambient rotation. The large magnitude of low-level vertical shear in the wind profile that is more realistic for the boundary layer in the outer region of a tropical cyclone is detrimental to the growth of convection, weakening both the updraught and the downdraught. However, the maximum vertical vorticity generated near the surface is relatively large because of the large horizontal vorticity near the surface. In contrast, the maximum vorticity at a height of 1 km is much weaker due to a combination of a weaker updraught and more comparable magnitude of horizontal vorticity to other experiments.

The calculations provide a basis for appraising a recently proposed conceptual model for the inward contraction of eyewall convection in tropical cyclones.
Cell splitting is an essential element of Hogsett and Stewart's conceptual model to explain the inward contraction of eyewall convection in tropical cyclones. Splitting did not occur in any of the experiments performed here, although there was an indication at low levels that splitting could occur if the thermodynamical environment was more unstable. Since the inner-core tropical cyclone region is typically one of reduced convective instability and has larger values of CIN than in the sounding used here, at least in the later stages of storm evolution and warm core development, it cannot be taken for granted that splitting will occur. The additional complexities of dipole rotation due to the strong radial wind component and the dipole changing in sign with height would appear to have important implications for Hogsett and Stewart's conjecture.

7.2 Discussion and future work

By design the calculations here are all highly idealized. For example, like the classical studies of convective storms discussed in the introduction, there is no representation of boundary-layer friction and no representation of radiative processes. The omission of radiative processes can be justified on the basis that the timescales under consideration are too small for radiative processes to become important (this timescale is on the order of 12 hours according to Rotunno and Emanuel 1987). One may presume the effect of surface friction will be to weaken the magnitudes of vertical vorticity near the surface, but bearing

in mind that the induced tangential wind speeds by a single updraught are typically no more than a few meters per second (Wissmeier and Smith 2011), the frictional effects may not be that important. A new version of the CM1 model including frictional and radiative effects has just become available, providing the possibility to address these issues in due course. At present there are limited observations of vertical vorticity fields in tropical convection, which limits the ability to compare the calculations with observations. Nevertheless, the calculations provide a series of baseline results with which to interpret the effects of more complicated simulations, and will provide a basis for the interpretation of observations as they become available.

While the implementation of an initial thermal perturbation is not particularly realistic, its use may be defended here as a means of isolating and understanding the effects of increasingly more realistic environments on the development of a single updraught. By using an initial thermal bubble it is possible to examine the effects of more complex wind profiles on convective cells, ranging from a quiescent environment to one typical of that in more realistic tropical depression environments. While the updraught strengths may appear on the high side compared with those commonly reported in deep tropical convection, it is worth noting that the maximum observed vertical velocities determined by aircraft penetrations may be expected to have a bias because, for safety reasons, pilots will not deliberately fly into the most intense updraughts.

The present study was motivated by the desire to understand the merger of convectively-induced vorticity anomalies during vortex evolution, a process that is currently not well known. The interaction of the vorticity remnants that evolve in a rotating environment is the topic of a future study. High temporal and spatial resolution simulations using the MM5 model[1] are planned in order to analyse the interaction of the vorticity remnants in a rotating vortex. The vertical vorticity structures that developed in the more realistic tropical depression environment of Chapter 6, will presumably develop also in the MM5 simulations, albeit with possibly weaker rotation near the surface due to friction. An interesting possibility is that the convective cells that develop in the MM5 simulations will have cyclonic vorticity dominating at low levels, like in Chapter 6, and the inward radial flow associated with the secondary circulation of the vortex may lead to a merger of convectively-induced vorticity anomalies as the vortex evolves. Interesting questions arise then: what role does the upper-level vertical vorticity dipole play, and to what extent are barotropic arguments applicable as proposed in Nguyen *et al.* (2008)?

---

[1]Or the latest version of CM1 which can be run with an initial vortex, radiative processes and boundary layer friction.

Bibliography

Arakawa A, Lamb VR, 1977: Computational design and the basic dynamical processes of the UCLA general circulation Model. *Methods in Computational Physics* **17**. p173.

Black PG. 1983: Tropical storm structure as revealed by stereoscopic photographs from skylab. *Adv. Space Res.*, **2**, 115-124.

Bolton D. 1980: The computation of equivalent potential temperature. *Mon. Wea. Rev.*, **108**, 1046-1053.

Bluestein HB, McCaul EW, Byrd GP, Woodall GR, 1988: Mobile sounding observations of a tornadic storm near the dryline: The Canadian, Texas storm of 7 May 1986. *Mon. Wea. Rev.*, **116**, 1790-1804.

Braun SA Montgomery MT Mallen KJ Reasor PD. 2010 Simulation and interpretation of the genesis of Tropical Storm Gert (2005) as part of the NASA Tropical Cloud Systems and Processes Experiment. *J. Atmos. Sci.*, **67**, 999-1025.

Braun SA Sippel JA Nolan DS. 2012: The impact of midlevel dry air on hurricane intensity in idealized simulations with no mean flow. *J. Atmos. Sci.*, **69**, 236-257.

Brown RG Zhang C. 1997: Variability of midtropospheric moisture and its effect on cloud-top height distribution during TOGA COARE. *J. Atmos. Sci.*, **54**, 2760-2774.

Browning KA., 1964: Airflow and precipitation trajectories within severe local storms which travel to the right of the winds. *J. Atmos. Sci.*, **21**, 634-639.

Bryan GH. 2002: An investigation of the convective region of numerically simulated squall lines. *Ph.D. thesis, The Pennsylvania State University*, 181 pp.

Bryan GH Fritsch JM. 2002: A benchmark simulation for moist nonhydrostatic numerical models. *Mon. Wea. Rev.*, **130**, 2917-2928.

Bryan GH, Rotunno R, 2009: The maximum intensity of Tropical cyclones in axisym-

metric numerical model simulations. *Mon. Wea. Rev.*, **137**, 1770-1789.

Bryers HR, Braham RR, 1949: The thunderstorm. *US Government Printing Office*, Washington 25, CD, USA

Browning KA, 1977: The structure and mechanism of hailstorms. *Meteor. Monogr.*, **38**, 1-39

Cotton WR, Bryan GH, Van Den Heever SC, 2011: *Storm and cloud dynamics, second edition*. Academic Press.

Davies-Jones RP, 1974: Discussion of measurements inside high-speed thunderstorm updrafts. *J. Atmos. Sci.*, **13**, 710-717.

Deng Q, Smith L, Majda A 2012: Tropical cyclogenesis and vertical shear in a moist Boussinesq model. *Journal of Fluid Mechanics*, **706**, pp 384-412

Didlake AC, Houze RA, 2011: Kinematics of the secondary eyewall observed in Hurricane Rita (2005). *J. Atmos. Sci.*, **68**, 1620-1636.

Dunion, J.P, and C.S. Veldon, 2004: The impact of the Saharan air level on Atlantic Tropical cyclone activity. *Bull. Amer. Meteor. Soc.,* **85**, 353-365.

Dunion JP, Marron CS, 2008: A Reexamination of the Jordan mean Tropical sounding based on awareness of the Saharan air layer: Results from 2002. *J. Atmos. Sci.*, **21**, 5242-5253.

Dunkerton, T. J., Montgomery, M.T., and Wang, Z., 2009: Tropical cyclogenesis in a tropical wave critical layer: easterly waves. *Atmos. Chem. & Phys.,* **9**, 5587-5646.

Emanuel KA. 1989 The finite amplitude nature of tropical cyclogenesis. *J. Atmos. Sci.*, **46**, 3431-3456.

Emanuel KA. 1994: Atmospheric convection. *Oxford University Press*, 580 pp.

Fang J Zhang F. 2010: Initial development and genesis of Hurricane Dolly (2008). *J. Atmos. Sci.*, **67**, 655-672.

Ferrier BS Houze RA. 1989: One dimensional time-dependent modelling of GATE cumulonimbus convection. *J. Atmos. Sci.*, **46**, 330-352.

Fierro AO Zipser EJ Lemone MA Straka JM Simpson J. 2012: Tropical oceanic hot towers: need they be dilute to transport energy from the boundary layer to the upper tro-

posphere effectively? An answer based on trajectory analysis of a simulation of a TOGA COARE convective system. *J. Atmos. Sci.*, **69**, in press.

Foster IJ, Lyons TJ, 1984: Tropical cyclogenesis: A comparative study of two depressions in the northwest of Australia. Quart. J. Roy. Meteor. Soc., 110, 105-119.

Frank WM. 1987: Tropical cyclone formation. In: *A global view of tropical cyclones.* Ed. R. L. Elsberry, Office of Naval Research, 53-90.

Gentry RC, Fujita TT, Sheets RC. 1970: Aircraft, spacecraft, satellite and radar observations of Hurricane Gladys. *J. Appl. Meteor.*, **9**, 837-850.

Gilmore MS Straka JM Rasmussen EN. 2004. Precipitation and evolution sensitivity in simulated deep convective storms: comparisons between liquid-only and simple ice and liquid phase microphysics. *Mon. Wea. Rev.*, **132**, 1897-1916.

Haynes P McIntyre ME. 1987: On the evolution of vorticity and potential vorticity in the presence of diabatic heating and frictional or other forces. *J. Atmos. Sci.*, **44**, 828-841.

Hendricks EA Montgomery MT Davis CA. 2004: On the role of "vortical" hot towers in formation of tropical cyclone Diana (1984). *J. Atmos. Sci.*, **61**, 1209-1232.

Heymsfield AJ, Hjelmfelt M, 1981: Dynamical and microphysical observations in two Oklahoma squall lines: Part II - Insitu measurements. *20th Conference on Radar Meteorology*, Boston, MA.

Hogsett W, Stewart SR, 2013: Dynamics of Tropical cyclone intensification: Deep convective cyclonic "left-movers". *J. Atmos. Sci.*, Early view

Holloway CE Neelin JD. 2009: Moisture vertical structure, column water vapor, and tropical deep convection. *J. Atmos. Sci.*, **66**, 1665-1683.

Holton JR. 2004 *An introduction to dynamic meteorology* Academic Press, London, pp535.

Houze RA, Lee W-C, Bell MM, 2009. Convective contribution to the genesis of hurricane Ophelia (2005). *Mon. Wea. Rev.*, **137**: 2778-2800.

James IN, 1994: Introduction to circulating atmospheres. *Cambridge University Press*, London.

James RP, Markowski PM, 2009: A numerical investigation of the effects of dry air aloft on deep convection. *Mon. Wea. Rev.*, **138**, 140-161.

Karyampudi VM, Pierce HF, 2002: Synoptic-scale influence of the Saharan air layer on tropical cyclogenesis over the eastern Atlantic. *Mon. Wea. Rev.*, **130**, 3100-3128.

Klemp JB, Wilhelmson RB, 1978: The simulation of three-dimensional convective storm dynamics. *J. Atmos. Sci.*, **35**, 1070-1096.

Klemp JB, 1987: Dynamics of tornadic thunderstorms. *Annual Rev. Fluid Mech.*, **19**, 396-402.

Kuchera EL, Parker MD, 2006: Severe convective wind environments. *Wea. Forecasting*, **21**, 595-612.

LeMone MA, Zipser EJ, 1980: Cumulonimbus vertical velocity events in GATE. Part I: Diameter, intensity and mass flux. *J. Atmos. Sci.*, **37**, 2444-2457

Lin YL, Farley RD, Orville HD, 1983: Bulk parameterization of the snow field in a cloud model. J. Climate Appl. Meteor., 22, 1065-1092.

McBride JL, 1995: Tropical cyclone formation. In *Global Perspectives on Tropical Cyclones. pp21-62. WMO/TD-No 693 (Ed. R. L. Elsberry), World Meteorological Organization, Geneva*, 289pp.

Minoru C, Sugiyama M, 2010: A cumulus parameterization with state-dependent entrainment rate. Part I: Description and sensitivity to temperature and humidity profiles. *J. Atmos. Sci.*, **67**, 2171-2193.

Montgomery MT Nicholls ME Cram TA Saunders AB. 2006: A vortical hot tower route to tropical cyclogenesis. *J. Atmos. Sci.*, **63**, 355-386.

Montgomery MT, Smith RK. 2011. Tropical cyclone formation: Theory and idealized modelling. In Proceedings of Seventh WMO International Workshop on Tropical Cyclones (IWTC-VII), La Réunion, Nov. 2010. (WWRP 2011-1) World Meteorological Organization: Geneva, Switzerland.

Montgomery MT Nguyen SV Smith RK. 2009: Do tropical cyclones intensify by WISHE? *Q. J. R. Meteorol. Soc.*, **135**, 1697-1714.

Montgomery MT, Davis C, Dunkerton T, Wang Z, Velden C, Torn R, Majumdar S, Zhang F, Smith RK, Bosart L, Bell MM, Haase JS, Heymsfield A, Jensen J, Campos T, Boothe MA, 2012: The pre-depression investigation of cloud systems in the Tropics (PRE-DICT) experiment: Scientific basis, new analysis tools, and some first results. *Bull. Amer. Meteor. Soc.,* **93**: 153-172.

Newton, CW, 1950: Structure and mechanism of the prefrontal squall line. *J. Meteor.*, 7, 210-222.

Nguyen SV Smith RK Montgomery MT. 2008: Tropical-cyclone intensification and predictability in three dimensions. *Q. J. R. Meteorol. Soc.*, **134**, 563-582.

Ooyama KV. 1969 Numerical simulation of the life cycle of tropical cyclones. *J. Atmos. Sci.*, **26**, 3-40.

Raymond DJ., Gjorgjievska S, Sessions S. Fuchs Ž, 2013: Tropical cyclogenesis and mid-Level vorticity. *Aust. Met. Ocean. Soc. Journl.*, (submitted).

Redelsperger JL Parsons DB Guichard F. 2002: Recovery processes and factors limiting cloud-top height following the arrival of a dry intrusion observed during TOGA COARE. *J. Atmos. Sci.*, **59**, 2438-2457.

Riehl H, Malkus J, 1958. On the heat balance of the equatorial trough zone. Geophysica, v6, Nos 3-4 503-538

Rotunno R, 1981: On the Evolution of Thunderstorm Rotation. *Mon. Wea. Rev.*, **109**, 577-586.

Rotunno R, Klemp JB, 1982: The influence of the shear-induced pressure gradient on thunderstorm motion. *Mon. Wea. Rev.*, **110**, 136-151.

Rotunno R, Klemp JB, 1985: On the rotation and propagation of simulated supercell thunderstorms. *J. Atmos. Sci.*, **42**, 271-292.

Rotunno R, Emanuel KA, 1987: An air-sea interaction theory for tropical cyclones. Part II: Evolutionary study using a nonhydrostatic axisymmetric numerical model. *J. Atmos. Sci.*, **44**, 542-561.

Rozoff CM 2007: Aspects of moat formation in tropical cyclone eyewall replacement cycles. *Ph.D. thesis, Colorado State University*, 165 pp.

Saunders and Montgomery MT. 2004: A closer look at vortical hot towers within a tropical cyclogenesis environment. Colorado State University, Atmospheric Science Bluebook No. 752.

Schlesinger, RE, 1978: A three-dimensional numerical model of an isolated thunderstorm: Part I. Comparative experiments for variable ambient wind shear. *J. Atmos. Sci.*,

35, 690-713.

Shin S Smith RK. 2008 Tropical-cyclone intensification and predictability in a minimal three-dimensional model. **134**, 1661-1671.

Smith RK, Montgomery MT, Zhu H, 2005: Buoyancy in tropical cyclone and other rapidly rotating atmospheric vortices. Dyn. Ocean Atmos. Dyn. Atmos. Oceans, **40**, 189-208.

Smith RK Montgomery MT. 2012: Observations of the convective environment in developing and non-developing tropical disturbances. *Q. J. R. Meteorol. Soc.*, **138**, (in press).

Smith RK, Montgomery MT, 2013: On the existence of the logarithmic surface layer in the inner core of hurricanes *Q. J. R. Meteorol. Soc.*, (in early view).

Sobel AH. Yuter SE Bretherton CS Kiladis GN. 2004: Large-scale meteorology and deep convection during TRMM KWAJEX. *Mon. Wea. Rev.*, **132**, 422-444.

Stern, DP, Nolan DS, 2011: On the vertical decay rate of the maximum tangential winds in tropical cyclones. *J. Atmos. Sci.*, **68**, 2073-2094.

Tompkins AM. 2001: Organization of tropical convection in low vertical wind shears: The role of water vapor. *J. Atmos. Sci.*, **58**, 529-545.

Tory K Frank WM. 2010: Tropical cyclone formation. Chapter 2 of Global perspectives on tropical cyclones: From science to mitigation. (Ed. Kepert JD. Chan JCL.) World Scientific Series on Asia-Pacific Weather and Climate, Vol. 4, 448pp.

Trier SB Skamarock WC LeMone MA Parsond DB Jorgensen DP. 1996: Structure and evolution of the 22 February 1993 TOGA COARE squall line: numerical simulations. *J. Atmos. Sci.*, **53**, 2861-2886.

Vogl S, Smith RK, 2009, Limitations of a linear model for the hurricane boundary layer, *Q. J. R. Meteorol. Soc.*, **135**, 839-850.

Weisman ML Klemp JB. 1982: The dependence of numerically simulated convective storms on vertical wind shear and buoyancy. *Mon. Wea. Rev.*, **110**, 504-520.

Weisman ML, Klemp JB, 1984: The structure and classification of numerically simulated convective storms in directionally varying wind shears. *Mon. Wea. Rev.*, **112**, 2479-2498.

Wilhelmson RB, Klemp JB, 1978: A numerical study of storm splitting that leads to long-lived storms. 1974-1986.

Wilhelmson RB, Klemp JB, 1981: A three-dimensional numerical simulation of splitting severe storms on 3 April 1964. *J. Atmos. Sci.*, **38**, 1581-1600.

Wissmeier U. 2009: The physics of tropical convection. *Ph.D. Dissertation, Ludwig-Maximilians University of Munich*, 124 pp.

Wissmeier U Smith RK. 2011: Tropical-cyclone convection: the effects of ambient vertical vorticity. *Q. J. R. Meteorol. Soc.*, **137**, 845-857.

Acknowledgements

Curriculum Vitae

Gerard Kilroy

Faculty of Physics, Ludwig-Maximilians University
Theresienstr. 37, 80333 Munich

Nationality	Irish
Date of Birth	06/06/1986
Contact	gerard.kilroy@physik.uni-muenchen.de

Education

2011 - Now	**Ph.D. student at LMU (University of Munich),** Faculty of Physics, Prof. Dr. Roger K. Smith. Thesis title: Numerical studies of tropical convection
2009 - 2011	**M.Sc. Meteorology, UCD (University College Dublin, Ireland),** Faculty of Physics, Prof. Dr. Peter Lynch. Thesis title: Performance of the WRF Model in Simulating Historical Irish Storms Grade: Second Class Honours, Grade 1
2005 - 2009	**B.Sc. Mathematical Science, UCD (University College Dublin, Ireland),** Grade: Second Class Honours, Grade 1
1999 - 2005	**Leaving Certificate, Rice College, Westport, Ireland** Grade: 485 Points

Work History

| 2007 - 2010 | UCD Sports Centre assistant, Dublin. |
| 2008 - 2010 | Sports coach/First aid officer at UCD Sport Summer Camps, Dublin. |

Publications

- Kilroy G and Smith RK, 2012: A numerical study of rotating convection during tropical cyclogenesis. *Q. J. R. Meteorol. Soc.*, **139**, 1255-1269.

- Kilroy G, Smith RK, and Wissmeier U, 2013: Tropical convection: the effects of ambient vertical and horizontal vorticity. *Q. J. R. Meteorol. Soc.*, (in early view).

- Kilroy G and Smith RK, 2013: Tropical-cyclone convection: the effects of a vortex boundary layer wind profile on deep convection *Q. J. R. Meteorol. Soc.*, (submitted).

Conferences and Summer Schools

- 30th Conference on Hurricanes and Tropical Meteorology (2012); Oral presentation: A numerical study of rotating convection during tropical cyclogenesis.

- Invited as a guest speaker to give an oral presentation at the School of Mathematical Sciences, UCD, Dublin (2012).

- Attended the 4th ISAC Summer School, 2012 in Lecce, Italy. The topic was Severe Convective Weather: Theory and Applications.

- Awarded the Royal Meteorological Society (RMS) Rupert Ford Travel Award (2013) to visit the Tropical Regional Forecasting Centre, Darwin, Australia.

Membership

- Member of the American Meteorological Society (AMS).

- Member of the Royal Meteorological Society (RMS).